An Investigation into the Shape and Insertion Mechanism of a Bio-Inspired Trephine Needle for Bone Marrow Biopsy

A Thesis Submitted

in Partial Fulfillment of the Requirements

for the Degree of

Doctor of Philosophy

by

Rahul Nadda

(2020BMZ0011)

DEPARTMENT OF BIOMEDICAL ENGINEERING

INDIAN INSTITUTE OF TECHNOLOGY ROPAR

April 2024

Rahul Nadda:

An Investigation into the Shape and Insertion Mechanism of a Bio-Inspired Trephine Needle for Bone Marrow Biopsy

DECLARATION OF ORIGINALITY

I, **Rahul Nadda,** hereby declare that the work which is being presented in the thesis entitled **"** *An Investigation into the Shape and Insertion Mechanism of a Bio-Inspired Trephine Needle for Bone Marrow Biopsy***"** has been solely authored by me. It presents the result of my own independent investigation/research conducted during Jan 2021 - Oct 2023 under the supervision of **Dr. Ramjee Repaka, Associate Professor** and **Dr. Ashish Kumar Sahani, Assistant Professor**. To the best of my knowledge, it is an original work, both in terms of research content and narrative, and has not been submitted or accepted elsewhere, in part or in full, for the award of any degree, diploma, fellowship, associateship, or similar title of any university or institution. Further, due credit has been attributed to the relevant state-of-the-art and collaborations (if any) with appropriate citations and acknowledgments, in line with established ethical norms and practices. I also declare that any idea/data/fact/source stated in my thesis has not been fabricated/ falsified/ misrepresented. All the principles of academic honesty and integrity have been followed. I fully understand that if the thesis is found to be unoriginal, fabricated, or plagiarized, the Institute reserves the right to withdraw the thesis from its archive and revoke the associated Degree conferred. Additionally, the Institute also reserves the right to appraise all concerned sections of society of the matter for their information and necessary action (if any). If accepted, I hereby consent for my thesis to be available online in the Institute's Open Access repository, inter-library loan, and the title & abstract to be made available to outside organizations.

Signature

Name: **Rahul Nadda**

Entry Number: **2020BMZ0011**

Program: **PhD**

Department: **Biomedical Engineering**

Indian Institute of Technology Ropar

Rupnagar, Punjab 140001

Date: 9/April/2024

CERTIFICATE

This is to certify that the thesis, entitled "*An Investigation into the Shape and Insertion Mechanism of a Bio-Inspired Trephine Needle for Bone Marrow Biopsy*", authored by **Mr. Rahul Nadda (2020BMZ0011)** for the award of **Doctor of Philosophy** submitted to the Department of Biomedical Engineering, Indian Institute of Technology Ropar is an authentic record of bonafide research work carried out under our guidance and supervision. To the best of our knowledge and belief, the work presented in this thesis is original and has not been submitted, either in part or full, for the award of any other degree, diploma, fellowship, associateship or similar title of any university or institution.

In our opinion, the thesis has reached the standard fulfilling the requirements of the regulations relating to the Degree.

Signature of the Supervisor
(Dr. Ramjee Repaka)
Associate Professor,
Department of Mechanical Engineering,
Indian Institute of Technology Ropar
Date: 9/April/2024

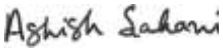

Signature of the Co-Supervisor
(Dr. Ashish Kumar Sahani)
Assistant Professor,
Department of Biomedical Engineering
Indian Institute of Technology Ropar
Date: 9/April/2024

`

ACKNOWLEDGMENTS

- As another phase of life is ready to dawn with the submission of my PhD thesis, there have been numerous helping hands and genuine advice behind the successful completion of my work. First and foremost, I express my sincere gratitude and respect to my thesis supervisor(s) **Dr. Ramjee Repaka,** Associate Professor, Department of Mechanical Engineering and **Dr. Ashish Kumar Sahani**, Assistant Professor, Department of Biomedical Engineering, IIT Ropar, for their valuable guidance, constant encouragement throughout this study and untiring help, without which this research would not have attained its shape. Words would not be enough to describe the ocean of knowledge they have, and I feel divinely blessed to have worked under their guidance and command. I would also like to thank them for the brotherly support and the parent-like emotional care that not only helped me evolve myself as a researcher but also develop me as a better individual.
- I would also like to extend my heartfelt appreciation to **Prof. Reena Das** (Head of the Department), **Dr. Nabhajit Mallik**, General Physician and all **Senior and Junior residents** of the Department of Hematology, Postgraduate Institute of Medical Education & Research, Chandigarh, India, for providing the necessary support, and Indian Institute of Technology Ropar for providing necessary facilities to carry out this research.
- It would be unfair if I proceed without thanking my DC committee members, **Dr. Srivatsava Naidu**, Assistant Professor, Department of Biomedical Engineering, **Dr. Subrahmanyam Murala**, Associate Professor, Department of Electrical Engineering, **Dr. RaviKant**, Assistant Professor, Department of Mechanical Engineering, and **Dr. Rajesh Kumar**, Assistant Professor, Department of Biomedical Engineering, IIT Ropar for his concern for me and efficient and timely advice on research activities that helped me to complete my research with ease and well in time.
- I hereby mention special heartfelt thanks to **Dr. Prabir Sarkar**, Associate Professor, Department of Mechanical Engineering, **Dr. Anshu Dhar Jayal**, Assistant Professor, Department of Mechanical Engineering, for providing me the necessary additional computational facility in their lab.
- I would like to extend my heartfelt appreciation to the dedicated staff members of the Mechanical Engineering Department at IIT Ropar, especially **Mr. Sukhwinder Singh**, for their valuable support in helping me complete my research work. Their assistance in providing an additional workstation facility in the CAD lab was instrumental in the successful completion of my project. I am truly grateful for their kindness and encouragement throughout this journey.
- I would also like to extend my heartfelt appreciation to the dedicated staff members **Mr. Jitender Sayal** and **Mr. Dharminder Singh** of the Biomedical Engineering Department at IIT Ropar for helping me out in my office related work.

- I am highly obliged and thankful to my seniors, colleagues, well-wishers and friends- **Dr. Manoj Kumar, Dr. Ajinkya Sirsat, Nishant Shakya, V. Satish, Dasari Yogeshwar, Dhiraj Kumar, Jitender Singh, Rajendra Choudhary, Abhishek Gangawar** whom I might not have made a special mention of here, but they always stay with a special mention in my life.
- Yet importantly, I extend my salutations to my beloved parents: **Sh. Manohar Lal Nadda** and **Smt. Pushap Lata** for their everlasting encouragement and support. I would like to dedicate this thesis to my highly respected parents whose unwavering support was the backbone for completing this thesis work.
- Last but not least, I wish to record my gratitude, with utmost reverence and gracious faithfulness to the **Almighty** for His indomitable lead and guidance throughout my life.

Thank You all!

April of 2024 **Rahul Nadda**

LAY SUMMARY

A bone marrow biopsy (BMB) is a clinical procedure employed to extract a small specimen of bone marrow for diagnosis. The purpose of a bone marrow biopsy is to aid doctors in assessing the condition of the bone marrow, which plays a vital role in the production of blood cells within the human body. A bone marrow biopsy can help diagnose blood problems, malignancies, infections, and autoimmune illnesses. While it can result in discomfort, it is usually seen as an effective procedure. The initial stage of the study involved conducting a prospective survey on bone and bone marrow trephine biopsies obtained from Indian patients. The primary objective has been to gain a comprehensive understanding of the process and explore its potential application in patient care, raising awareness about the effectiveness of trephine biopsy. The secondary objective has been to assess the procedural difficulty, patient discomfort, needle bending frequency, repetition rate, and sample collection precision in trephine bone marrow biopsy. Following the survey and documentation of various issues encountered during the biopsy procedure, a reusable device for bone marrow biopsy has been developed. The reusable biopsy device offers enhanced comfort to clinicians during bone marrow sample collection and benefits patients due to its user-friendly, sustainable, and cost-effective design. Due to remarkable advancements in medical sciences, numerous treatment options are now accessible in clinical settings. Doctors frequently recommend an appropriate biopsy diagnosis based on the affected organ and the stage of the disease. The current study aims to improve BMB procedures by creating a needle inspired by the stinger of a honeybee and mosquito proboscis, leading to enhanced accuracy, reduced patient discomfort, prevention of deflection and clogging, and increased efficiency.

The focus of this thesis has been to explore the potential advantages of utilizing bio-inspired needles modeled based on the stinger and proboscis of honeybees and mosquitoes. A 3D finite element multilayer iliac crest model has been developed to investigate the barbed needle tip (bevel) effect, insertion velocity, and barb shapes. Further, the needle deflection, shear stress, and von Misses distribution around the barbed needle have also been studied. It has been shown in this thesis that an improvised bio-inspired BMB device possesses the potential to reduce insertion/extraction forces and avoid patient discomfort, deflection, and clogging without compromising the diagnosis procedure. This work aims to create a computationally feasible simulation model for a bio-inspired needle design based on the stinger of a honeybee and the proboscis of a mosquito. Such a model is expected to demonstrate the relationship between the axial forces measured on the needle and the penetration depth during insertion/extraction into/from the soft tissue and the bone. The needle rotation decreases the cutting force on the tissue, improving clinical outcomes and reducing discomfort. In this connection, the present investigation aims to analyze the effects of essential factors, viz., needle rotation, α_1, α_2, h_b, L_{bs} and insertion velocity on insertion and extraction forces produced during the BMB procedure. The present study evaluated the cutting forces during needle insertion and extraction using unidirectional (360° rotation) and bidirectional (180°clock and anti-clock rotation) bioinspired BMB needles. Further, the current study considers Taguchi's L32 orthogonal array, which requires 32 tests instead of 2048 for the

full factorial design approach. Each computational procedure has been carried out step by step using ABAQUS FEM software to evaluate the tissue deformation, needle bending, insertion, and extraction forces up to a depth of 53 mm.

Further, other important goal of this study is to develop an Artificial Intelligence (AI) tool that can support clinicians in their decision-making process by assisting in selecting an appropriate biopsy needle for BMB procedures, considering various design parameters of the needle. The proposed tool is based on an Artificial Neural Network (ANN) model, which takes the biopsy needle design parameters (viz. needle rotation, α_1, α_2, h_b, L_{bs} and insertion velocity) as inputs and provides the corresponding outputs regarding insertion/extraction force and needle deflection. A user-friendly Graphical User Interface (GUI) has been developed for the AI tool to ensure efficient utilization by clinicians. Initial results indicate that the bio-inspired honeybee stinger and mosquito proboscis needles outperformed the conventional needle across multiple aspects. These needles' reduced diameter and enhanced flexibility facilitated smoother penetration and minimized tissue damage during the procedure. Moreover, the bio-inspired needles exhibited enhanced precision in extracting bone marrow samples, leading to higher-quality specimens for diagnostic analysis and benefiting clinicians in their diagnostic procedures. The encouraging outcomes suggest that bio-inspired honeybee and mosquito proboscis needles potentially enhance the bone marrow biopsy experience for patients while improving healthcare providers' overall procedure. Additional studies and clinical trials are required to validate these findings and ensure the safety and effectiveness of these innovative needle designs.

ABSTRACT

Bone marrow biopsy (BMB) needles are commonly utilized for extracting tissue samples to identify lesions or abnormalities detected during medical examinations or radiological scans. During this technique, the inadequate support from the surrounding tissue results in tissue damage and displacement due to needle insertion forces. An additional challenge during the procedure is the needle deflection during insertion, leading to more pronounced tissue deformation. Tissue distortion and needle deflection frequently cause needle tip misalignment, reducing the intended targeting precision. There is a lack of studies addressing key aspects such as anxiety, pain, needle types, biopsy duration, needle deflection, recurrence rates, bone texture, tissue deformation, crack propagation, and more in the context of BMB. Drawing inspiration from the complex structures of the honeybee stinger and mosquito proboscis, our biomimetic design integrates peripheral barbs on the needle and vibration to improve tissue penetration and sample retrieval. To begin with, we conducted a prospective survey involving bone and bone marrow trephine biopsies obtained from Indian patients. The performance of the needle during BMB procedures has been assessed using the finite element method-based simulations, which analyzed factors such as insertion/extraction forces, needle deflection, tissue damage, and bone damage. The study has investigated the impact of unidirectional and bidirectional rotation on needle insertion/extraction into skin-bone tissue (iliac crest model). Through biomechanical modeling of the needle, our objective has been to optimize its design and comprehend the effects of various rotation modes and associated parameters on the efficiency and accuracy of needle insertion/extraction. Additionally, the thesis explored the application of unidirectional (360° rotation) and bidirectional (180° C.W. and C.C.W. rotation) rotation during needle insertion. Alongside the biomechanical analysis, an artificial neural network (ANN)-based AI tool has been developed to aid clinicians in selecting the optimal biopsy needle for BMB procedures. By incorporating insights from finite element simulations, the AI tool integrated the knowledge to offer recommendations based on criteria such as insertion/extraction forces, deflection, torque, and tissue damage. The primary objective of this tool is to assist clinicians in their decision-making process, ultimately improving the overall success and safety of BMB procedures. The results derived from the FE simulations offer valuable insights into the performance of the bio-inspired BMB needle. This research contributes to optimizing the needle design for enhanced clinical outcomes by analyzing insertion/extraction forces, deflection characteristics, tissue damage, and bone damage. In addition, the AI tool developed in this thesis provides a novel approach to assist clinicians in choosing the most suitable needle for BMB procedures. In summary, this study synergistically integrates finite element simulations and AI-assisted decision-making tool to advance the field of bio-inspired bone marrow biopsy needles. The potential implications of these findings include more efficient and minimally invasive BMB procedures, leading to improved patient comfort and diagnostic accuracy.

LIST OF PUBLICATIONS

Journal papers

1. **Nadda, R.**, Sahani, A.K., Repaka, R. A systematic review of real-time fine-needle aspiration biopsy methods for soft tissues. IETE Tech Rev. 2022;39(5):1011–26.
2. **Nadda, R.**, Repaka, R., Sahani, A.K. Finite element simulation of multilayer model to simulate fine needle insertion mechanism into iliac crest for bone marrow biopsy. Comput Methods Biomech Biomed Engin. 2022;26(8):877–92.
3. **Nadda, R.**, Repaka, R., Sahani, A.K. Numerical modeling of conical-shaped bone marrow biopsy needle into multilayer iliac crest model. J Eng Sci Med Diagn Ther. 2023;6(1):011001.
4. **Nadda, R.**, Repaka, R., Sahani, A.K. Honeybee stinger-based biopsy needle and influence of the barbs on needle forces during insertion/extraction into the iliac crest: a multilayer finite element approach. Comput Bio Med. 2023; 162:107125.
5. **Nadda, R**., Repaka, R., Mallik, N., Sahani, A.K. A prospective survey on trephine biopsy of bone and bone marrow: an experience with 274 Indian patients' biopsies. Eur J Med Res 28, 193 (2023). https://doi.org/10.1186/s40001-023-01167-7
6. **Nadda, R.,** Repaka, R., Sahani, A.K. Development of a multilayer iliac crest numerical model for simulating honeybee stinger-inspired hollow needle insertion. J Eng Sci Med Diagn Ther. 2024; 7(1): 011201
7. **Nadda, R.,** Repaka, R., In-silico analysis of optimal configurations for rotational bioinspired bone marrow biopsy needle designs: An ANN Approach, Ann Biomed Eng. 2023, 1-19.

Conference papers

1. **Nadda, R.,** Repaka, R., Sahani, A.K. DEVELOPMENT OF A MULTILAYER ILIAC CREST NUMERICAL MODEL FOR SIMULATING HONEYBEE STINGER-INSPIRED HOLLOW NEEDLE INSERTION, ASME, IMECE (2023).

Patents

1. **Nadda, R.,** Repaka, R., Yogeshwar, D., Sahani, A.K. A BONE MARROW BIOPSY DEVICE, Application number (202211061266) **(Published)**

TABLE OF CONTENTS

LIST OF FIGURES

LIST OF TABLES

NOTATIONS AND ABBREVIATIONS

ANN	Artificial neural network
ALE	Arbitrary Lagrangian Eulerian
AI	Artificial intelligence
BMA	Bone marrow aspiration
BMB	Bone marrow biopsy
CAD	Computer aided design
FEM	Finite element method
GUI	Graphical User Interface
α_1	Barbed front angle
α_2	Barbed back angle
h_b	Height of barb
L_{bs}	Length of the portion containing barbs
n	Desired sample size from the unlimited population
E	Margin of error
N	Size of the population under consideration
Z	z score
$\hat{p}$	Estimated population proportion
θ	Included angle of needle tip
λ	Inclination angle
ξ	Bevel angle
U	Strain energy density
$\bar{I}_1, \bar{I}_2,$ and $\bar{I}_3$	Cauchy-Green deformation tensors
J_{el}	Elastic volume ratio
C_{i0}	Material constants
D_i	Material constants
P	Point of contact
$\frac{\cdot}{\varepsilon}_o^{pl}$	Reference plastic strain rate
$\Delta\bar{\varepsilon}^{pl}$	Growth in the equivalent plastic strain
T_{melt}	Melting temperature
T_{room}	Room temperature
p	Pressure Stress
q	Von Mises equivalent stress
r_i	Inner radius

r_o	Outer radius
t_b	Barb tip thickness
$\bar{\varepsilon}^{pl}$	Equivalent plastic strain
$\dot{\bar{\varepsilon}}^{pl}$	Equivalent plastic strain rate

Chapter 1
Introduction

This chapter provides a concise yet comprehensive introduction that outlines the importance and background of the questions being addressed. Furthermore, this chapter discusses the objectives to address these problems and comprehensively overview its contents.

1.1 Background and Motivation

Diagnosis of hematopoietic diseases can be challenging since peripheral blood tests and traditional laboratory tests may not always give comprehensive or adequate information for an appropriate diagnosis. In certain cases, a direct microscopic evaluation of the bone marrow is necessary to confirm a potential medical disorder or to monitor the progress of medicinal treatment. This invasive treatment includes extracting a sample of bone marrow for detailed examination under a microscope, which allows an in-depth study of the hematologic disease. Bone marrow examination plays a crucial role in diagnosing hematological disorders and managing patients with such conditions. The BMB and BMA are the exclusive methods for obtaining crucial material for immunophenotyping, molecular, histological and cytological studies in evaluating and treating hematological disorders [1]. The bone marrow examination involves the aspiration and spreading of bone marrow particles on slides, as well as the collection of a core sample of bone and marrow (trephine biopsy). BMA procedures are useful for assessing the morphology of cells and performing alternative cell counts; however, BMB is recommended to evaluate megakaryocyte count and detect focal lesions, viz. metastatic carcinoma, lymphoma and granuloma cancer [2, 3]. Due to their complimentary insights, acquiring both bone marrow aspirate and biopsy samples during the test is standard practice. A skilled clinician will typically perform a bone marrow inspection with minimal discomfort and pain to the patient. The bony structure of the human bone is composed of irregular trabeculae that create voids containing hematopoietic cells, supporting connective tissue and adipose cells [4]. In children, hematopoietic bone marrow is present throughout the skeleton, but in adults, it is limited to the axial bones. The posterior iliac crest is the ideal site for marrow extraction due to its ease of performance, convenience and safety. However, in cases where the posterior iliac crest is compromised by disease or inaccessible due to factors like morbid obesity or patient positioning limitations, it is important to explore alternative sites for marrow procurement [5]. Other potential sites for marrow procurement include the anterior iliac crest, suitable for children and adults, the sternum (limited to adults and for aspiration only), and the tibia, which applies only to infants. These alternate locations might be evaluated based on specific patient characteristics

and requirements. Initially, BMB is being carried out with a typical needle and syringe device. Needles are extensively employed in various medical procedures that involve minimally invasive surgery and percutaneous techniques. These procedures include tissue biopsies, BMB, regional anesthesia, drug delivery, and BMA [6-8]. Needles serve as ubiquitous tools in these applications. BMB is a diagnostic technique that may be performed using a palpation approach, allowing real-time evaluation without requiring a skin incision. This method has the benefit of assessing bone marrow in a single session. This technique is most suited for tumour monitoring and assessment, encompassing both malignant and benign conditions. The needle employed for trephine biopsy features a hollow inner section and offers significantly improved efficiency compared to standard needles frequently used in other procedures. During a trephine biopsy, medical professionals commonly use 11-gauge and 13-gauge needles. This procedure yields a sample suitable for cytological examination, with the possibility of developing a cell block for further analysis. Figure 1.1 depicts a schematic representation of a BMB technique using a biopsy needle targeting the posterior ilium crest. The biopsy needle is inserted into the desired area for inspection, and as the needle is moved back and forth, a negative pressure is generated inside the biopsy needle (refer to Figure 1.1). The needle movement causes the sample to dislodge from its original location, allowing it to be drawn into the needle through suction.

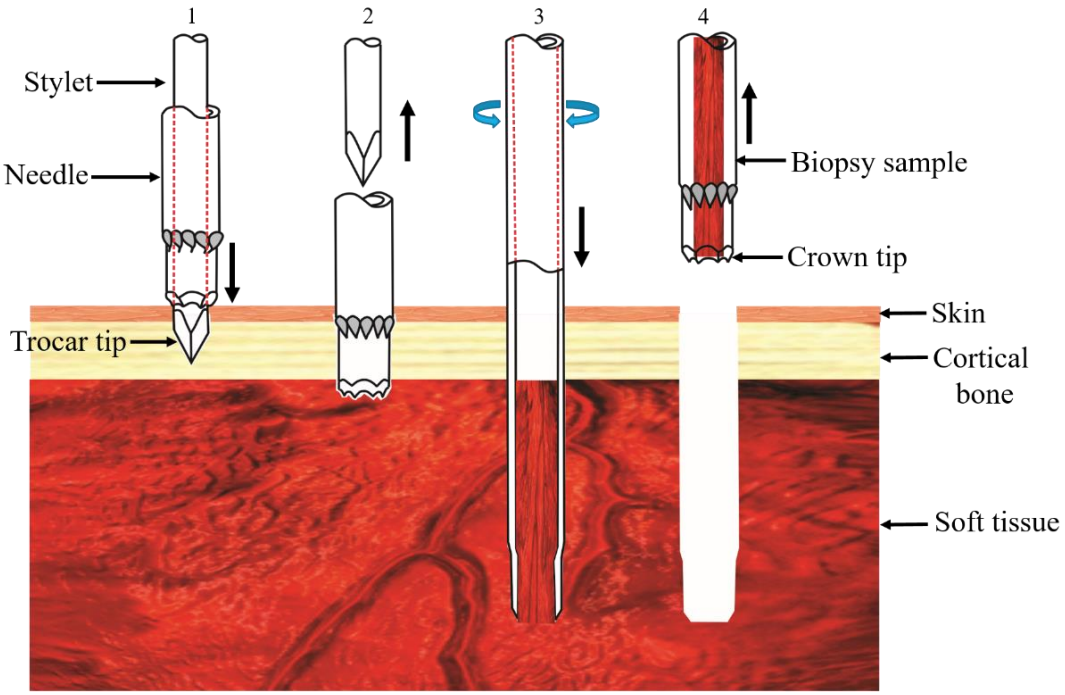

Figure 1.1: Schematic diagram of the biopsy process. (1) The biopsy needle with stylet is introduced into the bone, (2) The posterior ilium cortex is pierced with the mild rotating motion of the needle, (3) After the piercing is accomplished, the stylet is introverted, (4) Once sufficient depth is reached, the needle is revolved numerous times over its extended axis and introverted with a conventional pull

A previous study has suggested that BMB should be used to test marrow circularity and diagnose Hodgkin's disease and metabolic bone disorders [9]. However, the standard procedure of BMB does have certain drawbacks. Patients often experience discomfort and pain during the procedure due to the force needed to puncture the bone and acquire a tissue sample. In addition, samples acquired through conventional needles cannot consistently yield adequate material for proper evaluation or effective monitoring. This can lead to problems including pain, anxiety, inconclusive results, needle deflection, the need for repeat biopsies, and tissue deformation [10, 11]. To address these difficulties and improve the effectiveness and satisfaction of BMB patients, I have been motivated to evaluate alternate needle designs. The present research draws inspiration from natural mechanisms and structures observed in diverse organisms, including insects and animals, to develop bio-inspired needle designs that have the potential to enhance the BMB procedure. One intriguing observation that drew our interest is the trephine mechanism in honey bees and mosquito proboscis (refer to Figure 1.2).

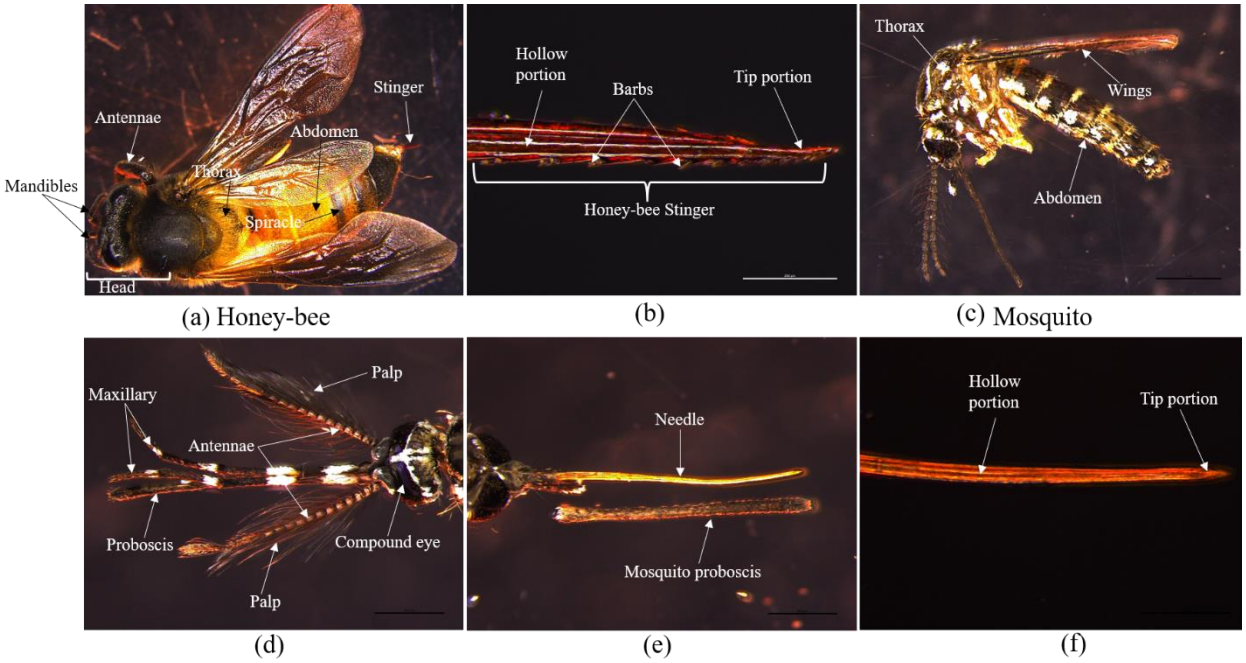

Figure 1.2: Diagrammatic representation of honey-bee and mosquito anatomy

The trephine mechanism observed in honey bees, characterized by their stinger-like structure and rotational motion, provides valuable insights into achieving efficient and precise insertion. The potential to overcome the limitations associated with traditional needles motivates the study and design of alternative needles for BMB. By integrating bio-inspired features into the needle structure, there is an aspiration to make the BMB procedure less invasive, thereby minimizing pain, patient discomfort, the need for repeat procedures, needle deflection and tissue deformation. Furthermore, bio-inspired needles have the potential

to facilitate more efficient specimen collection, leading to the acquisition of higher-quality samples. This, in turn, can contribute to more precise diagnoses and improved monitoring of blood diseases.

1.1.1. Historical perspective

Dr. John Dalrymple, hailing from Dublin, Ireland, was among the pioneering individuals conducting microscopic bone tissue studies in pathological conditions. In 1846, Dr. Dalrymple conducted a review of a bone sample obtained from a patient with multiple myeloma under the care of Dr. William Macintyre [12]. The bone marrow samples extraction technique for pathological evaluation was initially introduced by G. Pianese in 1903. Pianese utilized femoral trephination to obtain bone marrow samples [13-15]. Similar approaches were described in subsequent decades by Ghedini from Genoa, Italy, in 1908 and Peabody in 1927 [16]. These individuals also described methods involving bone marrow sampling for diagnostic purposes. Many researchers were discouraged by the absence of active bone marrow in the tibia. However, in the 1920s, Carley Paul Seyfarth and Mikhail J. Arinkin established the efficiency of sternal needle penetration as an outstanding approach for collecting clinical bone marrow aspirate samples, revitalizing interest in bone marrow sampling [15, 17]. During the early 1930s, Custer [18] emphasized the diagnostic significance of biopsy imprints, commonly referred to as "touch preparations," as well as histologic portions of sternal bone, alongside preparations for smears. Custer's technique involved the extraction of a 1 cm diameter disc from the ventral sternal plate, which necessitated a complex intraoperative process. BMBs were not widely conducted until 1958 when McFarland and Dameshek [19] introduced a more straightforward procedure using the Vim-Silverman biopsy needle. This advancement resulted in an increase in the number of BMBs performed. Subsequent modifications of the Vim-Silverman needle by researchers, viz., Swain, Westerman, Schaadt-Fischer, Jensen, Jamshidi, and others have contributed to reducing the pain associated with the procedure, enhancing the retention rate of biopsied samples and yielding larger core samples [20-23]. Recent technological advances led to the development of bone marrow biopsy needles with specifically designed cannula and stylet tips. These designs make cortical bone penetration easier. Internal core collecting mechanisms have also been added into these needles to successfully separate the biopsy while avoiding the core specimen from being lost during needle removal [24, 25]

1.2 Research goals and approach

The main objective of this thesis is centered around enhancing BMB needles to achieve a less invasive and more comfortable procedure for both patients and doctors. The aim is to develop improved needle designs that facilitate early cancer detection and other diseases during bone marrow biopsies. The goals for fulfilling this aim are listed below:

1. A prospective survey on bone and bone marrow trephine biopsy aims to determine actual and physical problems associated with BMB procedure. The objective is to obtain an in-depth comprehension of the process and assess its potential utility in enhancing patient care.
2. This thesis focuses on design and development of different bio-inspired trephine biopsy needles modeled based on the stinger and proboscis of honeybees and mosquitoes.
3. Quantification of insertion and extraction forces experienced during the BMB using FEM-based analysis.
4. FEM-based analysis of
    a) different challenges in needle insertion, such as tissue deformation and bone damage, to achieve desired targeting accuracy.
    b) needle deflection, and different stresses induced during bone marrow biopsy.
5. Design and develop an Artificial Intelligence (AI) tool that aids clinicians in their decision-making process by providing assistance in the selection of an optimal biopsy needle for BMB procedures.

1.3 Originality/Novelty of the work

The researchers developed models to replicate the process of inserting a needle into soft tissue in various experiments. However, their primary emphasis was not on creating a comprehensive model incorporating multiple layers to analyze the forces involved in needle-tissue interaction. This work examines the interaction forces between a needle and a combined multi-layered domain of skin and bone tissue (specifically, the iliac crest layer). The objective is to evaluate the needle-tissue interaction forces in the context of the BMB method. The results obtained from this research serve as a basis for developing more advanced models essential for gaining a deeper comprehension of the complex dynamics involved in the interaction between a BMB needle and the combined skin-bone tissue during the biopsy procedure. Utilizing these models can expedite the design and optimization of physically used BMB instruments, thereby minimizing the need for extensive trial-and-error approaches. This reduces the required trials and helps minimize patient discomfort and pain during the BMB procedure. The concept of employing bioinspired honey bee and mosquito proboscis needles for BMB procedures is an emerging idea that takes inspiration from the natural structures and mechanisms observed in these insects. It represents a novel approach in the field, harnessing the unique characteristics of these biological systems for potential application in medical procedures. The aim is to create needles replicating the efficient and minimally invasive properties observed in honey bees and mosquito proboscises.

1.4 Dissertation overview

The structure of this dissertation is detailed below:

Chapter one: Introduction to the problem, historical perspective, its magnitude, and why it exists have been detailed. The work's goals and novelty for fulfilling this thesis's aim have been explained.

Chapter two: The technology of BMB and the background of the thesis questions are detailed in this chapter. In-practice improvisations and their drawbacks have also been detailed to overcome the BMB problems discussed in the first chapter.

Chapter three:

In this chapter, methodologies taken to address the objectives of this thesis have been detailed. This chapter also discusses and elaborates statistical, mathematical, geometric, and numerical models of the problems.

Chapter four:

Herein, results corresponding to the studies performed in this thesis have been presented and discussed.

Chapter five:

The whole dissertation has been concluded by summarizing the significant results and their implications. The future scope of this study has also been discussed in this chapter.

Chapter 2

State of the art and literature review

In this chapter, we begin with the principle, technology, and technique of the BMB, which will provide a context for understanding the significance of thesis objectives.

2.1 Principle of BMB

The principle of a BMB procedure is to procure a specimen of bone marrow tissue to make a diagnosis or conduct further evaluations. Bone marrow, a crucial body component, is a soft and spongy substance found within specific bones [26]. It is essential for the development and growth of blood cells. Medical professionals can examine various problems such as infections, blood disorders, systemic diseases, and malignancies by analyzing the cell structure of bone marrow [27]. The patient is normally positioned on the back for a sternum biopsy, whereas patients are positioned on their left or right side or stomach during a hip bone biopsy. To ensure the patient's comfort, local anesthesia is delivered where the needle for the biopsy will be penetrated, essentially numbing the area. The healthcare expert skillfully creates a tiny incision in the skin and carefully inserts the biopsy needle into the bone using a specific needle such as a trephine or Jamshidi [1]. The needle is then guided deeper into the bone, reaching the bone marrow cavity that houses a combination of solid and liquid constituents of the bone marrow. After ensuring the needle is correctly positioned, the medical professional carefully rotates it while applying suction to obtain a core specimen of bone marrow tissue [28]. The healthcare professional may remove numerous samples from various sites inside the bone to obtain an accurate representation of the bone marrow. The obtained bone marrow specimen is carefully placed into a specialized container comprising a cylindrical core comprising cells and bone marrow components. The container is subsequently brought to a laboratory for further investigation and evaluation. The pathologist scrutinizes the bone marrow specimen using a microscope in the laboratory and performs a series of tests to determine the cellular composition. During the examination, the pathologist searches for deviations in the type and quantities of blood cells, the presence of malignant cells, or other types of pathological diseases [29]. The fundamental principle underlying a BMB is to acquire an appropriate amount of bone marrow tissue. A pathologist analyzes this sample to address various blood-related illnesses and ailments identified efficiently.

2.2 Technology of BMB

The technology and components utilized in bone BMB procedures have seen minimal changes since its introduction in clinical settings. The fundamental principles and equipment employed for BMB have

remained largely unchanged. The major components are – a) a biopsy needle and b) local anesthesia. Let us briefly go through these components that would help better understand BMB.

2.2.1 Biopsy needle

BMB needles are custom-designed medical instruments that extract bone marrow samples to diagnose medical conditions. These needles penetrate the bone, extracting a small section of both bone and bone marrow for further examination. A Jamshidi or similar needle is used to get a bone marrow core biopsy from the back portion of the iliac crest or other suitable locations. It is then processed in the same manner as other surgical specimens. There are several BMB needles available, including manual and powered variants [30]. Factors such as healthcare provider preference, patient characteristics, and the nature of the procedure being conducted influence the selection of the appropriate needle.

Manual BMB Needles:

1. Jamshidi needle: Among the frequently employed manual BMB needles, this particular one stands out as a popular choice in clinical practice. This manual BMB needle comprises a sharp, beveled tip and a hollow cannula, both essential components for its functioning. The needle is inserted into the bone and a rotating or twisting action is used to obtain the bone marrow sample. This action makes it easier to obtain the necessary bone marrow samples.
2. Ostycut needle: This manual biopsy needle is designed with a trocar-like tip, enabling smoother and more effortless penetration into the bone during the procedure. Renowned for its stability throughout the biopsy procedure, this manual needle is highly regarded for maintaining steady positioning and control.

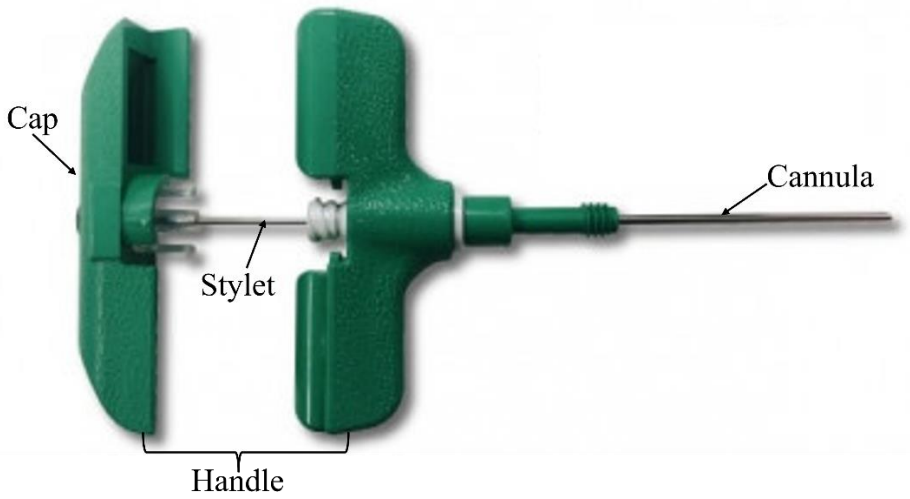

Figure 2.1: Pictorial representation of ostycut trephine biopsy needle

Powered BMB Needles:

1. On control BMB needle: A powered biopsy needle system is an example of the advanced medical devices available for biopsies. This biopsy needle device, including a motorized driver, uses controlled bone penetration, lowering the required force and improving patient comfort throughout the procedure.
2. MAX-CORE biopsy needle: This alternative-powered BMB needle was created to achieve a regulated and consistent collection of bone marrow samples. This device utilizes a powered driver for the biopsy procedure, enhancing its functionality and efficiency.

BMB needles are usually available in various diameters and lengths to fit different patient anatomy and biopsy locations, providing flexibility in selecting the most appropriate alternative. These needles, often made of stainless steel or other strong materials, are chosen for their remarkable strength, sharpness, and longevity, assuring optimal performance during BMB procedures [30].

2.2.2 Local Anesthesia

A local anesthetic provides numbing sensation to the skin and periosteum at the site where marrow procurement occurs. Lidocaine or a comparable local anesthetic may be utilized, provided the patient has no history of adverse reactions to the medication. Ensuring enough time to obtain complete local anesthesia can reduce discomfort. A 10 mL plastic syringe, equipped with a 22-gauge, 1-1/2-inch needle, is used to draw 2 mL of sterile 8.4% sodium bicarbonate solution (1 mEq/mL) and 8 mL of sterile 1% lidocaine hydrochloride during the procedure [1]. The addition of sodium bicarbonate buffers the lidocaine solution, thereby reducing the burning pain induced by the acidic nature of the lidocaine solution [1]. Afterward, the 26-gauge needle is substituted with a 22-gauge needle, and the operation is repeated by gently moving the needle through the skin and subcutaneous tissue around the center of the papule until the periosteums surface is reached [1]. A 2-5 mL of buffered lidocaine is commonly injected to anesthetize a circular area of the periosteum. To verify enough local anesthesia, the periosteum can be gently probed with the sharp tip of the needle to confirm no remaining sensitive regions [1]. A further 1-2 mL of lidocaine may be necessary if severe pain occurs [1]. Considering the potential occurrence of anaphylactic reactions even in patients without a prior history of allergies, it is essential to have an emergency kit readily accessible, containing an airway, injectable epinephrine, and hydrocortisone, for immediate use when needed [31].

2.3 Technique

The minimally invasive bone marrow biopsy procedure typically consists of three sequential steps:

2.3.1 Pre-planning

Numerous key elements are required in the pre-planning phase to prepare for a conventional trephine BMB clinical procedure appropriately. Before performing the trephine BMB clinical technique, it is required to evaluate the patient's medical history, current medicines, and any known allergies to confirm their suitability for the treatment [32]. In order to get informed consent from the patient, a full explanation of the goal, potential dangers, and anticipated benefits of the trephine BMB operation is required. It is essential to have the necessary equipment and supplies readily available for the trephine BMB procedure, including the appropriate biopsy needle, local anesthetic, sterile drapes, gloves, syringes, and specimen containers [1]. The trephine BMB operation should be carried out by qualified healthcare professionals with prior expertise doing such biopsies. These specialists should be well-versed in the safety precautions involved with the process and well-trained in using a specific biopsy needle. Based on the patient's factors, the anesthesia requirements for the trephine BMB procedure, such as the type and dosage of local anesthetic, should be determined accordingly [32]. It is critical to have an immediately available emergency pack that contains airway tools, injectable epinephrine, and hydrocortisone to guarantee emergency preparation during the trephine BMB process. This kit should immediately be available for urgent use, if unexpected situations arise.

2.3.2 Typical trephine BMB clinical procedure

The Jamshidi needle, introduced in 1971, is the most commonly utilized needle for performing marrow biopsies. However, several other needles are available for this procedure [33, 34]. The Jamshidi needle has a radially tapered tip that allows marrow tissue to enter the needle without clogging the tip, providing smooth and uninterrupted sample collection. Innovations in BMB needle design have incorporated tapered, sharp cutting edges for enhanced efficiency in bone penetration and reduced pain, along with core-securing devices to minimize core damage and the risk of leaving the core in place during specimen extraction [24, 25]. The BMB is performed using the same skin incision site as the marrow aspiration, but the biopsy needle is angled differently to access and sample a distinct area. Typically, the BMB needle, being of a larger caliber, necessitates more force than the aspirate needle during the procedure. Before performing the bone marrow examination, the hematologist briefed the patients regarding the procedure and obtained written informed consent. Patients were requested to lie in a prone position on an examination bed, and specimens from the posterior iliac crest were obtained. Before taking the trephine biopsy, a bone marrow aspiration sample was obtained using a bone marrow aspiration needle (15G/16G for adults, 18G for pediatric patients) and a 20-ml syringe. A hematologist performed

the procedure with the assistance of an operator who swiftly prepares bone marrow films and fills various vials (anti-coagulated with ethylene diamine tetra acetic acid (EDTA) and heparin) for further analysis. After the aspiration, the biopsy was performed from the iliac crest using appropriate trephine needles with varying lengths and diameters. To regulate the penetration depth during the process, the biopsy needle is grasped with the handle in the palm and the tip of the index finger rests on the shaft of the needle. To begin the procedure, the needle is inserted through the puncture site in the skin, steadily advanced with consistent pressure until it reaches the periosteum, and then rotated into the surface of the bone cortex. Once the needle gets anchored into the bone, the stylet will be removed, and the cannula (i.e., outer hollow needle) further penetrates into the bone to collect the bone marrow sample. The collected sample can be seen in Figure 2.2(a). A decrease in resistance typically indicates that the needle has entered the marrow cavity. Continuing with a back-and-forth rotation, the needle is further advanced, approximately 1-2 cm. To separate the biopsy core from the surrounding bone, the needle is rotated vigorously in a complete 360° and 180° clockwise or anti-clockwise motion multiple times while applying gentle pressure. A reduction in rotational resistance usually indicates that the core has detached from the surrounding bone during the process. The obturator is inserted into the distal end of the needle, and then, with gentle pressure, the core biopsy is pushed through the hub of the needle onto the glass slide. Following this, biopsy imprint preparations were made from the BMB core. This method involves placing the fresh core biopsy material on a new microscope slide (see Figure 2.2(b)). As seen in Figure 2.2(c), the biopsy sample is carefully placed against a second fresh microscope slide, then the slide is slowly rolled from side to side. It is suggested to produce two or three specimens with various imprints on every plate. Cells on the surface of the biopsy core adhere to the microscope slides when imprint slides are being made. The bone marrow sample is subsequently immersed in formalin solution (can be seen in Figure 2.2(d)) to effectively preserve its morphology for an extended period. The imprint slides can be stained using the May Grunwald-Giemsa method for morphologic inspection or cytochemical staining and analysis (refer to Figure 2.2(e) and (f)). Approximately 5 to 6 ml of 1-2% lidocaine was utilized for local anesthesia, while ketamine and midazolam were given for sedation in children at a dose of 0.1 mg/kg to 1 mg/kg. Each patient (or the guardian in the case of children) was informed about the risks of local anesthesia/sedative drugs.

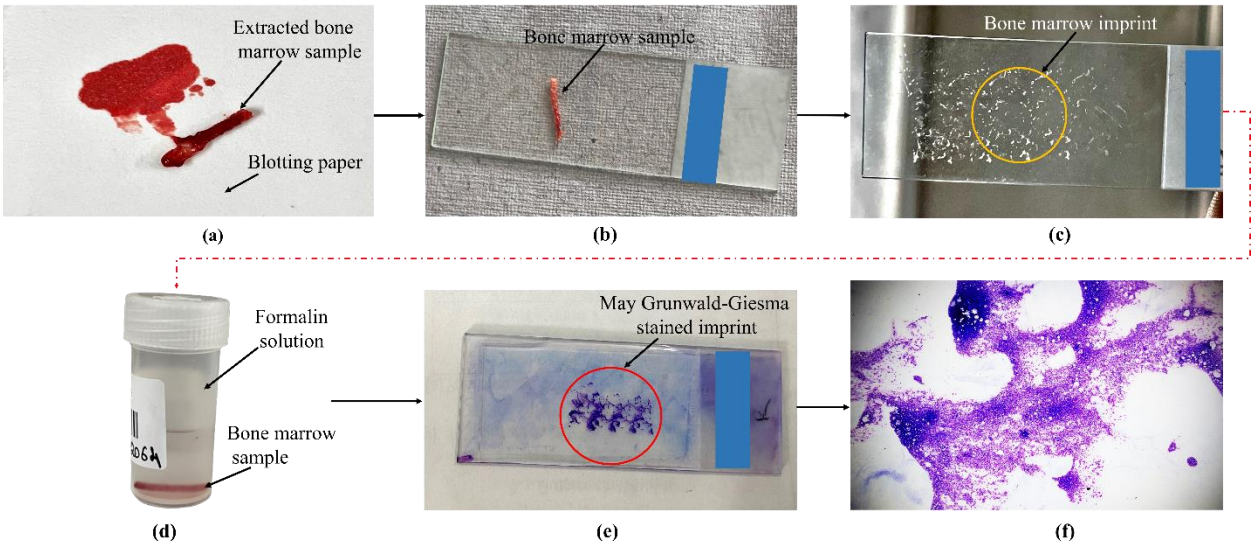

Figure 2.2: Pre-and post-processing procedure of trephine biopsy

2.3.3 Post-Procedure Care

Once the marrow specimens are obtained, it is necessary to address any bleeding, tidy up the procedure site, dispose of the needles appropriately in a sharp's container, and apply a bandage over the site. In the absence of bleeding issues, post-procedure care covers the skin puncture site with sterile gauze and exerts mild but firm pressure on the skin and the underlying bone for roughly one minute. If bleeding persists after removing the gauze, further pressure is administered. The gauze and fenestrated drape are then thrown in a sharp's disposal receptacle. To ensure the complete removal of povidone-iodine, the skin is meticulously wiped with isopropyl-soaked swabs. It is important to eliminate any residual povidone-iodine as it can potentially cause itching and trigger allergic reactions in the future. A folded gauze square is placed over the treatment site, and at least two pieces of elastic surgical tape of roughly 2-3 inches in length are attached. To avoid further bleeding, the patient is placed in supine position with their weight centered on the incision for at least 30 minutes [35]. In the event of abnormal bleeding during a marrow operation, pressure is used until the bleeding stops. Following that, a pressure dressing is applied, and the patient is placed in a supine position for at least one hour [36]. It is normal for the procedure site to exhibit mild tenderness for a few days. However, if patients notice swelling, significant tenderness, or continued bleeding, they are advised to contact their physician promptly.

2.4 Complications of the BMB procedure

The bone marrow examination is a procedure with minimal risk of complications and a low chance of causing health issues. Fatalities are infrequent with sternal marrow aspiration and extremely rare with bone marrow aspiration with iliac crest biopsies. Death resulted from cardiac tamponade caused by

laceration of the right ventricle or intrapericardial aorta in numerous recorded cases of fatal sternal aspiration [37-39]. Other distinct complications associated with sternal marrow aspiration include the occurrence of pulmonary bone marrow emboli, the development of a tumor mass in the sternum, and sternal-manubrial separation [40, 41]. Applying a small pressure dressing to the biopsy site helps minimize the risk of hemorrhage, a rare complication of BMB procedures conducted at any location [42, 43]. Patients with osteoporosis, Paget's disease, and other bone-related illnesses have the highest risk of bleeding problems during bone marrow aspiration and biopsy operations. A case report documented a fatal occurrence of intraabdominal hemorrhage after bone marrow aspiration and biopsy in a patient diagnosed with multiple myeloma [44]. The incidence of needle breakage or handle separation during bone marrow needle insertion is an extremely rare complication in the marrow procurement procedure. If the needle fragment cannot be readily extracted using a hemostat, it is important to inform the patient about the incident and seek a surgical consultation for further guidance and assistance. In certain rare cases, patients experienced numbness and weakness in one lower extremity after undergoing a bone marrow examination. This occurrence is believed to result from potential infiltration of the sacral nerve plexus. These patients, who exhibited moderate obesity and relatively low pain tolerance, required additional lidocaine for effective local anesthesia during the procedure.

2.5 Literature review

2.5.1 Literature search strategy and data extraction

To perform this survey, Science direct, MEDLINE, Google Scholar, Research Gate, and PubMed have been searched, to collect relevant research articles up to 2023. The data for the current analysis has been identified without language or time restriction. The search engines have been checked by employing various terms like: "Bone marrow" AND ("BMA" or "BMB") AND ("fine needle aspiration" or "trephine biopsy") AND ("conventional" or "bio-inspired needles") AND "BMA and biopsy site." The research articles have been chosen for full-text study based on their abstracts and titles. The bibliographies of some research publications have been manually searched to enhance the yield of related studies. The data extracted from each incorporated article have been the year of publication, study area, author, needle design, insertion forces, needle deflection, bio-inspired designs, pain, needle size, suction method, repetitions required, complications, etc. The search engines have been used to identify 2086 research articles; 1806 have been screened for non-duplication citations. In addition, 84 and 1557 articles have been excluded based on the full-text review and information in the abstract and title, respectively. Eight research articles have been added after studying references from related articles. Finally, 39 articles met all inclusion criteria for the survey concerning the accuracy of diagnosis of BMA and biopsy.

2.5.2 Conventional biopsy needles

Needles are commonly encountered medical instruments with extensive application in minimally invasive surgical and percutaneous procedures. These procedures include administering injections, performing regional anesthesia, collecting blood samples, conducting biopsies, and implementing brachytherapy [45-47]. Depending on the specific medical procedure, needles are available in a diverse range of tip configurations. These configurations include bevel-tip, lancet tip, back-bevel tip, trocar, Fransen, conical, and many others. The choice of needle tip configuration is determined by the particular requirements of the medical procedure [48]. Minimally invasive surgical procedures frequently employ a technique whereby a hollow needle, known as a cannula, is inserted into the body to reach a specific target. This procedure serves two primary purposes: removing tissue samples, also known as biopsies, or delivering drugs to the intended site within the body. Precise needle placement is critical to ensuring accurate diagnosis and treatment by minimizing tip misplacement during medication administration or biopsy, which might affect accuracy and efficacy. Various factors contribute to the inaccuracy of needle placement or deviation from its intended path, including tissue deformation caused by factors such as inhomogeneity and anisotropy, physiological processes like fluid flow and respiration, as well as anatomical obstructions [49-51]. Achieving success in minimally invasive surgical procedures is influenced by additional factors, including the force and friction experienced by the needle tip during insertion, which can cause tissue deformation and result in needle deflection from the intended target [52]. In recent years, extensive research has been undertaken to examine the interaction between needles and tissues, particularly emphasizing needle insertion tests utilizing soft gel models [53-54. Dimaio et al. [55] inserted needles into a thin tissue phantom with a grid of black dots on its surface. They could quantify and confirm the tissue deformation exhibited in the tissue FE model by using image processing techniques to trace the motions of these dots. Misra et al. [56] conducted an extensive literature review focusing on utilizing the FE method to model needle-tissue interaction and its applications in invasive and non-invasive surgical simulations within the medical domain. This research aims to study the impact of certain factors on the dynamics between a needle and soft tissue, such as diameter, bevel angle, needle insertion speed, needle tip shape, and gel elasticity. In a study conducted by Jiang et al. [57], experimental findings revealed that manipulating parameters such as diameter, bevel angle, insertion speed, and tip shape during needle insertion led to changes in the forces experienced by the needle and the occurrence of gel rupture. The experimental studies investigating needle force interactions with tissue were analyzed in a comprehensive review conducted by van Gerwen et al. [58]. The review revealed that typical peak forces observed during these interactions range from approximately 0.1 to 10 N. Furthermore, the study emphasized that blunt-tipped needles, despite having smaller diameters, generate higher peak axial forces than conical, diamond, and bevel needles. Various considerations are necessary to conduct FE analysis of

needle-tissue insertion in surgical simulation, including material mechanical behavior, non-linear material and geometry effects, material rupture, and boundary conditions [49-51]. Then, Oldfield et al. [59] introduced an FE approach incorporating a cohesive zone element model to simulate tissue rupture and needle-tissue interaction, specifically addressing crack propagation using cohesive elements. In this technique, prior to needle insertion, it is necessary to define the cutting path and subsequent needle penetration path. Additionally, initiating a crack requires the definition of a notch or crack on the surface of the bulk material. A limitation of this method is that the needle path is not predetermined before insertion, which can result in the distribution of cohesive elements across a region with fine elements. The presence of cohesive elements distributed across a region with fine elements can increase computation time and pose challenges in accurately defining the crack propagation path. Yamaguchi et al. [60] presented an alternative FE approach based on Arbitrary Lagrangian Eulerian (ALE) method. This approach was developed primarily for fluid-based analysis, which includes significant deformations and fractures inside continuum models. This method offers advantages such as handling arbitrary enclosing boundaries, adjusting zoning for optimal resolution, and achieving improved accuracy in situations where fully Lagrangian calculations are not feasible while also enabling larger time steps compared to explicit methods [61]. The study demonstrated that the ALE-based FE method allows for dynamic analysis of needle insertion and tip geometries, enabling examining needle-interaction forces and needle deflection within a soft phantom tissue environment. Liang et al. [62] obtained around 80% accuracy in modeling a 40-mm insertion for prostate deformation by including a needle deflection model in the FEM simulation. Although FEM offers feasibility in studying tissue deformation, the intricate nature of needle-tissue interaction results in significant computational expenses and constrains the fidelity of the model. Novel experimental techniques have been devised to quantify tissue deformation during needle insertion, offering valuable insights into the dynamics of needle-tissue interaction. Kerdok et al. [63] created a silicone rubber phantom containing embedded fiducial markers in Teflon spheres to establish a physical benchmark for tissue simulation. These markers allowed for the correlation of the deformed phantom with computer tomography images, enabling the validation and calibration of tissue simulations. Oldfield et al. [64] utilized a tissue phantom containing embedded aluminum oxide particles and employed a laser illumination system to illuminate the cutting plane of the needle. A modified digital image correlation approach was developed to follow particle mobility and correctly evaluate the mechanical behavior of tissue during needle insertion. Maurin et al. [65] investigated the correlation between axial force and penetration displacement depth during surgical needle penetration and withdrawal. Their study focused on examining the penetration resistance of needles when puncturing a living liver. However, researchers did not specifically address the variation in penetration resistance associated with different needle tip shapes. As a result, studying the mechanical features of needle insertion provides a solid foundation for enhancing

the design of medical needles. An empirical model for the unilateral insertion force of needles was developed by Okamura et al. [66]. This model combines the forces associated with capsule stiffness, friction, and cutting, resulting in a comprehensive understanding of the factors influencing the insertion force. Based on their approach, the stiffness force exists before to puncturing the capsule, but the friction and cutting forces appear immediately following the initial puncture. Hing et al. [67] devised a system that utilizes conventional FEM and ABAQUS software to forecast the movement of soft tissues and the associated force components. In this study, two C-arm fluoroscopes were employed to capture images of fiducial markers and observe needle bending. Misra et al. [68] evaluated the effect of axial force on tissue rupture toughness, tissue elasticity, and needle tip bevel angle. They incorporated these physical parameters into a FEM-based model using contact and cohesive zone models. Kobayashi et al. [69] developed an alternative model that included precise material characteristics, as well as viscoelastic and non-linear behavior. By employing FEM, the researchers validated the correlation between needle displacement and insertion force. Additionally, they assessed the velocity dependence of this relationship during puncture occurrences. Yan et al. [70] introduced an online estimator that utilized a series of interconnected local polynomials within finite segments. This estimator was designed to approximate the depth-dependent tissue parameters using force measurements. In order to validate the model, an 18GA needle with a trihedral tip was inserted at a constant insertion speed. Barbe et al. [71] developed an alternative online technique based on the recursive least squares methodology. The established system was combined with the Kelvin-Voigt viscoelastic interaction model, which included time-varying characteristics. This integration aided in the reconstruction of force evolution throughout the insertion process. Yen et al. [72] described a telemanipulation device to aid soft tissue penetration during medical operations. The technology interacts with the environment using a spinning arm built for needle insertion. They used velocity and acceleration data from encoder readings during a single test on a pig sample to build a simulation. Brett et al. [73] described an automated portable device that analyzes tissue type and deformation throughout the insertion procedure. Both recently dead pig and human lumbar samples were used to test the device. The ongoing improvement of reality-based tissue models, as detailed in this study, is predicted to increase their use in tissue simulation and robot-assisted surgical systems. This improvement will help increase the realism and performance of these systems.

Traditional BMB needles have limited efficacy in minimizing damage to tissue during the biopsy procedure. Conventional needles often rely on shear force and rigid structures to penetrate the skin-bone, which can result in higher levels of trauma and discomfort for the patient. Furthermore, their rigidity might make it difficult to traverse through intricate anatomical systems, perhaps leading to inadequate biopsy samples or an increased risk of complications.

2.5.3 Bio-inspired biopsy needles

Bio-inspired BMB needles are designed and developed with inspiration from biological processes to increase the efficiency and efficacy of the biopsy technique. These bio-inspired needles provide several benefits over traditional BMB needles. This bio-inspired needle shape enables easier entry into the bone marrow, decreasing tissue stress and minimizing patient pain. Bio-inspired BMB needles have characteristics that include serrations or barbs on the needle shaft. These features provide increased stability and grip during needle insertion, lowering the danger of needle slippage or deflection. Furthermore, bio-inspired BMB needles might include structures influenced by natural biological systems, such as suction or vacuum-assisted extraction, which can improve the effectiveness and precision of the biopsy procedure by allowing for the extraction of greater quantity and quality bone marrow specimens.

While various studies have focused on needle diameter and tip geometries, there has been limited exploration into altering the geometry of the needle body itself. Traditionally, the needle body has been conceived as a hollow cylinder, and only a few investigations have ventured into modifying its structural design [74]. Improving needle insertion performance is an ongoing objective in the medical community. Extensive study has demonstrated that the form and geometry of the needle have an important impact in determining the insertion force necessary for medical procedures [75-77]. Achieving precise targeting is crucial when using a needle for therapeutic delivery or acquiring biopsy samples for diagnostic purposes. Numerous research endeavors are underway to replicate insect stingers' penetration mechanisms, such as those found in honeybees [78-80] and mosquitoes [81]. These efforts aim to aid in the development of improved needle insertion techniques. Insect stingers offer the potential for revolutionizing needle design due to their evolutionary adaptation and proficiency in penetrating human tissue using various mechanical and dynamic insertion techniques. The study of insect stingers holds promise for enhancing modern needle designs by incorporating the efficient and effective strategies observed in nature [82]. To develop a painless microneedle with minimal insertion force and strong soft tissue adhesion, our research drew inspiration from the remarkable natural bio-microneedles that have evolved to fulfill these specific functions over time. By studying these natural adaptations, we sought to incorporate their advantageous features into our microneedle design. In the realm of nature, one remarkable example of an inherently painless microneedle is the mosquito fascicle. Female mosquitos, unlike males, have a specialized biological microneedle known as a fascicle that can pierce the skin of animals, including humans, easily. During the puncturing process, this biological microneedle never loses strength. The proboscis is an important mechanism female mosquitos use to puncture the skin and draw blood during feeding. The fascicle, which consists of six stylets, is an essential component of the proboscis. The labium, on the other hand, encircles the fascicle with its grooved shape. Gordon and Lumsden [83] conducted a study

examining the behavior of the mosquito fascicle during blood uptake from a frog web. Their findings revealed the remarkable flexibility of the mosquito fascicle, allowing it to bend and maneuver within the frog tissue. Anne [84] conducted a detailed analysis of the piercing fascicle in three mosquito species using a Scanning Electron Microscope (SEM). The study provided a comprehensive description of the morphological structure of the fascicle, offering valuable insights into its intricate details. Jones [85] examined the anatomy of the mosquito's proboscis and alimentary canal. Additionally, the research focused on investigating the feeding behavior of female mosquitoes. This study provided valuable insights into the physiological aspects of mosquito feeding. Previous studies on the penetrating process of the mosquito fascicle primarily focused on descriptive observations, lacking a comprehensive investigation into the underlying physics. The jagged structure of a mosquito's proboscis is a beneficial bio-microneedle that allows painless penetration into the skin for blood-feeding purposes. Kong and Wu [86,87] researched the insertion behavior of the Aedes albopictus mosquito fascicle. Their findings demonstrated that the mosquito fascicle could easily cut through the skin using vibrations, with an average insertion force of 18 μN. Ramasubramanian et al. [81] used a high-speed video imaging approach to detect the penetration of the mosquito fascicle into human skin in recent research. This novel technique yielded important insights into the dynamics of mosquito fascicle penetration in human skin. According to the researchers, the mosquito uses a non-conservative follower force in addition to the Euler compressive load to prevent buckling and accomplish effective skin penetration. The utilization of mosquito-inspired vibration has gained interest because of its capacity to lessen insertion forces and discomfort during the penetration process [88, 89]. Insertion force has been reduced using axial vibration on microneedles [90] and ultrasonic vibration on hypodermic needles [91]. To optimize the vibration for tissue cutting, the forces were tested by adjusting frequencies and amplitudes to determine their effects [92]. Bi and Lin [93] conducted a study to enhance needle position accuracy by investigating the effect of vibration during needle insertion to reduce deflection. The findings of this study were used to incorporate the mechanical and procedural components of mosquito-inspired vibration into the development of novel bioinspired needle designs. Cho et al. [94] conducted a comprehensive investigation on porcupine quills found in North America. The biological design of the quill allowed for easy insertion and strong tissue adherence, with the barbs playing a crucial role in enhancing the adhesion and significantly reducing the force required to penetrate the tissue. Numerous researchers have also examined honeybee stingers in their studies. Wu et al. [79] and Ling et al. [95] investigated honeybee stingers and barbs separately. The labium's protective sheath provides lateral support during insertion, improving stability and enabling penetration. Ling et al. [78] researched the sting behavior of worker honeybees. The study observed that the honeybee stinger directly penetrates the skin without the involvement of any vibration. The force required to penetrate artificial skin was extremely low, measuring approximately 1.34 mN. The stinger

exhibited elasticity, allowing it to easily recover its shape after being bent. While the sting behavior has been extensively described, further investigation is needed to understand better the mechanical function of the barbs on the stinger. Adding barbs on the stinger significantly lowered the penetrating force by reducing the frictional forces involved. In contrast, the average extraction force was approximately four times higher than acupuncture microneedles. This increase in extraction force can be attributed to the mechanical interaction between the barbs and the tissue [80].

2.6 Need of the work/ Gap in existing research

BMB procedures require sub-mm accuracy, but it is becoming technically and clinically challenging. In this technique, the needle insertion force damages and shifts the tissue inadequately sustained by the surrounding tissue. Another challenge while performing the procedure is that the needle bends during insertion, making tissue deformation more prominent. The tissue distortion and bending of the needle frequently lead to misalignment of the needle tip, leading to problems in achieving preferred aiming accuracy [96]. To overcome these clinical challenges, measuring tissue deformation during needle insertion is important to assist clinicians and medical robots understand the needle-tissue interaction and improving targeting accuracy.

Numerous research articles on the clinical performance of BMB have been published recently. However, the outcomes of these bone marrow investigations were never described based on anxiety, pain, type of needles, time taken to complete biopsy, bending of the needle, number of recurrences, bone texture, tissue deformation, etc. Related to this, there is still scope for further improvement, especially regarding the complexity of bone marrow inspection, pain, anxiety, diagnostic performance, etc. The main endpoint was the accuracy of the sample acquired during BMB, the number of needles that passed or deflected during the procedure, tissue deformation, and insertion/extraction force generated during the procedure.

2.7 Summary and Implications

The available literature on conventional and bioinspired BMB needles offers valuable insights into their design and performance. Despite their ubiquitous usage, conventional needles have certain limitations, including significant insertion forces and the potential to cause tissue damage. On the other hand, bioinspired needles are inspired by biological processes found in insects such as mosquitos and porcupines, which give greater penetration and tissue adhesion. Researchers have gained significant knowledge by studying the anatomy and mechanics of natural systems such as mosquito fascicles, honeybee stingers, porcupine quills, and others. This information may be used to improve the design and

performance of BMB needles. Bioinspired techniques have tremendous potential for lowering insertion forces, optimizing tissue penetration, and improving overall performance. Research on bioinspired needles has investigated diverse aspects, encompassing needle geometry, vibration techniques, and the structure of barbs. Utilization of non-conservative follower forces, barbs, and vibration techniques has demonstrated potential in reducing pain, enhancing targeting accuracy, and optimizing tissue cutting. The implications of this literature extend widely, as bioinspired needle designs have the potential to revolutionize medical procedures by mitigating patient discomfort and minimizing tissue trauma. Bioinspired needles, which incorporate nature-inspired elements such as barbs and vibration, represent a possible option for obtaining more efficient and least invasive medical procedures. Continued research and development in this field holds the potential for advancements in needle design, which can ultimately benefit patients and healthcare professionals by enhancing the effectiveness and safety of needle-based procedures.

The honeybee stinger and mosquito proboscis influenced the shape of our one-of-a-kind bioinspired needle. Incorporating strong barbs inspired by honeybee stingers and vibration during needle penetration inspired by mosquito proboscis minimizes insertion force. The distinctive characteristic of reduced penetration force observed in honeybee stingers motivated us to develop a unique bioinspired needle shape that could provide lower penetration force than traditional needles. An improved and precise design for the bioinspired needle has been proposed and presented by extensively evaluating the characteristics and constraints of distinct barb configurations, surpassing prior research efforts in this field. This study aims to develop a numerically feasible simulation model for a bioinspired needle inspired by the honeybee, allowing for accurate and reliable simulations. The proposed model aims to establish the correlation between the axial forces experienced by the needle and the depth of penetration during both insertion and extraction processes in soft tissue and bone. This study aims to improve the accuracy, reduce patient discomfort, prevent deflection and clogging, and enhance the efficiency of bone marrow biopsy procedures by developing a needle inspired by the honeybee stinger. The objectives of this study contribute to a better understanding of the challenges and outcomes of trephine bone marrow biopsy procedures, leading to improved effectiveness and patient care.

Chapter 3

Methodology

The majority of the research in this thesis has used numerical simulations as the primary methodology. Subsequently, this chapter discusses the numerical methods employed, following an overview of the methodology of the trephine bone marrow biopsy survey. Since the past two decades, numerous attempts have been made to investigate the risk factors, techniques, anxiety, concern biopsy specimen length, etc. during the BMB. Most studies on BMB focused on evaluating pain, considering perspectives from both pathologists and hematologists. Therefore, the existing research has not adequately explored crucial aspects such as anxiety, pain, needle types, biopsy duration, needle bending, recurrence frequency, bone texture, tissue deformation, crack propagation, and other relevant factors during BMB. Most of the research articles had considered comparatively small biopsy samples, and, it has been quite difficult to evaluate the diagnostic precision of BMB. Therefore, a survey has been conducted on BMB to identify the specific challenges clinicians and patients encounter during the procedure. The survey revealed that the needle material is not compatible with the bone marrow and forms plasminogen. The size of needle depends on the strength of the bone, and different needles have been used in children, young and older people. Needle strength has been poor and therefore it bends very frequently during biopsy. Therefore, there is a requirement of extensive research to explore and study. The issues identified in the BMB survey have been considered, and subsequent analyses were conducted using FE and Artificial Intelligence (AI) methodologies.

3.1 Materials and Methods

The current survey has been carried out in compliance with systematic survey and research article standards. The whole analysis has been carried out at PGIMER, Chandigarh according to the declaration of Helsinki.

3.1.1 Study design and data collection

The current survey has been conducted between March and April 2022 on patients undergoing trephine bone marrow biopsy at PGIMER Chandigarh. PGIMER is a large tertiary care hospital catering to patients from various parts of North India, having numerous departments, including the Department of Clinical Hematology & Medical Oncology (adult), Pediatric Hemato-Oncology unit in the Department of Pediatrics, and Department of Hematology (laboratory-based). The patients included were outdoor and indoor patients undergoing bone marrow procedures for hematological or non-hematological indications.

The trephine bone marrow biopsy procedure was performed by trained residents of the Department of Hematology, having experience of 1 to 6 years. Patients with a language barrier, syncope, and severe psychiatric disorder have been excluded from the present study. At the same time, during the procedure, a standardized questionnaire, as shown in Figure 3.1, has been systematically filled out by the author. The questionnaire contains 14 inquiries related to the personal experience of the patient and operator before, during, and after the biopsy. The information recorded before and during the procedure includes (refer to Figure 3.1): patient information (age, gender), trephine biopsy indication, biopsy location, anesthetic procedure, needle types, and needle bending (if any). Upon procedure completion, the operator has been asked to assess the patient's bone texture and pain level. Following this, a one-to-five-minute pressure was employed by the operator on the biopsy site to achieve hemostasis. For additional safety, patients were instructed to lie on their back in a prostrate position for 10 - 15 minutes to apply more prolonged pressure.

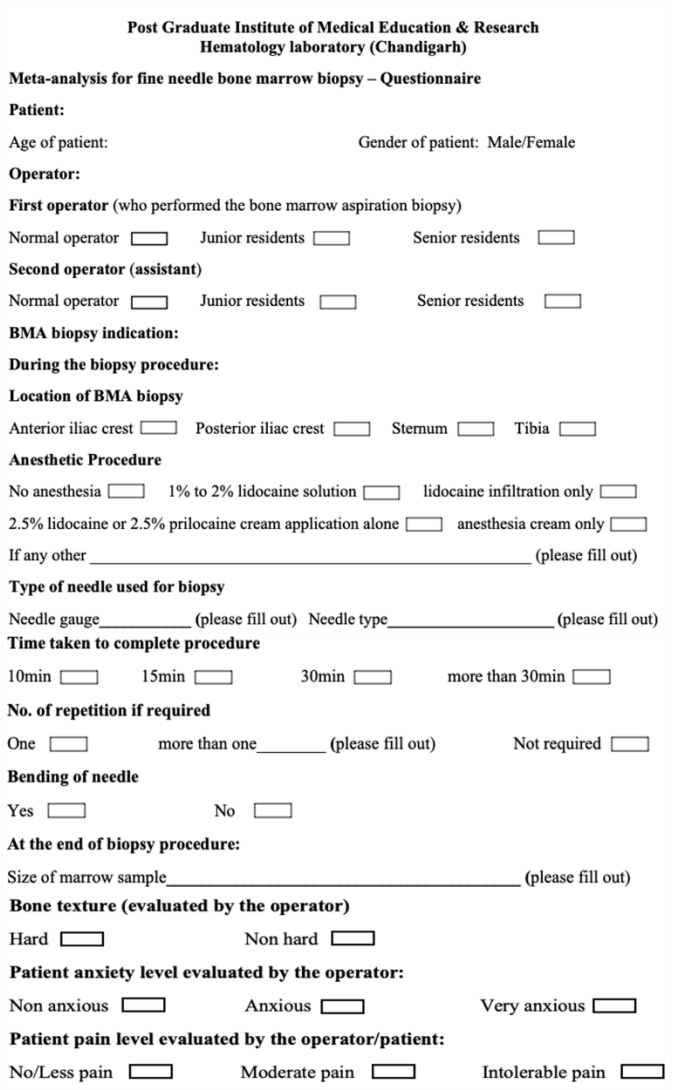

Post Graduate Institute of Medical Education & Research
Hematology laboratory (Chandigarh)

Meta-analysis for fine needle bone marrow biopsy – Questionnaire

Patient:

Age of patient: Gender of patient: Male/Female

Operator:

First operator (who performed the bone marrow aspiration biopsy)

Normal operator ☐ Junior residents ☐ Senior residents ☐

Second operator (assistant)

Normal operator ☐ Junior residents ☐ Senior residents ☐

BMA biopsy indication:

During the biopsy procedure:

Location of BMA biopsy

Anterior iliac crest ☐ Posterior iliac crest ☐ Sternum ☐ Tibia ☐

Anesthetic Procedure

No anesthesia ☐ 1% to 2% lidocaine solution ☐ lidocaine infiltration only ☐

2.5% lidocaine or 2.5% prilocaine cream application alone ☐ anesthesia cream only ☐

If any other _____ (please fill out)

Type of needle used for biopsy

Needle gauge_____ (please fill out) Needle type_____ (please fill out)

Time taken to complete procedure

10min ☐ 15min ☐ 30min ☐ more than 30min ☐

No. of repetition if required

One ☐ more than one_____ (please fill out) Not required ☐

Bending of needle

Yes ☐ No ☐

At the end of biopsy procedure:

Size of marrow sample_____ (please fill out)

Bone texture (evaluated by the operator)

Hard ☐ Non hard ☐

Patient anxiety level evaluated by the operator:

Non anxious ☐ Anxious ☐ Very anxious ☐

Patient pain level evaluated by the operator/patient:

No/Less pain ☐ Moderate pain ☐ Intolerable pain ☐

Figure 3.1: Questionnaire on trephine bone marrow biopsy

3.1.2 Patient population

Three hundred questionnaires have been filled out by the author, which include 157 (52.3%) adult male patients, 113 (37.6%) adult female patients, and 30 (10%) pediatric patients. The age of patients ranged from 2 months to 85 years (median age of 25 years). Major indications of trephine bone marrow biopsy were 39 (14.23%) patients with suspected multiple myeloma, 63 (22.99%) patients with suspected acute leukemia, 48 (17.52%) patients with suspected myeloproliferative neoplasm, 24 (8.75%) patients with lymphoma for staging and 28 (10.21%) patients with other bone marrow indications. The number of repetitions required has been documented and reported in the questionnaire if a patient is subjected to more than one pass during the biopsy procedure. Figure 3.2(a) shows the number of patients (n = 274) who underwent the trephine BMB with respective biopsy process notes and pathology reports. Similarly, Figure 3.2(b) depicts different indications that led the patient to undergo the trephine bone marrow biopsy.

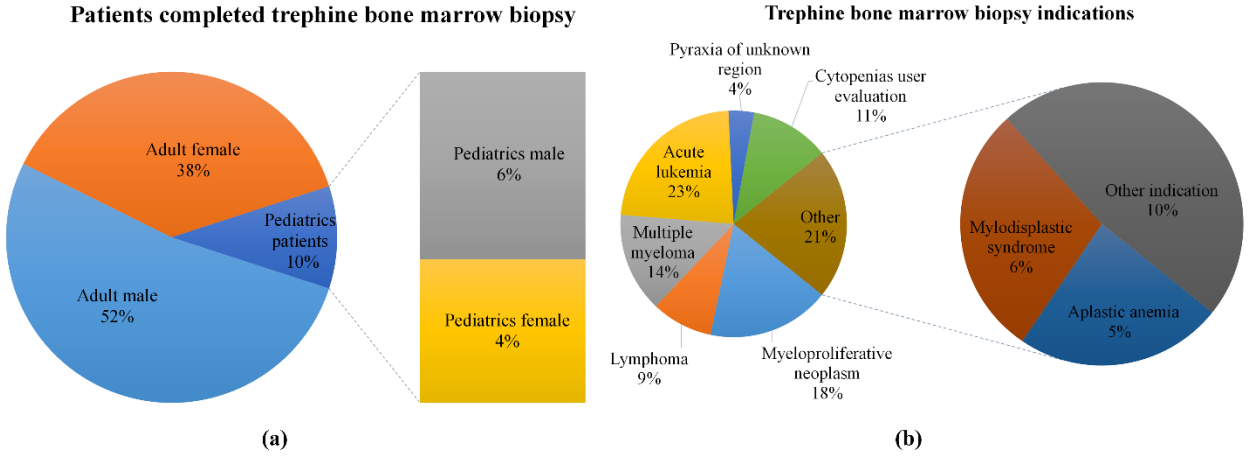

Figure 3.2: Chart representing (a) patients who completed BMB and (b) indications to perform trephine biopsy

3.1.3 Trephine bone marrow biopsy needles

Two distinct biopsy needle types, single and triple bevel, were used by the clinicians to smooth the trephine BMB procedure. The single bevel trephine biopsy needle was utilized in 264 biopsy cases, while a triple bevel trephine biopsy needle was utilized in 10 biopsy cases. As illustrated in Figure 3.3, the triple bevel biopsy needle has a two-piece T handle with procurement cradle, a triple crowned cannula tip with a trocar-tapered sharp-pointed stylet, and three bevels and six sharp cutting edges. A single bevel biopsy needle, on the other hand, has an elliptical stylet, a smooth handle, and a single bevel needle tip with two cutting edges (refer to Figure 3.3(a) and (c)). For adults, the trephine needle had a diameter of 11 G and a length of 10 cm. On the other hand, the trephine needle used was 13 G and 9 cm long for pediatric patients.

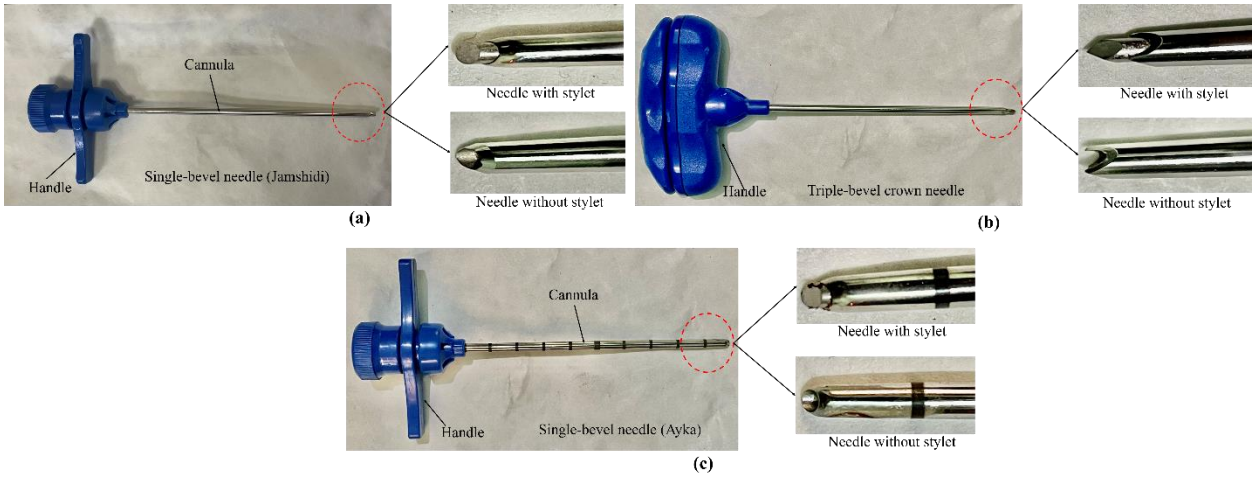

Figure 3.3: Pictorial view of (a) single-bevel adult biopsy needle, (b) triple-bevel crown tip, and (c) single-bevel pediatrics trephine bone marrow biopsy needle displaying the differences in handles, bevels, and stylets

3.1.4 Statistical analysis and sample size

To address the issue of potential bias, two independent investigators have extracted the data. A comparison of the statistical results and quality scoring has been made, and any discrepancy between the results led to a reanalysis of the original article. Finally, any unresolved issues have been settled by an independent investigator. The results have been presented as mean values with their associated standard deviations. To estimate the precision of the percentage of specimens with evaluable marrow of 4 mm or more, 98% confidence intervals have been considered. These intervals provide a range within which we can be 98% confident that the true population percentage lies. Bivariate logistic regression has been conducted to examine the relationship between each core specimen quality factor and covariates, including sex, size of marrow sample, anxiety, pain, bone texture, needle bending, repetition required for the biopsy, indication for trephine biopsy, and length of evaluable marrow.

Sample size refers to the number of observations or replicates necessary to be included in a statistical study. Based on a sensitivity of 98% in predicting positive core specimen quality factor and considering numerous variables related to trephine bone marrow biopsy, a maximum marginal error, also known as the estimate's precision, of 2.08% has been chosen. The standard population proportion has been assumed to be 50%. A sample size of 300 patients has to be used to test the general hypothesis. After determining the sample size, it has been determined that 274 patients would be enrolled in the study. This sample size has been deemed appropriate to meet the research objectives and obtain reliable data. Sample sizes are crucial as they represent subsets of a population selected for a particular survey or experiment. In the present study, the sample size has been determined considering a finite population, as illustrated in equation (3.1) below [97]:

$$n' = \frac{n}{1 + \frac{z^2 \times \hat{p}(1-\hat{p})}{\varepsilon^2 N}} \tag{3.1}$$

here n represents the desired sample size from the unlimited population, ε is the margin of error, N represents the size of the population under consideration, z represents the z score values (taken from Z-score table), and $\hat{p}$ is the estimated population proportion, which is often based on preliminary data or prior knowledge.

3.2 Computational modeling

3.2.1 Geometrical modeling of conventional BMB needle

The fine biopsy needle geometric parameters investigated in the present article have been considered from the numerical and experimental models proposed by different researchers [98, 99]. In the present study, a fine conical-shaped biopsy needle has been created with different diameters, viz., 11G - 14G and 20G, to be deployed in both adults and infants. The G here represents the gauge size of the needle which specifies the lumen diameter of the needle. The higher the gauge value, the smaller the diameter of the needle, viz, a 20G needle has a finer lumen than an 11G needle. In the present investigation, a significant large circle region with a diameter of ϕ20 mm has been selected, as depicted in Figure 3.4.

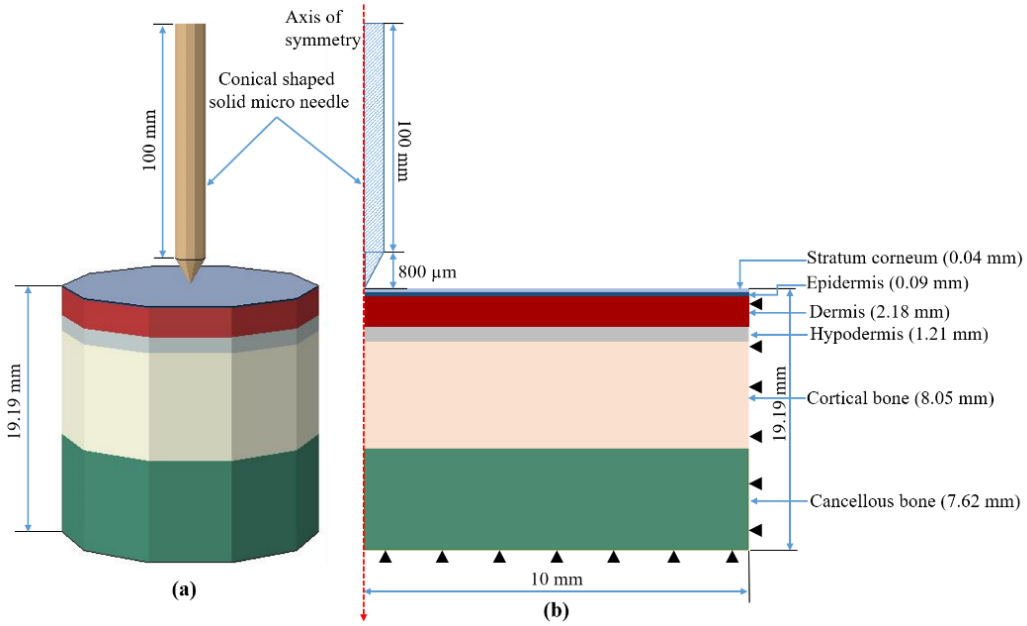

Figure 3.4: Schematic of (a) iliac crest layers with conical needle model and (b) axisymmetric view of a solid model with boundary conditions

All the fine conical-shaped stainless steel biopsy needles used for FEM simulation of insertion have a length of 100 mm. The biopsy needle has been established as a rigid body due to its high modulus [100]. The model design includes the layers of the iliac crest (viz., stratum corneum, epidermis, dermis,

hypodermis, cortical bone, and cancellous bone) on the bottom surface and stainless-steel biopsy needle with a conical tip on the upper surface. A displacement of 15.35 mm, i.e., up to the cancellous bone, has been applied to the needle (rigid part) along the insertion direction.

3.2.2 Geometrical modeling of honeybee stinger/mosquito proboscis-inspired BMB needle

The BMB is necessary to diagnose hematological malignancy and other disorders and monitor patients receiving bone marrow transplantation, chemotherapy, and other medical therapies. A needle collects bone marrow during biopsy from the posterior iliac crest, which is then prepared like other tissue samples. The BMB is a minimally invasive procedure recommended for assessing marrow cellularity, accurately counting the number of megakaryocytes, and finding specific lesions such as granulomas, lymphomas, and metastatic cancer. Several basic studies on honeybee stingers and mosquito proboscis have been conducted in Fly Lab (Indian Institute of Technology Kanpur), influenced by the peculiar mechanics of the honeybee stinger and mosquito proboscis. Honeybee stinger and mosquito proboscis pictures have been captured using a fluorescent stereo microscope (Leica M205FA) to help us to comprehend their barb designs better (refer to Figure 3.5(a)).

After considering the advantages and disadvantages of the honeybee stinger and mosquito proboscis, unique 3D barbed needle designs inspired by the honeybee stinger and mosquito proboscis have been developed using SolidWorks CAD software (refer to Figure 3.5(b-d)). The honeybee stinger has asymmetrical barbs [81]. However, it's steep α_2 enhances the removal force of the stinger by approximately 70 times compared to the acupuncture needle [95], which is produced by the unequal barb distribution along the needle shaft. Barbs that protrude from the stinger's main structure enhance the drag force during penetration. Recognizing the disadvantage of asymmetrical barbed needles, the needle has been designed with symmetric barbs on the surface of the needle shaft. The design described in the present paper attempts to minimize or remove any drawbacks, especially the large stinger extraction force, while preserving the benefit of the stinger's barbs to minimize the insertion force. The barbs in the present honeybee-inspired biopsy needles will not be the same as those on the stinger. Figure 3.5(a) depicts the 3D model of a hollow barbed and mosquito proboscis biopsy needle with a beveled tip generated using 3D CAD design SolidWorks software. The needle has an outer diameter of 3 mm [81] and an inner diameter of 1.7 mm. The overall length of the hollow barbed biopsy needle is 100 mm. In the present model, barbs have been placed on the periphery of a plain biopsy needle to study their influence on the insertion and extraction forces (refer to Figure 3.5(b)). The barbs seen in Figure 3.5(d) are 360°revolved on the circumference of the needle. To study the insertion, deflection, and extraction forces during BMB simulation α_1 (147°-170°), α_2 (90°-170°), h_b (0.2 mm-0.5 mm), L_{bs} (30 mm-45 mm), insertion velocity (2mm/sec-20mm/sec), vibration frequency (55 Hz-110 Hz), amplitude (5 µm-35 µm), 2 radian/time-6.67 radian/time have been

varied. The bioinspired BMB stainless steel needles utilized in finite element modeling exhibit mechanical properties, comprising a density of 7.85e-09 ton/mm^3, a Young's modulus of 205,000 MPa, Poisson's ratio of 0.29, and a yield stress ranging from 450 to 600 MPa. [101].

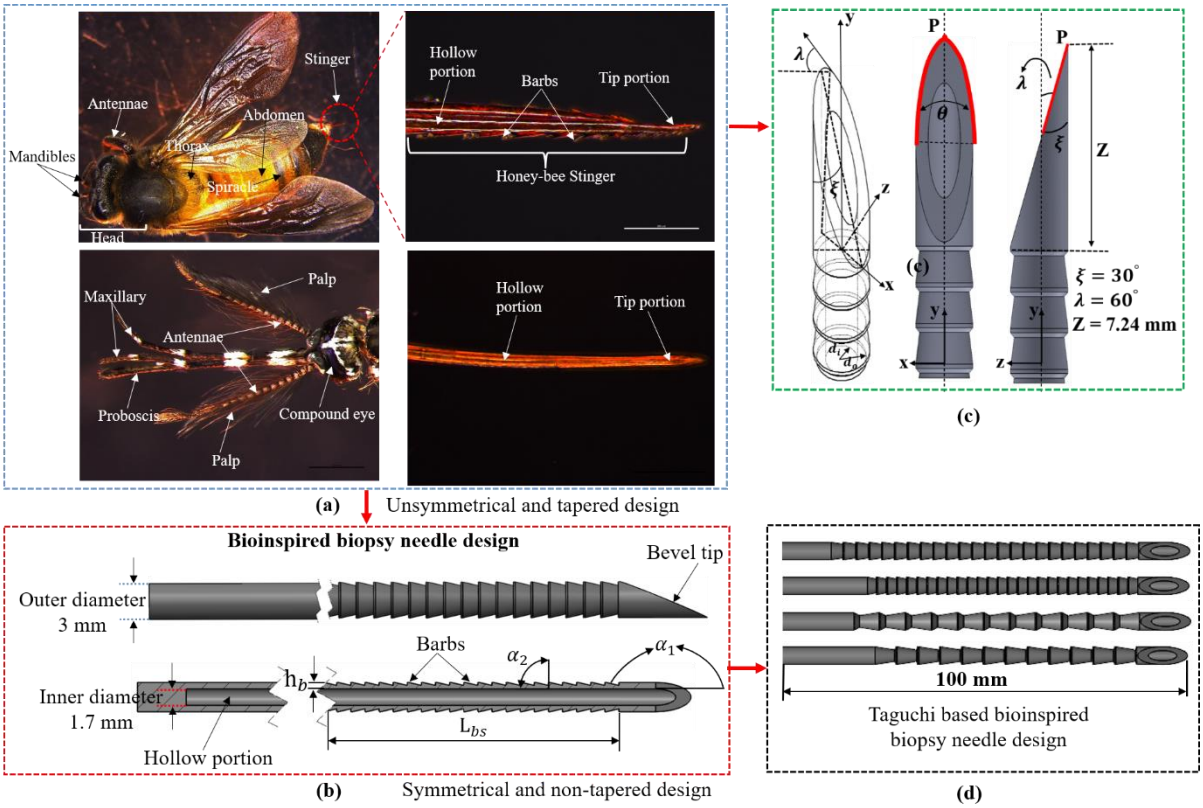

Figure 3.5: (a) Pictorial illustration of the mosquito proboscis, honeybee and its stinger, (b) cut section of the hollow needle with barb design parameters, (c) design of 3D needle encompasses included angle (θ), inclination angle (λ), and bevel angle (ξ), and (d) 3D models of the barbed biopsy needles with different barb design parameters [102].

3.2.3 Multilayered skin-bone tissue design (Iliac crest model)

Human skin is a non-linear viscoelastic and anisotropic material with complex mechanical characteristics [40]. The human iliac crest is well-structured and comprises five heterogeneous skin-bone tissue layers: the stratum corneum, epidermis, dermis, hypodermis, cortical bone, and cancellous bone, as shown in Figure 3.6(a). The barbed biopsy needle's insertion depth is proportional to the thickness of the iliac crest layers (i.e., skin and bone layer). The current numerical simulation uses a skin-bone model to better understand the insertion and extraction processes. The bottom surface of the numerical model has the iliac crest layers (stratum corneum + epidermis, dermis, hypodermis, cortical bone, and cancellous bone), while the upper surface has a stainless-steel hollow barbed biopsy needle with a bevel tip. This study has

chosen a considerably broad cuboidal domain with dimensions of 40 mm × 60 mm × 40 mm (refer to Figure 3.6(b)). An insertion depth of 53 mm, i.e., up to the center of the cancellous bone, has been considered in the present study.

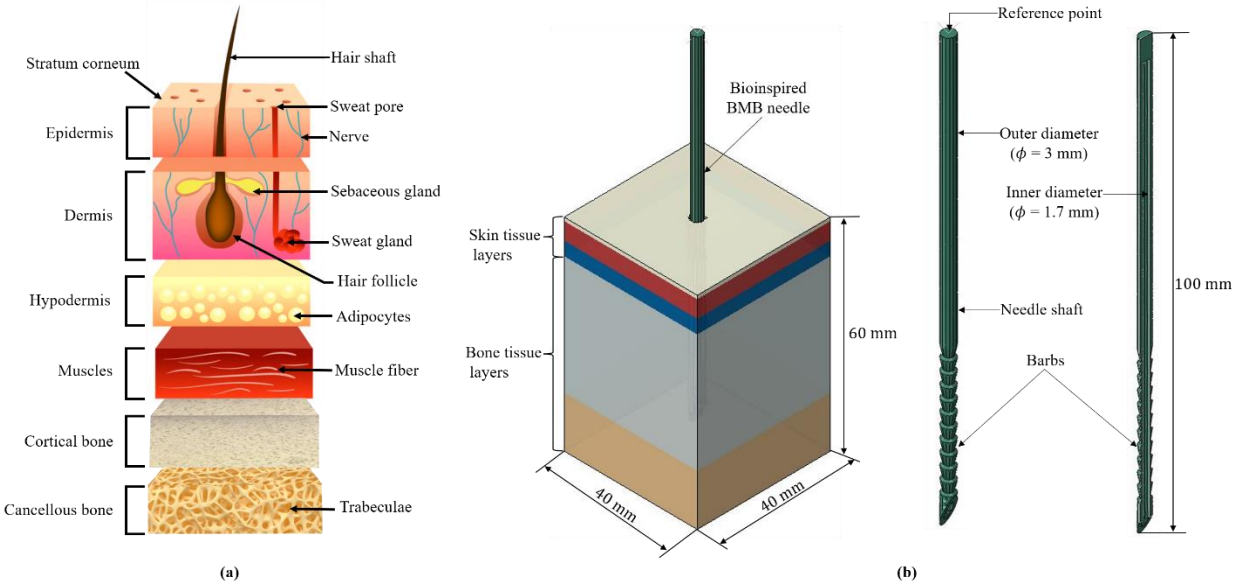

Figure 3.6: (a) Schematic of a cross-section of the human iliac crest and (b) three-dimensional heterogeneous cuboidal domain of biological iliac crest (skin-bone) tissue with an embedded bioinspired BMB needle generated using ABAQUS

3.2.4 Material properties

For simplicity and owing to the lack of significant mechanical data, all three skin layers have been modeled as hyperelastic by using the Neo-Hookean model. The present study has used uniaxial tensile data provided by [103-105] for the stratum corneum, who measured the elongation at fracture, mechanical properties, and failure stress from the stress-strain features of the human stratum corneum. The stratum corneum + epidermis hyperelastic and other material properties have been selected as the density = 1.3E-09 ton/mm^3, stiffness C_{10} = 13 MPa, D_1 =1.03E-07 and failure stresses = 13-44 MPa [103,106]. Similarly, the dermis might also be considered hyperelastic, isotropic, and incompressible, according to the results of Hendriks et al. [107]. Based on the studies of Hendriks et al. [107] and Duck [108], the dermis material properties have been selected as the density = 1.2E-09 ton/mm^3, stiffness C_{10} = 0.2 MPa, D_1 = 1.03E-07 and failure stresses = 13-44 MPa. Failure and substantial distortion do not occur in the hypodermis layer. For simplicity, Poisson's ratio of 0.48, Young's modulus of 3.4×10^4 Pa, and an elastic behavior for the hypodermis have been considered [109]. This study has considered elastoplastic behavior to imitate anisotropic cancellous and cortical bone until failure. The values of the anisotropic cortical bone's parameters, including Young's modulus of 14500 MPa, Poisson's ratio of 0.2, yield stress ranging from 90-

147 MPa, and density of 1.1E-09 ton/mm^3, as well as the parameters of the cancellous bone, including Young's modulus of 1370 MPa, Poisson's ratio of 0.2, yield stress ranging from 2.2-4.2 MPa, and density of 2.7E-10 ton/mm^3, were obtained from Demirbas et al. [110]. As a result of the elastoplastic properties of cancellous and cortical bones, the Johnson-Cook plasticity model was used by Demirbas et al. [110]. Further, using a distortion energy theory coupled with element deletion, the user subroutine 'VUSDFLD' has been used to simulate skin failure during the insertion process. An element close to the barbed biopsy needle tip will be recognized and removed from the mesh if its effective stress has reached the required failure threshold. Table 3.2 shows the appropriate material properties determined by the experimental work [103-110].

Table 3.1: Mechanical properties of the human skin-bone (iliac crest) model

Hyperelastic material [103-108]					
	Material model	Stiffness (C_{10}) (MPa)	Compressibility value (D_1)	Density (ton/mm^3)	Failure stress (MPa)
Stratum corneum and epidermis	Neo-Hookean	13	1.03E-07	1.3E-09	13-44
Dermis	Neo-Hookean	0.2	1.03E-07	1.2E-09	7.3
Linear elastic and elastoplastic material [109, 110]					
	Young's modulus (MPa)	Poisson's ratio	Yield stress (MPa)	Density (ton/mm^3)	Friction coefficient
Hypodermis	0.034	0.48	1.0-1.05	9.71E-10	0.42
Cortical bone	14500	0.323	90-147	1.1E-09	0.42
Cancellous bone	1370	0.3	2.2-4.2	2.7E-10	0.42

3.2.5 Governing equations

Bone has been modeled as an elastic-plastic material and skin layers as hyperplastic material due to the absence of fundamental mechanical properties and its simplicity at the microscopic level.

The skin has been assumed to be isotropic, and its isothermal elastic characteristics can be characterized using the strain energy function [111].

$$U = f(\bar{I}_1, \bar{I}_2, \bar{I}_3) \tag{3.2}$$

here U is the strain energy density and $\bar{I}_1, \bar{I}_2,$ and $\bar{I}_3$ are Cauchy-Green deformation tensors.

Equation (3.2) can be approximated as:

$$U = \sum_{i=1}^{3} C_{i0}(\bar{I}_1 - 3)^i + \sum_{i=1}^{3} \frac{1}{D_i}(J_{el} - 1)^{2i} \tag{3.3}$$

Here, i = 1…3 denotes the true stress, J_{el} is the elastic volume ratio, C_{i0} and D_i are material constants.

Here the strain tensor invariants are provided by:

$$(\bar{I}_1 = \lambda_1^2 + \lambda_2^2 + \lambda_3^2,\ \bar{I}_2 = \lambda_1^2\lambda_2^2 + \lambda_2^2\lambda_3^2 + \lambda_1^2\lambda_3^2,\ \bar{I}_3 = \lambda_1^2\lambda_2^2\lambda_3^2) \quad (3.4)$$

When material data is insufficient, the neo-Hookean version can be used. It is simple to use and can provide acceptable approximation at low stresses. It is produced by simplifying the reduced-polynomial strain-energy function further by setting N = 1:

$$U = C_{10}(\bar{I}_1 - 3) + \frac{1}{D_1}(J_{el} - 1)^2 \quad (3.5)$$

If the material is considered to be incompressible, then J = 1, and the second term becomes zero. Using only the first term results in the neo-Hookean model [111].

$$U = C_{10}(I_1 - 3) \quad (3.6)$$

where U represents the potential strain energy, and I_1 represents the shear behavior of the model.

The present study has considered elastoplastic behavior to simulate anisotropic cortical and cancellous bone up to failure. Numerous studies have shown that bone displays anisotropic behavior with ultimate stress, elastic modulus, and yield stress, shifting substantially according to stress directions [112-114]. The Johnson-Cook plasticity model has been applied due to the elastoplastic behaviors of cortical and cancellous bones, as shown in Table 3.3 [110]. The material behaves like linear elastic as per the Johnson-Cook plasticity model; however, the material deforms plastically once the yield stress is achieved. The damage caused by the penetration of the needle has been assessed using the ductile damage initiation criteria [110]. The stress distribution during plastic deformation can be described using the Johnson-Cook plasticity model (Equation 3.7) [115].

$$\overline{\sigma} = \left(\mathrm{A} + \mathrm{B}\left(\overline{\varepsilon}^{\mathrm{pl}}\right)^{\mathrm{n}}\right)\left[1 + \mathrm{Cln}\left(\frac{\dot{\overline{\varepsilon}}^{\mathrm{pl}}}{\dot{\overline{\varepsilon}}_{\mathrm{o}}^{\mathrm{pl}}}\right)\right]\left(1 - \left(\frac{\mathrm{T} - \mathrm{T}_{\mathrm{room}}}{\mathrm{T}_{\mathrm{melt}} - \mathrm{T}_{\mathrm{room}}}\right)^{\mathrm{m}}\right) \quad (3.7)$$

where A, n, B, C, and m are material constants, $\overline{\varepsilon}^{\mathrm{pl}}$ is the equivalent plastic strain, $\dot{\overline{\varepsilon}}^{\mathrm{pl}}$ represents the equivalent plastic strain rate and $\dot{\overline{\varepsilon}}_{\mathrm{o}}^{\mathrm{pl}}$ is the reference plastic strain rate, respectively. Further, $\mathrm{T}_{\mathrm{melt}}$ and $\mathrm{T}_{\mathrm{room}}$ represent the melting and room temperatures, respectively.

The equivalent plastic strain ($\overline{\varepsilon}^{\mathrm{pl}}\mathrm{D}$) at the beginning of the damage is determined by the strain rate and the stress triaxiality under the ductile damage initiation criteria:

$$\overline{\varepsilon}^{\mathrm{pl}}\mathrm{D}\left(\eta, \dot{\overline{\varepsilon}}^{\mathrm{pl}}\right)$$

where η = p/q denotes the stress triaxiality, q represents the Von Mises equivalent stress, and p is the pressure stress.

It has been presumed that damage occurs when the damage parameter (B_D) exceeds 1 in the Johnson-Cook dynamic damage model, depending on the corresponding plastic strain value at element integration sites.

$$B_D = \sum \left(\frac{\Delta \bar{\varepsilon}^{pl}}{\bar{\varepsilon}^{pl} D\left(\eta, \dot{\bar{\varepsilon}}^{pl}\right)} \right) \tag{3.8}$$

where, $\Delta \bar{\varepsilon}^{pl}$ represents a growth in the equivalent plastic strain. Cancellous bone has fracture strain, stress triaxiality, and strain rate values of 0.0002, 0.5, and 1, respectively, whereas cortical bone has fracture strain, stress triaxiality, and strain rate values of 0.0001, 0.5, and 1, respectively [110].

Table 3.2: Johnson Cook plasticity parameters and material constants for bone tissue [110]

Parameter	**Cancellous bone**	**Cortical bone**
Yield stress (A), (MPa)	28	90
Hardening modulus (B), (MPa)	0.1	0.1
Hardening exponent (n)	0.1	0.1
Thermal softening coefficient (m)	0.02	0.02
Strain rate coefficient (C)	0.015	0.03
Reference strain rate $\left(\dot{\bar{\varepsilon}}_o^{pl}\right)$	0.001	0.001
T_{melt} (K)	1573	1573
T_{room} (K)	293	293

3.3 Numerical modeling

The barbed biopsy needle insertion and removal mechanisms from the human iliac crest are still not well understood. Hence, a non-linear FEM model has been suggested to simulate and visualize the barbed biopsy needle insertion and extraction process into the human skin-bone tissue. In the present study, a Lagrangian-based FE numerical simulation model has been developed using the ABAQUS® package, as depicted in Figure 3.7(a). All mesh elements have been created using a free mesh generator incorporated into ABAQUS, which offers several meshing choices based on the number of mesh elements, ranging from relatively coarse (containing few elements) to very fine mesh (containing a large number of elements). A grid independence test has been conducted to determine the ideal mesh element size while reducing computing expenses. The outcome of a grid independence study for several meshing configurations of ABAQUS's integrated mesh generator for a heterogeneously dense iliac crest model has been shown in Figure 3.7(b). No major difference in the stress value has been recorded for the element size after 0.3 mm. Hence, as mentioned above, the results concluded that the outcome is convergent, and any additional decrease in mesh size does not significantly enhance the result. As a result, the most suitable element size of 0.3 mm has been selected throughout the simulation to perform the investigation. A very fine mesh has

been generated between the needle and iliac crest layers zone to achieve highly precise numerical results in higher stress and strain gradient regions. The skin-bone domain has meshed with eight nodes of fine C3D8R mesh elements and a lower integration. A fine mesh with an element size of 0.3 mm has been constructed to get more accurate numerical output while minimizing computational effort. The region away from the BMB needle has been meshed with a standard element size of 1.6 mm.

The skin-bone tissue has been meshed using a total of 4,80,800 elements. The barbed biopsy needle has been meshed with 16,207 4-node linear tetrahedron C3D4 mesh element. The current investigation has employed a 2^{nd} order (modified quadratic tetrahedron) tetrahedral element type. The tetrahedral elements of the second order are more precise and give a better geometric depiction. They can capture precise geometric detail and deform more realistically than the linear components. Meshing is easier and faster for the software when tetrahedral components are used. ABAQUS meshes cannot always generate hexahedral elements for every conceivable form and may loop indefinitely or fail with an error message. The tetrahedral elements will be more precise than the existing best estimates of elasticity, Poisson's ratio, thermal conductivity, or dimensional tolerances. No contemporary solution is more exact than any physical qualities and dimensions that may be entered into the tetrahedral element model. As a result, hex components are overkilled in many applications. When hyper elastic materials come into contact with a solid or another hyper elastic body, the hex components will give a quicker solver time and may even ensure convergence. As a result, in the current investigation, hexahedral components have been employed in the skin-bone domain and tetrahedral elements in the needle domain. The numerical convergence has been observed below the solver's pre-specified relative tolerance of 0.0001. The segregation method that divides the solution procedure into smaller steps enhanced the convergence of the FEM solution. Surface-to-surface contact between the skin-bone domain and a barbed biopsy needle has been modeled in ABAQUS®/Explicit. In the simulation, the friction coefficient values for skin and bone tissue have been selected to vary from 0.10 to 0.42 and 0.30 to 1.03, respectively. These values have specified the contact conditions between the needle and the skin-bone model [116].

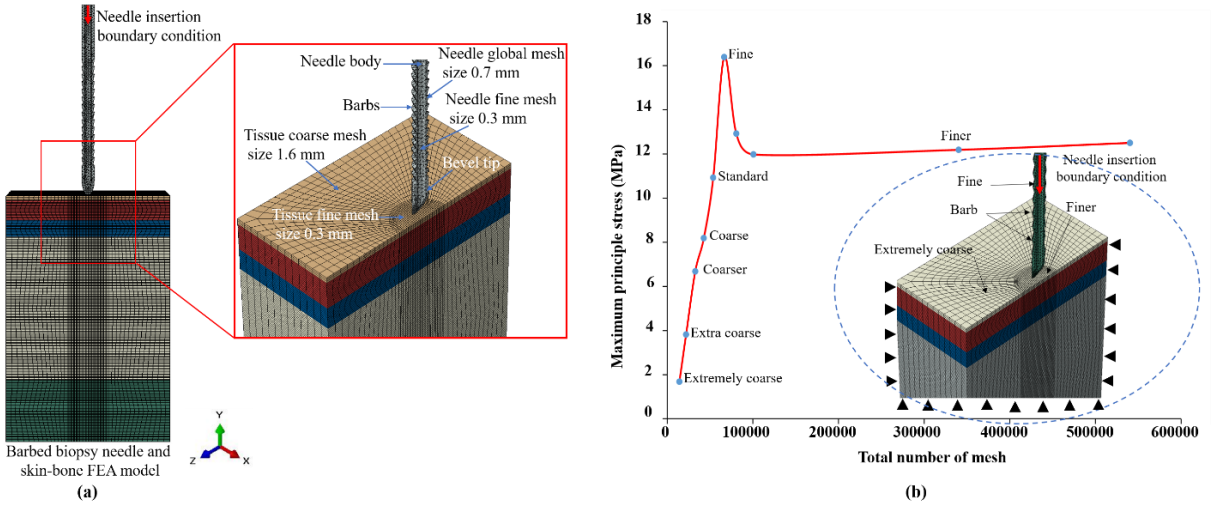

Figure 3.7: Finite element analysis: (a) design environment with different meshes and (b) Grid independence test outcomes of iliac crest model during BMB procedure analysis

The barbed biopsy needle penetrates the skin-bone tissue domain, with velocities in the range of 2-20 mm/sec, to acquire the tissue samples. The insertion speed influences the dimension of the biopsy needle and the type of tissue sample to be obtained during a biopsy operation. For softer tissues, such as liver or breast tissue, a slower insertion speed is suggested to avoid tissue injury and bleeding. On the other hand, faster insertion speeds may also be employed for harder tissue, like bone tissue, to allow for efficient tissue penetration. Moreover, the speed should be fast enough to accomplish the procedure on time but slow enough to reduce patient discomfort and pain. As a result, the present study considered different insertion speeds (slow and fast values). In the present study, different skin and bone layers have been represented by discrete partitions in the cuboidal-shaped skin-bone model. Mesh element deletion is the most commonly available procedure to model the separation due to fracture and material failure in FEM. This procedure will remove some elements as the required element removal condition is met during deformation.

Moreover, if small suitable elements are employed during the simulation, the influence of mesh size dependence can be minimized. In the present study, FE analysis of the fine needle insertion procedure in the iliac crest layers has also been performed by employing ABAQUS®/Explicit, linked to the element deletion algorithm. For the separation and simulation of material failure, it is well recognized that element deletion must be constrained by local mesh failure criteria, like critical stress and strain. During the insertion procedure, a specific damage evolution model, "type=DISPLACEMENT," has been used to regulate the mesh element deletion in the iliac crest layers. When the stress value in the element close to the needle tip reaches the defined criteria, the element will be detected and then deleted from the mesh. The elements of the needle permitted rotation on the x and y-axes as well as translation on the y-axis using a reference node. The bottom nodes of the iliac crest domain have been fully confined using the encastre boundary condition (refer to Fig. 3.7(b)). In the current study, enhanced hourglass control and element distortion have also been

applied to regulate the element distortions. All simulations have been run on a Dell Precision Tower 7810 workstation equipped with eight Core 3.1 GHz Xeon processors and 64 GB RAM.

3.4 Parametric optimization approach

In the current study, a parametric optimization has been conducted. The optimization focused on six key parameters: α_1, α_2, h_b, L_{bs}, needle rotation, and insertion velocity. The examination aimed to identify the optimal values for these parameters. Additionally, five parameters with four levels and one with two levels has been considered based on the modifications of each input variable described in the literature (refer to Tables 3.4). To adequately evaluate the impact of every chosen input variable on the response variable, a full factorial analysis approach used for six parameters with several levels each will have $4^5 \times 2^1 = 2048$ FE simulation permutations. As a result, using all possible combinations becomes cumbersome and expensive, necessitating additional time and resources to complete the study. Taguchi method-based orthogonal array has been utilized to minimize the number of tests, resulting in identical results with the same system performance [117]. The current study considers Taguchi's L32 orthogonal array, which requires 32 tests instead of 2048 for the full factorial design approach. Each computational procedure has been carried out step by step using ABAQUS FEM software to evaluate the tissue deformation, needle bending, insertion, and extraction forces up to a depth of 53 mm.

Table 3.3: Selected parameters and their associated levels utilized in the study

Parameter level	**α_1 (degree)**	**α_2 (degree)**	**h_b (mm)**	**L_{bs} (mm)**	**Insertion velocity (mm/sec)**	**Needle rotation (degree)**
Level 1	147	90	0.2	30	3	180°
Level 2	157	110	0.3	35	5	360°
Level 3	167	130	0.4	40	7	
Level 4	170	170	0.5	45	10	

3.5 Architecture development of the ANN model

As a machine learning methodology, ANN has uncovered intricate and non-linear connections amidst diverse datasets. ANN models perform better than regression-based models in handling datasets containing substantial noise levels. ANN effectively handles input data variability and exhibits a remarkable ability to identify data patterns, resulting in highly accurate output predictions compared to traditional techniques. The Python 3, google colab, and library-keras has been utilized to create the architecture for the ANN model. Figure 3.8 displays the schematic diagram depicting the architecture of the ANN model. The

components comprising the architecture of the ANN model include input parameters, viz., an input layer, a hidden layer, and an output layer (refer to Figure 3.8). After the training and testing, the model becomes prepared to predict the output results (viz., insertion, extraction, and deflection) corresponding to the provided inputs. In the present study, the hidden layer of the neural network consisted of 8 neurons. Each neuron in the network functions as a separate computational unit. The neurons in the input layer gather data from the input variables and transmit it to the neurons in the hidden layer, where it gets analyzed by assigning appropriate weights to various input data. Once the accumulated data within a particular neuron surpasses a threshold limit, it is propagated to the output layer and extracted as the predicted value for the corresponding output variable.

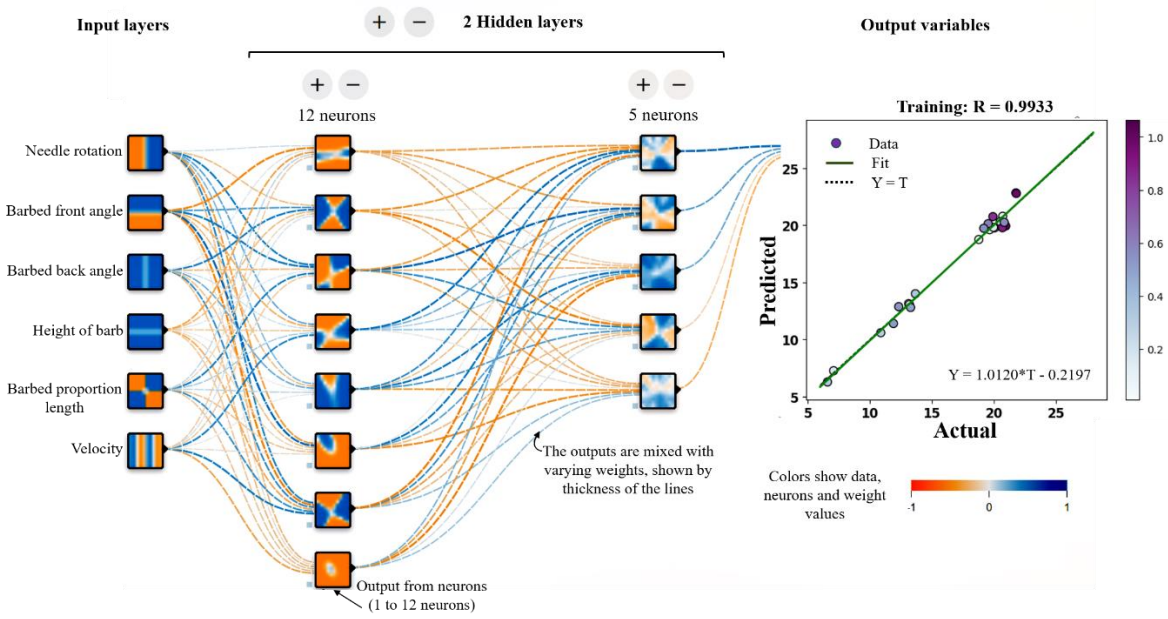

Figure 3.8: Architecture model of artificial neural network

3.5.1. Training and testing of the ANN model

After establishing the architecture, the ANN gets trained by utilizing an array of known inputs and corresponding outputs. In this study, 32 simulations have been conducted using Taguchi's L32 orthogonal array, resulting in 32 data sets. Among them, 60% have been assigned for training the ANN model, 20% for testing, and 20% for validation. The computed input and output values have been imported into the ANN model for additional processing during the training phase. Using the input and output data, the model establishes the correlation between them and assigns varying weights to neurons, enabling it to calculate predicted outputs based on these weightings. The model computes its predicted outputs using the specified weightage and then compares them to the actual outputs. The disparity between the predicted and actual outputs is evaluated to estimate the error. This procedure has been performed iteratively, and the model weights have been adjusted to minimize the difference between the expected and actual outputs. The

'Levenberg-Marquardt' approach has been implemented as an error function in the model to minimize the difference between the predicted and actual outputs. This approach entails altering the weights of neurons in the network. The iterative process of adjusting the weights in accordance with error feedback is known as 'backpropagation,' and it persists until the model reaches a global minimum error. The performance of the model is assessed by evaluating the mean squared error value, which indicates how closely the regression line aligns with a given set of data. The rationale for selecting MSE is its ability to effectively identify outlier predictions with substantial errors by assigning greater importance to them through the function's squaring operation.

Chapter 4

Results and Discussions

This chapter offers a concise yet comprehensive set of findings illustrating the importance and contextual foundation of the queries under consideration. Moreover, this chapter examines the aims of tackling these issues and offers a thorough overview of its contents, providing a comprehensive outlook on the subject matter. In this chapter, the outcomes pertaining to the investigations conducted in this thesis are presented. These studies adhere to the sequence outlined in section 1.2 (chapter 1) and the methodology in chapter 3.

4.1 Trephine Biopsy of Bone and Bone Marrow Procedure Survey (Study 1)

The primary goal of this study is to survey Indian patients undergoing the trephine bone marrow biopsy process to identify real-time challenges experienced by both clinicians and patients during the procedure. The present study acquired data related to 274 trephine biopsy samples from 300 patients at the Post Graduate Institute of Medical Education & Research (PGIMER), Chandigarh, India.

4.1.1 Trephine BMB complications and information quality

Eight incidences of bleeding and dizziness complications were reported during these 2 months of 274 trephine BMB procedures. The most common issues linked with BMB were needle bending, the length of the bone marrow sample, and the number of repetitions needed during the biopsy. The complications associated with trephine BMBs, such as pain, bleeding, dizziness, etc., have been shown in Table 4.1. In the current study, all patients were anxious before and during the procedure, and they experienced no/less pain, moderate pain, and intolerable pain during the trephine biopsy procedure (refer to Figure 4.1). Out of 274 cases, 34 BMB (12.4%) cases have been evaluated as non-anxious, 92 (33.57%) cases as anxious and 148 (54%) BMB cases as very/highly anxious as evaluated by the author and the hematologist. It was also observed that the quality of the information provided during the biopsy process could help reduce anxiety to a certain level. The information quality provided before and after the procedure was overall good. In 232 inspections out of 274 BMB cases, the patients were satisfied with the information provided before, during, and after the procedure; 133 (57.3%) of them became non-anxious, 75 (32.3%) remained anxious, and 24 (10.3%) were highly anxious. In contrast, 42 (15.3%) patients were not satisfied with the information provided before, during, and after the process; of these patients, 4 (9.52%) were non-anxious, 8 (19%) of them were anxious, and 30 (71.4%) were highly anxious ($p = 0.15$). Of the 274 patients who underwent the

trephine BMB procedure, only one refused to undergo the BMB procedure due to high anxiety. Providing adequate information regarding the biopsy process might avoid anxiety, and there is no doubt that the trephine biopsy specialist should keep the procedure as brief as possible. Additional complications were revealed as an effect of premedication. Forty-five (16.4%) patients were given premedication before the biopsy procedure, mainly with the appropriate dosage of Prilox Lignocaine cream and Toplap Lidocaine cream. Five (11.1%) experienced the side effects (viz., rashes and reddishness), but no one was critical enough requiring extensive hospitalization. Premedication before the procedure helps reduce the pain to some extent but does not help avoid intolerable pain.

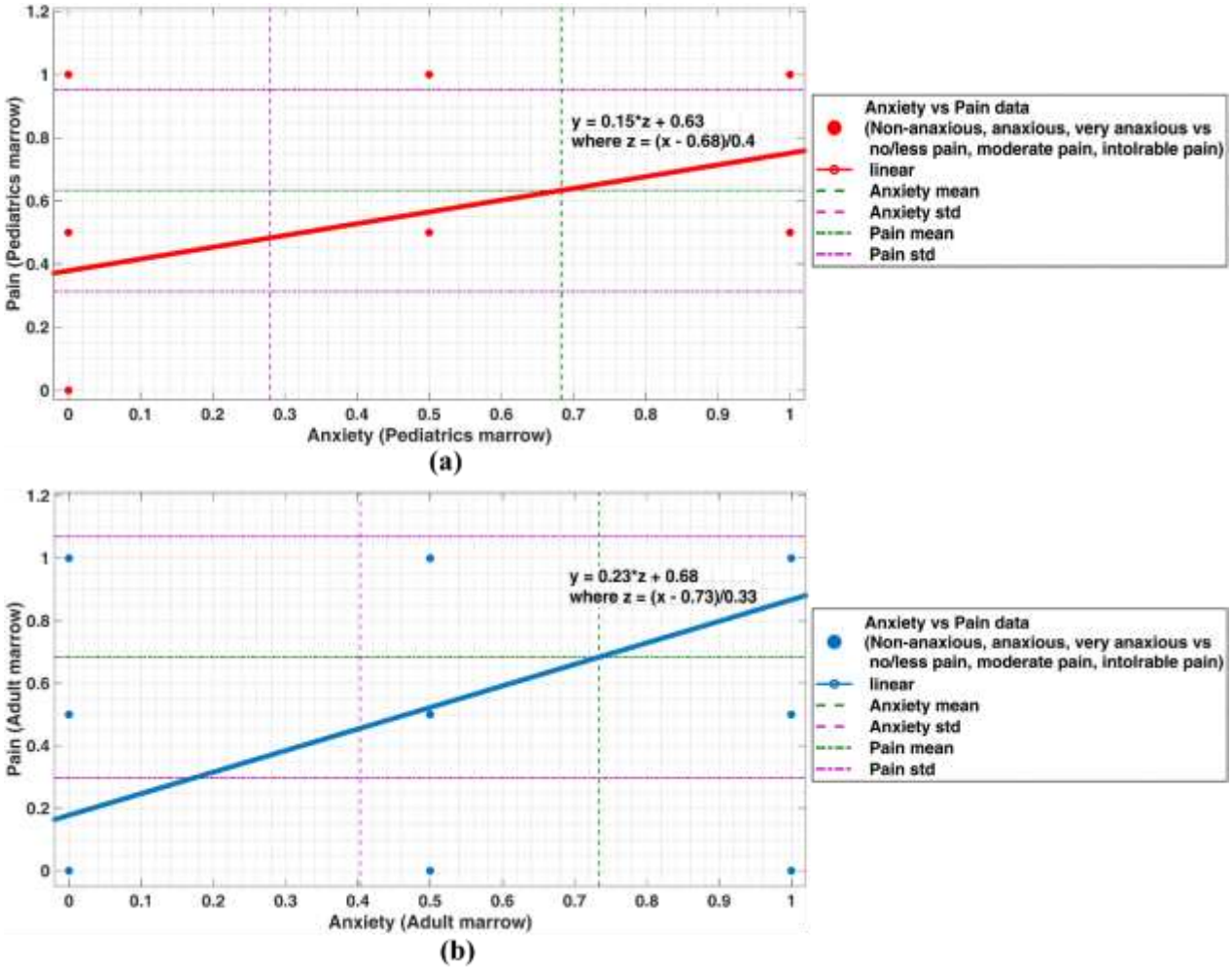

Figure 4.1: (a) Pediatrics anxiety vs. pain level and (b) adult anxiety vs. pain level evaluated during the trephine biopsy

Table 4.1: Table showing complications associated with trephine BMB inspections

			Number of patients	Percentage
Trephine biopsy-related complications	**Anxiety**	Non-anxious	34	12.4
		Anxious	92	33.57
		Very/highly anxious	148	54
	Pain	No/less pain	41	14.96
		Moderate pain	82	29.92
		Intolerable pain	151	55.1
	Number of attempts	One	27	9.85
		Two	54	19.70
		Three	12	4.37
		Four	20	7.29
	Infection	Yes	0	0
		No	274	100
	Bleeding	Yes	3	1.09
		No	271	98.9
	Dizziness	Yes	5	1.82
		No	269	98.1
Premedication-related complications		No	269	98.1
		Rashes	2	4.5
		Reddishness	2	4.5
		Fatigue	1	2.2

4.1.2 Aspects related to pain

Various issues were covered in the questionnaire surveyed by patients and operators, while some aspects of pain have been considered when the procedure was completed. The author and the hematologist evaluated the patients as experiencing no/less pain for 41 BMB (14.96%) procedures, moderate pain for 82 (29.92%) procedures, and intolerable pain for 151 (55.1%) BMB procedures (refer to Table 4.1). Out of 274 patients, 251 (91.6%) underwent the biopsy procedure for the first time, while the remaining 23 (8.4%) already had previous experience with bone marrow biopsy procedures. From the 251 patients who had their first bone marrow biopsy, 25 (9.9%) were anxious, 86 (34.3%) were non-anxious, and 140 (55.7%) were highly anxious. On the other hand, out of the 23 patients who already had a previous experience, 9 (39.1%) were anxious, 6 (26%) were non-anxious, and 8 (34.7%) were highly anxious, respectively. Thus, the

proportion of patients experiencing high anxiety has been less in those who already had an earlier experience with a trephine biopsy procedure. Anxiety has been a significant predictor of pain during the procedure, and it has been verified that the patient's psychological condition could affect the existence of pain, as detailed in Figure 4.1. It has been reported that most of the previous bad experiences of trephine BMB procedures might cause anxiety and fear for future BMBs and have been linked to intolerable pain [118]. Age does not affect unbearable pain. Fifty-two percent of 213 patients under 60 years of age complained about severe pain. Of the 54 cases over 60 years of age, 51.9% reported intolerable pain during the trephine BMB procedure ($p = 0.22$). Similarly, in patients under 13 years of age (i.e., pediatric patients), 10% of these 30 patients reported less pain, 53.3% reported moderate pain, and 36.6% reported intolerable pain with sedatives ($p = 0.43$). Ninety-eight (35.7%) trephine BMB inspections have been performed by hematologists having more than 250 BMBs of experience. One seventy-six (64.2%) cases had tolerable pain inspected by a clinician with less than 50 BMB inspection experience ($p = 0.56$). The clinician's experience did not affect the patient's anxiety and pain level.

4.1.3 Bone marrow length and requirement of repeated attempts

From 185 (67.5%) inspections, the trephine BMB has been successfully achieved with a single attempt, and a maximum of 4 attempts has been required to achieve the appropriate sample. The number of patients having intolerable pain was 34.6% for 185 cases with one attempt for trephine biopsy compared to the highest number of 72.2% for 113 cases with repeated BMB attempts ($p = 0.68$). To evaluate the trephine BMB sample quality, we initially compared bone marrow length in trephine biopsy samples. The triple-bevel needle has been related to a smaller length of evaluable bone marrow with a mean variation of 0.13 cm. Moreover, the number of patients having 1.5 cm or more marrow length has been significantly less for the case of triple-bevel crown tip (3%; 95% CI, 1% - 5%) needle as compared to single bevel needle (69.3%; 95% CI, 62.2%-78.8%). The collected information demonstrated that triple-bevel crown tip needles cause less pain than single-bevel needles but have been associated with poorer quality BMB samples. However, the number of patients who underwent biopsy using triple bevel crown tip needles has been very small ($n = 10$). The number of repetitions and size of bone marrow have also been affected by the bone texture of the patients. In the present examination, it has been noticed that the hard (hard bone represents normal bone texture) or very hard bone texture might be related to intolerable pain. Under these conditions, the BMB takes longer to complete, and the bending of the needle has been more frequent, as shown in Figure 4.2(a)-(c).

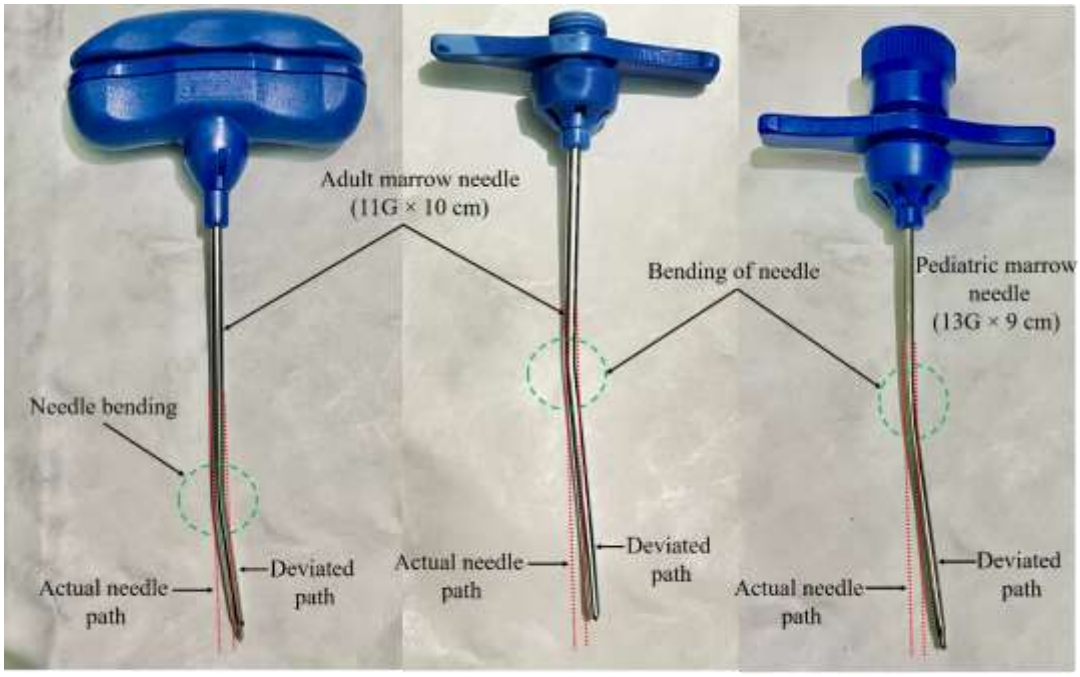

Figure 4.2: Pictorial representation of different needle types (a) triple bevel needle (adult marrow), (b) single bevel needle (adult marrow), and (c) single bevel needle (pediatric marrow) bending during the biopsy procedure

Similarly, with fragile bone texture, the bone was very soft, and locating the needle on the iliac crest surface was challenging. Due to the bone's fragile nature, the bone marrow biopsy length was much shorter than that of the hard bone. Needle bending and the number of repetitions required were significantly affected by the patient's bone texture. Figure 4.3 depicts how bone texture affects needle bending and the number of repetitions required during the BMB procedure. Of 274 cases, bone texture for 60.5% of cases was evaluated as hard, 22.3% as fragile, and 16% as very hard (clinical evaluation). Needle bending was recorded in 79 (28.8%) cases out of 274 cases, as shown in Figure 4.3. In the 'very hard' bone group, needle bending was noted in 86.3% (38 out of 44 cases), while in the hard and fragile group, it was noted in 21.7% (36/166) and 7.8% (5/64) cases, respectively. This indicates that needles bent much more frequently when the bone was assessed as very hard. Needle anchoring is complex and results in frequent needle bending due to the very hard nature of bone. Similarly, during the BMB procedure, 113 cases had to undergo repetitions because of insufficient bone marrow sample acquisition (refer to Figure 4.3). This was much more frequent in fragile and very hard bones [48/64 (75%) and 40/44 (90.9%), respectively] compared to hard (normal texture) bones [25/166 (15.1%)]. In the case of fragile bone, the crest boundary layers are soft and often break, making it difficult for the hematologist to anchor the trephine needle in the bone and increase the repetition rate.

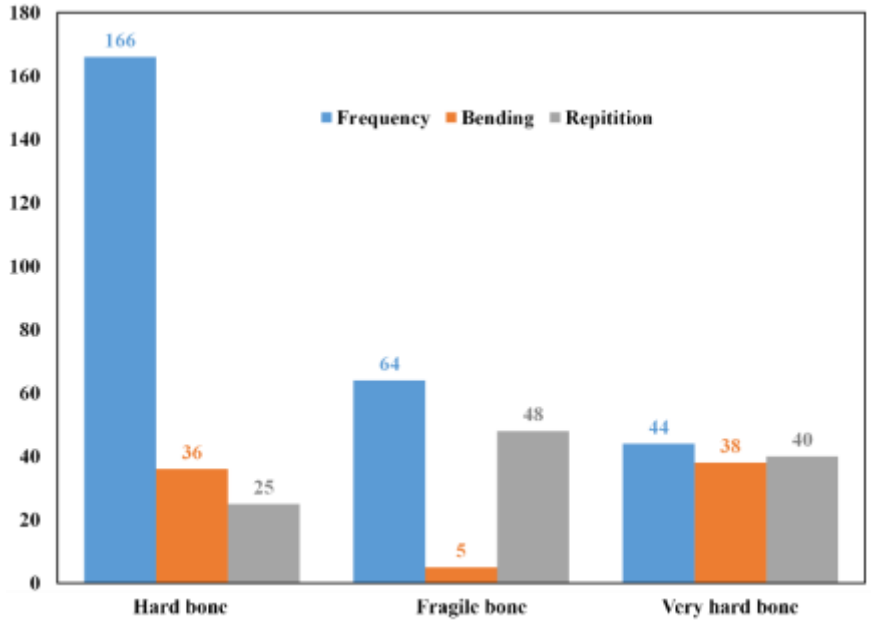

Figure 4.3: Effect of bone texture on the needle bending and number of repetitions required

4.1.4 Indication-based BMB marrow length

In the present inspection, we also consider various target lengths of bone marrow based on the indication for BMBs. Regarding bone marrow length, depending on indication: 18 BMBs (6.65%) were performed to diagnose suspected myeloproliferative neoplasm with an average evaluable bone marrow length of 2.5 cm. Twenty-four (8.75%) suspected lymphoma, 39 (14.23%) suspected multiple myeloma, and 23 (8.39%) pancytopenia trephine BMB cases were explored with an average bone marrow length of 2.1 cm, 1.6 cm, and 1.9 cm, respectively. Similarly, 23 (8.39%) out of 274 cases with suspected acute leukemia had an average bone marrow length of 1.8 cm, 29 (10.58%) suspected chronic myeloid leukemia, and 39 (14.23%) suspected acute myeloid leukemia had an average bone marrow length of 1.9 cm each. More fragmented BMB samples were reported compared to acute and chronic myeloid leukemia in the case of suspected acute myeloid leukemia. The complete evaluable bone marrow length compared with the BMB indication is shown in Table 4.2. It can be seen from Table 4.2 that the minimum length of the biopsy sample acquired during the procedure is less than 1.5 cm (1.5 cm gold standard suggested by WHO) for all the biopsy indications. Therefore, an optimum needle design or an external arrangement is required to ensure a minimum biopsy length of 1.5 cm or more. We have encountered 10 (3.64%) bicytopenia and 17 (6.2%) myelodysplastic syndrome indications with an average bone marrow length of 1.8 cm and 2.3 cm.

Table 4.2: Correlation between indications for trephine biopsy and bone marrow length.

Trephine biopsy indications	No. of cases	Percentage (%)	Minimum bone marrow length (cm)	Maximum bone marrow length (cm)	Mean length (cm)	Standard deviation
Myeloproliferative neoplasm	48	17.52	0.5	4	2.12	0.76
Lymphoma	24	8.75	0.6	3.5	2.1	0.77
Multiple myeloma	39	14.23	0.3	3.8	1.59	0.82
Acute leukemia	63	22.99	0.5	3.5	1.72	0.77
Pyrexia of the unknown region	10	3.64	0.5	2.3	1.47	0.67
Cytopenias user evaluation	31	11.31	0.3	4	1.88	0.79
Myelodysplastic syndrome	17	6.20	0.8	4	2.28	0.76
Aplastic anemia	14	5.10	0.2	3.2	1.74	0.89
Other indications	28	10.21	0.2	2.9	1.77	0.69

4.1.5 Interpretation-based BMB marrow length

The study of bone marrow contains quantitative and qualitative data about marrow cells, as well as morphologic characteristics about every cell line. The consistency of the sample is an essential aspect of interpreting bone marrow samples. Analyzing BMB length in relation to the hematological diagnosis provides valuable insights for diagnostic accuracy and disease categorization. A variety of cellular components in the bone marrow are changed in various hematological diseases. By examining the length of the BMB, clinicians can ensure an adequate representation of the bone marrow microenvironment, enhancing diagnostic accuracy by capturing the characteristic features of each disorder. Furthermore, the length of the BMB can aid in disease categorization and subtyping by determining the scope and severity of the condition. The length of bone marrow based on trephine biopsy interpretation is provided in Table 4.3. Following the interpretation, acute leukemia was reported to be the most prevalent cancer amongst those who underwent bone marrow examination in our study, with 73 (26.64%) cases diagnosed. According to the interpretation of results, acute leukemia has a minimum and maximum marrow lengths of 0.2 cm and 4.3 cm, respectively, with a standard deviation of 0.78.

The myeloproliferative neoplasm was the second most prevalent interpretation in the current study, accounting for 39 cases (14.23%), with an average marrow length of 2.20 cm and a standard deviation of

0.75 Aplastic anemia was another diagnosis presented as an interpretation in the report following examining samples in the current study. Of the 274 cases, 16 (5.83%) were identified as aplastic anemia, with a minimum and maximum marrow length of 0.3 cm and 3.1 cm, respectively, and a standard deviation of 0.81. Other cancers diagnosed during this survey were multiple myeloma (8.39%), lymphoma (8.39%), and myelodysplastic syndrome (2.55%). We found 8.39% of multiple myeloma and lymphoma cases, with average bone marrow lengths of 1.80 cm and 2.0 cm, respectively. Myelodysplastic syndrome was diagnosed in only 7 (2.55%) of 274 cases. The minimum and maximum bone marrow length for myelodysplastic syndrome ranges from 1 cm to 2.6 cm with a standard deviation of 0.63, as shown in Table 4.3.

Table 4.3: Table presenting interpretation-based BMB marrow length for different cases

Trephine biopsy interpretation	No. of cases	Percentage (%)	Minimum bone marrow length (cm)	Maximum bone marrow length (cm)	Average length (cm)	Standard deviation
Myeloproliferative neoplasm	39	14.23	0.3	4	2.20	1.0
Lymphoma	23	8.39	0.5	3	1.80	0.76
Multiple myeloma	23	8.39	0.2	3.2	2.0	0.72
Acute leukemia	73	26.64	0.2	4.3	1.93	0.78
Myelodysplastic syndrome	7	2.55	1	2.6	1.51	0.63
Aplastic anemia	16	5.83	0.5	3.1	1.84	0.81
Other interpretation	93	33.94	0.4	4	1.86	0.83

4.1.6 Surface roughness

The inner needle surface roughness has been measured using a Bruker Multimode Atomic Force Microscope with a vertical resolution of 1-5 nm after sectioning the needle to expose the internal surface. Figure 4.4 depicts microscopic images of the internal surface of an adult marrow biopsy needle (both single and triple-bevel needle) and a pediatric marrow needle. However, the BMB needles cannot be drawn using a mandrel, so their internal surface might be rough. In the present analysis, we found that the usual surface roughness (Ra) for the inner surface of commercial needles was between 1.3 µm to 3.4 µm. Figures 4.4(a) to 4.4(d) depict the inner surface roughness of Care Fusion single-bevel, Ayka single-bevel, triple-bevel crown tip, and pediatric BMB needle with 0.79 µm, 0.70 µm, 1.96 µm, and 0.64 µm respectively. As tissue moves beside the wall during operations, its rough internal surface might provide considerable frictional force to the needles. Because of this reliance on tissue length, existing trephine BMB needles are

unsatisfactory since their surface roughness restricts the quantity of tissue that can be collected. The bone marrow sample inside the needle was crushed considerably because of the high surface roughness and inner friction force. As the biopsy core within the roughened needle was crushed more, the protrusion length was more significant, and the contact length was shorter. The needle's inner frictional force influences the length of the biopsy. The biopsy length increases as the inner friction force decrease. Lowering the inner friction force may reduce the resistance to the biopsy core moving within the needle and lengthen the biopsy. The findings collected from the examination reveal that the triple-bevel crown tip had the shortest biopsy length because it had higher inner surface roughness and friction force as compared to other needles.

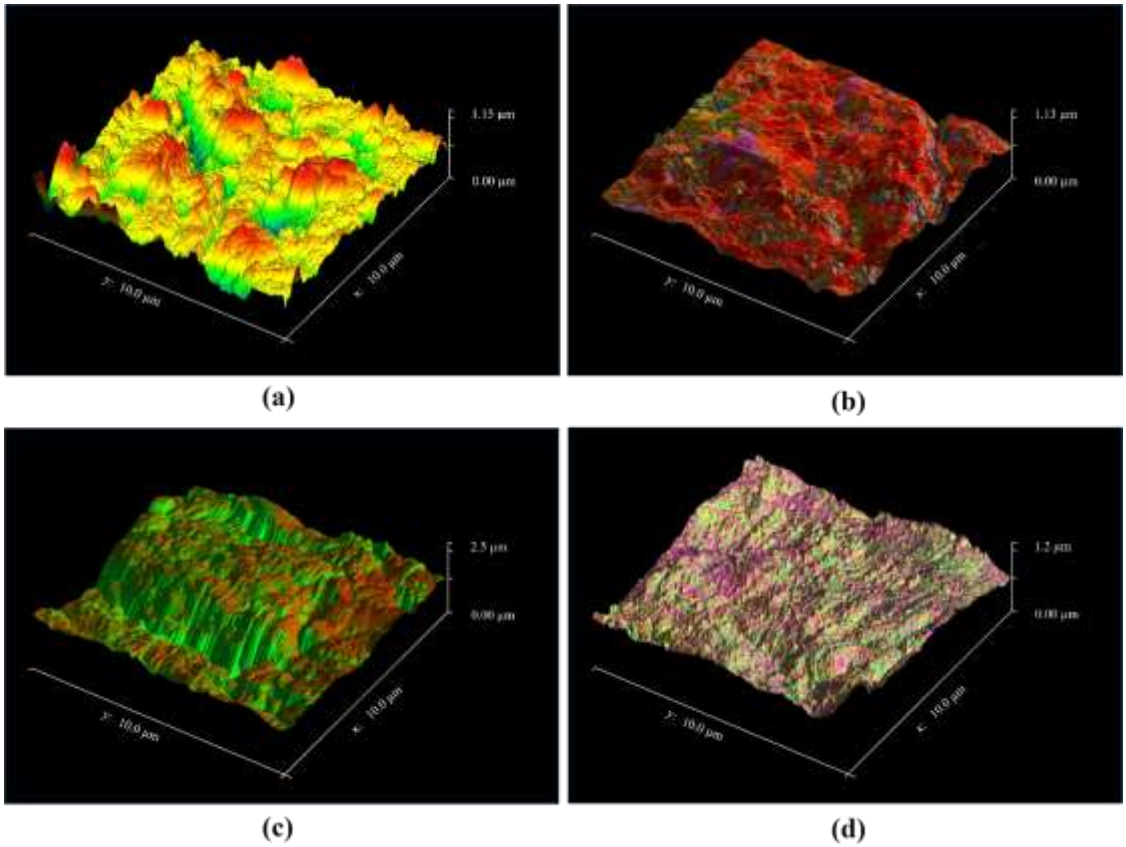

Figure 4.4: Different needle interior surfaces with typical surface topography: (a) Care Fusion single-bevel, (b) Ayka single-bevel, (c) triple-bevel crown tip, and (d) pediatric BMB needle.

4.1.7 Discussion

The present study conducted at PGIMER, Chandigarh, is a survey evaluating the pain during the BMB procedure, needle bending, number of attempts, bone texture, etc. The examination assured the safety of the process without any complications related to trephine BMB procedure except pain. Some other complications associated with trephine BMB, such as prolonged pain, infection, fatigue, and nausea, have been rare and unreported. The only complications reported have been bleeding and dizziness in some cases.

Trephine biopsies are essential for diagnosing, prognosticating, and follow-up of various hematological and non-hematological disorders. Various biopsy needles are employed in diagnostic procedures [118, 119]. In this study, a prospective survey has been executed evaluating the quality metrics of 274 BMB samples with two different Care Fusion and one Ayka needle design. These needles differed in the number of cutting edges, stylet shape, several bevels, and the shape of the handle and cradle receiving the marrow. Intolerable pain was reported by 55.1% of the patients during the trephine BMB, higher than the literature data in previous surveys, i.e., 3.7 % and 15.9% of patients complained of unbearable pain [118]. This variation in data may be due to the design of the inspection, the various factors for intolerable pain, and the standardized procedure.

On the other hand, compared with previous studies [120-129], the authors observed no significant association between intolerable pain and the use of premedication. In 2004, Giannoutsos et al. [123] revealed that 76 out of 112 patients chose not to take any premedication before the bone marrow examination and that 74 out of 76 patients were self-satisfied with their choice. Degan et al. [118] pointed out that a detailed explanation of the biopsy process in an instructive and comprehensive way permitted building trust among patients and physicians. It was necessary to confirm the patient's self-confidence level and was integrated with less pain during the iliac crest trephine BMB procedure [118, 130].

The different models of needles evaluated in the present examination had distinctive properties that make them convenient in specific diagnostic procedures. The triple-bevel crown tip needle has auxiliary cutting edges and sharp stylets to engage and penetrate cortical bone. As per the Care Fusion brochure, the triple-bevel trephine needles are believed to generate small insertion and extraction forces to puncture cortical bone. Further, the single-bevel biopsy needle helped retain the BMB sample with considerable lengths of assessed marrow and longer overall core quality. The side effects of the above-described premedication and its mortality and morbidity are usually very few. This may be further significant in outdoor patients, who must return home.

As some BMB indications like leukemia, lymphoma, and myelodysplastic syndrome need a considerable length of bone marrow to attain satisfactory sensitivity, it must be suggested to deploy the trephine needle, which supports the objective of a more significant length of bone marrow sample [131]. Usually, it is also beneficial to support the trephine BMB needles, which augment the bone marrow sample quality to avoid excessive biopsy repetitions and increase diagnostic yield. Furthermore, the triple-bevel trephine needle utilizes an acquisition cradle for smooth bone marrow sample acquisition. Variations in the needle handle can impact how the clinician interacts with the trephine biopsy needle, as in the case of manual biopsy. These variances may independently or together disrupt the sample quality, where the triple-bevel trephine needle-cutting procedure and specimen acquisition method typically yield a low bone

marrow sample. In contrast, triple-bevel needle shear stress permits a lower insertion force that fragments the bone microarchitecture and inherent bone marrow.

The primary outcomes of our examination have been the aspects conducted regarding unbearable pain. Neither gender, number of repetitions, premedication, age, nor hematologist experience, or information quality was significantly related during the trephine biopsy. These observations differ from earlier reports, except for the hematologist's experience, premedication, bone texture, and bone marrow length based on BMB indication. However, age was significant in one of the observations, whereas it appears to play a small part in another observation [121, 132]. The key findings were attributed to providing insufficient information to the patient before and during the procedure. A well-satisfied patient with information can establish a mental state and have lesser unbearable pain. Patients with unbearable pain usually had a poor impression of the bone marrow inspection procedure and the doctor.

The advantage of the present examination is that the hematologists/residents were blinded to a specific type of needle. Additionally, the analyses were based on the patient's gender, age, number of previous biopsies, and BMB indications and included differences from biopsy operators, length of bone marrow, level of anxiety/pain, and bone texture to interpret suitable influence produced in these features. An additional advantage of the present study is that the target length of each bone marrow sample based on BMB indication and interpretation has been considered, which remained un-attempted by Brestoff et al. [133] in their study. However, the limitation of the present study is that the hematologist performing the BMB with less experience was blinded to a specific type of needle. Still, the type of needle was not fixed. Due to this, hematologists face problems when handling different types of needles during the procedure. The study has been restricted to trephine bone marrow biopsy, and aspiration needle and smearing-related results have not been included.

Despite these drawbacks, current analysis indicates that trephine biopsy needle type can impact bone marrow quality. It is being suggested that the medical facilities performing BMB procedures evaluate the quality design whenever novel needle types are included. The primary objective of these head-to-head evaluations should be to confirm that BMB sample quality and length are not inadvertently compromised. Although the triple-bevel trephine needle employed in the present examination was related to poorer bone marrow quality, there was less pain during the procedure than the single-bevel needle. This needle design may be suitable in some medical situations, like a patient with dense cortical bone and operators who have not acquired an acceptable biopsy sample with an alternative needle design. However, based on the present study it has been suggested BMB performed on adult utilizing a single-bevel biopsy needle as the preferred technique to attain a BMB sample from the posterior iliac crest. But, if a patient wishes to use another needle design for biopsy or a single-bevel biopsy needle fails to acquire a suitable sample, a triple-bevel trephine needle should be tried.

Bone marrow examination is an effective and adequate technique for diagnosing hematological and non-hematological conditions. A trephine BMB reflects the topographical order of hematopoietic cells inside the marrow structure and provides a descriptive overview of marrow cellularity. The data illustrates a considerable effect of noble information provided via the hematologists/residents to minimize the anxiety/pain during the minimal invasive inspection. This information is frequently undervalued in a routine medical procedure, but it can be beneficial in minimizing the pain during a biopsy procedure. The information also recommends that the benefits and drawbacks of premedication be discussed with the patient, and then that approach should be incorporated into the patient's selection process.

4.2 FE Analysis of Conventional BMB Needle Insertion into Iliac Crest (Study 2)

In the present investigation, four process-specific criteria: velocity, skin coefficient of friction, bone coefficient of friction, and needle diameter, as individual variables of the simulation model, have been examined. Insertion tests consisting of 25 runs have been performed to evaluate the iliac crest simulation model developed for BMB with a conical needle. The needle was not rotated during different sets of tests in the insertion procedure. The stress and forces at the needle base have been recorded during the insertion process. The depth of insertion has been 15.35 mm throughout the tests.

4.2.1 Validation of the FE model

The multi-layer skin and bone tissue reaction force obtained using our axisymmetric FE model with two different cutting steps has been validated with the earlier proposed needle insertion force models [134-137]. A mesh independence test has been performed to acquire the best element size. Multiple simulations have been executed using the mesh size peculiar to CAX4R elements (1, 0.8 mm, 0.5 mm, 0.3 mm, 0.2 mm, and 0.1 mm) for the mesh independence test. No major difference in the stress value has been recorded for the element size ranges between 0.3 mm to 0.1 mm. Hence, as mentioned above, the results concluded that the outcome is convergent, and any additional decrease in mesh size does not significantly enhance the result. Thus, the most acceptable element size of 0.3 mm has been chosen throughout the simulation to conduct the study. A very fine mesh has been generated between the needle and iliac crest layers zone to achieve highly precise numerical results in higher stress and strain gradient regions. A contact algorithm provided surface-to-surface contact (Explicit) among the needle and iliac crest layers. The initial step has been from 0 to 4 mm of penetration depth; the needle tip progressively deformed the skin tissue until it got punctured. A sharp drop of insertion force recognizes this phase. The second step started instantaneously after the initial puncture (i.e., 4 mm to 15.35 mm cutting depth). The primary force constituent in the second step was the puncture force created while the needle tip constantly broke the bone tissue. In the present

study, the FE model expected the precise insertion force over time. The insertion force curves have been validated with the experimental results [134, 135] without normalizing the cutting force peaks. Compared to the skin tissue experimental results [134, 135], the variation has been, on average, less than 50% and has been 30% to 40% at the initial skin tissue puncture point. The obtained skin tissue insertion force has been in poor agreement with the experimental results since the skin tissue has been assumed to be an isotropic, heterogeneous, incompressible, and hyperelastic material in our simulations.

Further, the experimental and simulation studies available in the literature [135, 138, 139] have been performed at various concentrations of homogeneous phantom gel's environmental conditions, which are quite different from those in the simulations. Similarly, bone tissue simulation results have been compared with the experimental results available in the literature [136, 137] and obtained a deviation of 9% to 10% on average at the bone tissue puncture point. The bone tissue cutting behavior is assured of satisfying the fracture toughness and insertion force. The simulation model still expects precise cutting force values. It is visible from Table 4.4 that the insertion force data obtained from the present simulation design has been larger than the values available in the literature. The present method did not consider the resonance effect, which produces more vibration at different insertion velocity rates and causes corresponding variations in insertion force results [135].

Table 4.4: Validation of simulated needle insertion force with the experimental results

Sr. No.	**Needle insertion force (N)**			**Reference**
	Simulation	**Experiment**	**% Error**	
1.	10	7	30	[134]
2.	10	6	40	[135]
3.	220	250	-10	[136]
4.	220	200	9	[137]

4.2.2 Needle insertion and extraction forces

Standard needle insertion and extraction procedures consist of three simple contact steps between the needle and iliac crest layers, as depicted in Figures 4.5(a) and (b). The initial step, i.e., deformation (refer to Figure 4.5(a)), begins when the needle tip endures the phantom/tissue surface or boundaries and finishes. At the same time, these surfaces or boundaries are punctured, and the insertion force attains the highest value identified as peak force. The second step is the needle tip insertion which starts when the surface or boundaries of the phantom/tissue are punctured and finishes while the phantom or soft tissue slips up from the needle tip into the shaft. The final step begins immediately after the insertion of the needle tip, which is a transition from the needle tip to the shaft. It finishes when the needle contacts a new

phantom/tissue boundary or stops. The needle tip during the insertion step is exposed to the cutting forces and shaft to variable frictional forces because of the rise in interaction region among the tissue and shaft as the needle progressed.

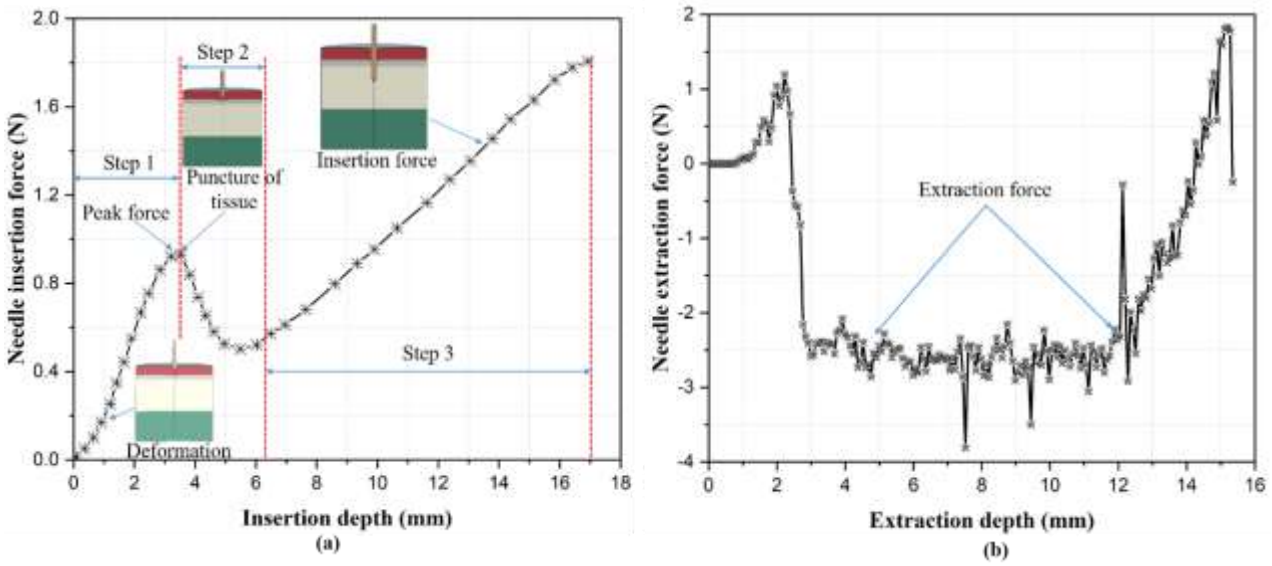

Figure 4.5: A standard needle (a) insertion and (b) extraction procedure plot

4.2.3 Effect of velocity and diameter on needle insertion

Figure 4.6(a-e) depicts the combined effect of different parameters (viz., needle diameter, coefficient of friction for skin and bone) on the insertion force at needle velocities, 1 - 10 mm/sec. The graphs plotted in Figure 4.6 demonstrate that when the needle is pushed into the multiple layers of the iliac crest model, the insertion force rises with the displacement of the needle. The puncture process begins when the needle tip touches the soft tissue's outer membrane. Due to the rigidity of the biological tissue, the needle tip could not enter the soft tissue before that point. As the penetration depth rises, the needle punctures the outer membrane of the living tissue. After that, the puncture needle penetrates soft tissue's outer membrane, and the response force abruptly decreases. The needle tip will cause soft tissue damage at this time, making it more uncomfortable. Because the section behind the needle tip scrapes beside the soft tissue, the stress on this part is lower than on the needle tip. The response force is the sum of the needle tip's cutting force on soft tissue and the friction force applied on the needle's outer wall. As the depth of the puncture rises, both the frictional and response forces rise.

Once the puncture occurs, the force drops rapidly and increases as the needle is pressed deeper into the skin and the bone. In the present study, the increase in needle insertion force depends on the needle velocity, diameter, and coefficient of friction of the skin and the bone.

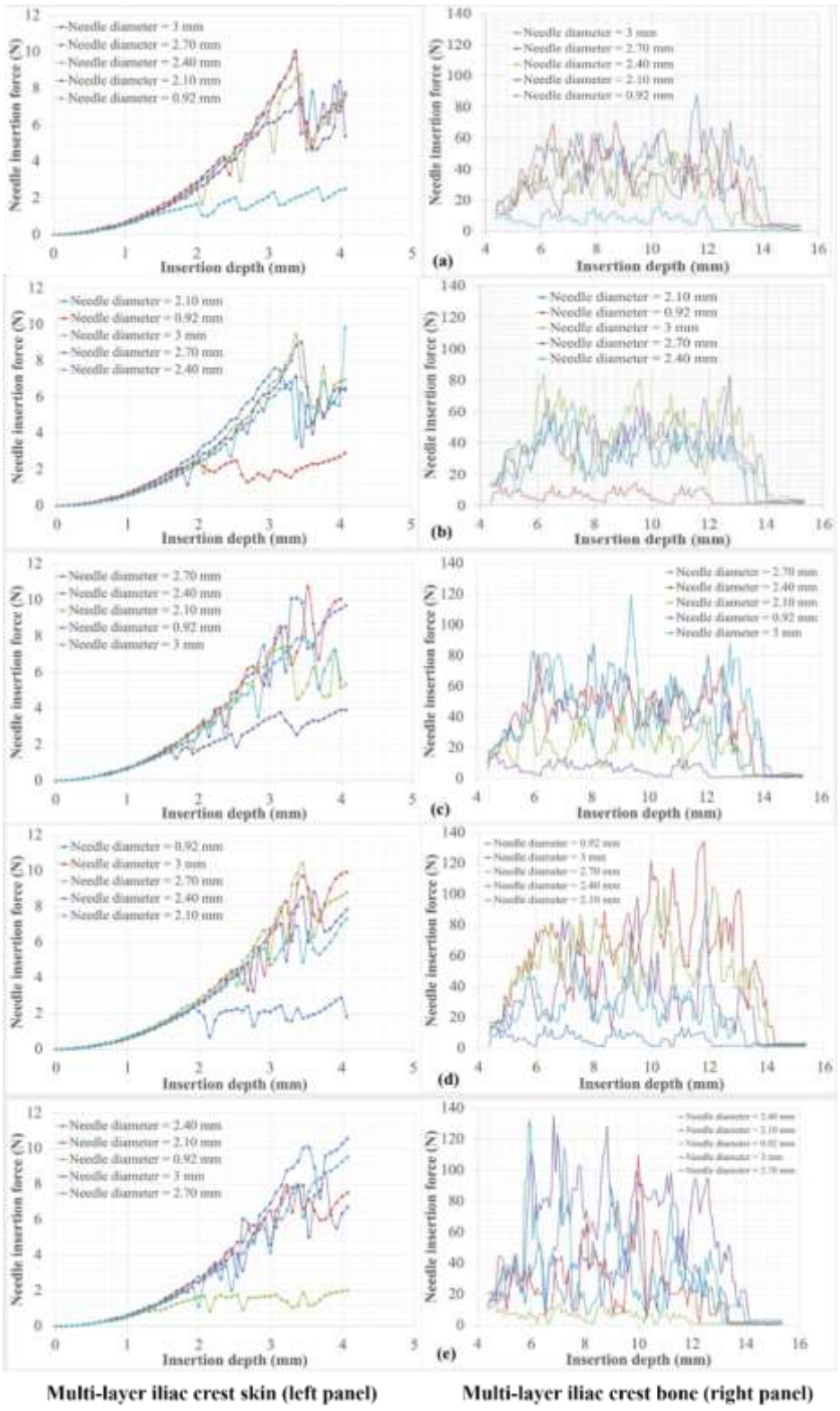

Figure 4.6: Needle insertion force for a depth of 15.35 mm (multi-layer skin and bone). The plot depicts results for insertion velocity of (a) 1 mm/sec, (b) 2.5 mm/sec, (c) 5 mm/sec, (d) 7 mm/sec, and (e) 10 mm/sec

The average insertion forces have been reported to be 28.975 N, 30.475 N, 31.613 N, 31.657 N, 35.735 N at velocities 1.0, 2.5, 5.0, 7.0, 10 mm/sec, with needle diameter of 0.92, 2.10, 2.40, 2.70, 3.0 mm, skin coefficient friction of 0.10 to 0.42, and bone coefficient friction of 0.30 to 1.03 while the insertion depth has been up to 15.35 mm. It is clear from the insertion force curve that the force due to the rise in tangential force rises along with the insertion depth and hence causes an increase in the insertion force. Once the tip of the conical needle touches the layers of the iliac crest model, the resistance force rises linearly from its initial value, i.e., zero. The puncture force then attains its peak value at a particular puncture depth of each layer, and this process continues until the needle reaches the desired location. The reason behind this is the increased sliding friction among the needle and layers of the iliac crest model. There is adequate friction between the walls of the needle and tissue layers when the penetration reaches a specific depth.

Datasets obtained from FE simulation for oscillations in the bone insertion force curve have been normalized beside the peaks using the data analysis software (MS Excel). The maximum force exerted on the needle during the experimentation was relatively more significant than 138 N (refer to Figure 4.6). In the case of all different gauge needles, a simple force vs. depth linear relationship has been detected for the entire five velocity penetration rates from 1 to 4 mm, as presented in Figure 4.6(a-e). A slight drop in the force between 10 and 12 mm is visible for 5 mm/sec velocity rate, with drop conditions survival being more critical for the latter. At the insertion depth up to 15.35 mm, the maximum insertion force for 10 mm/sec (i.e., high speed) experiments has been relatively more significant than 138 N, approximately 1.15 times higher than 5 mm/sec (i.e., medium speed) experiments and 1.56 times higher than 1 mm/sec (i.e., low speed) experiments.

4.2.4 Needle extraction

The graphs plotted in Figure 4.7 present the influence of different needle diameters and coefficient of friction of skin and bone on extraction force at the velocity rates varying in the range of 1 - 10 mm/sec. The average extraction force at a velocity rate of 1 - 10 mm/sec and needle diameter of 0.92 - 3.0 mm has been -1.43 N, -1.25 N, -1.0 N, -1.56 N, and -1.04 N, while the extraction depth has been 15.35 mm. The resistance force got reduced quickly once the needle has been withdrawn. When the resistance force dropped and reached zero, the compression of the multiple iliac crest layer on the needle changed to the tensile position. If the rigidity of the needle tip can be fixed, the tip angle should be sharpened to reduce the retraction force. The extraction force got reduced slowly during the extraction procedure.

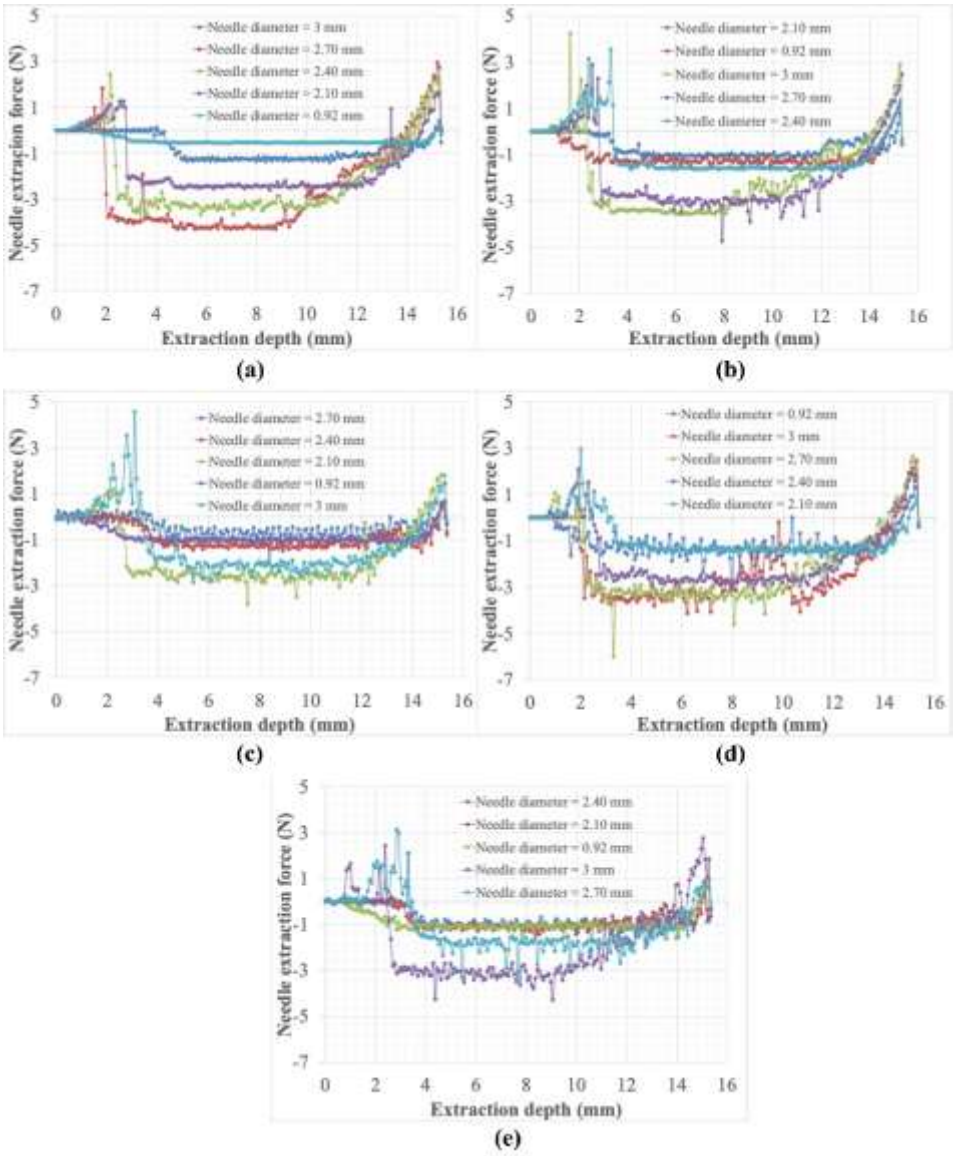

Figure 4.7: Needle extraction force measured during needle removal from a depth of 15.35 mm (multi-layer skin and bone).

4.2.5 Strain of multi-layered iliac crest model

Figure 4.8(a-e) depicts the strain contour results on the insertion and extraction process at different velocity and needle diameter values. The tissue could be deformed or cut as the maximum stress level of the needle tips is above the yield stress of the biological tissue. In a puncture biopsy procedure, a needle constantly penetrates and cuts the multiple layers of the iliac crest model. Pain experienced by patients is strongly correlated with the deformation of biological soft tissue and bone damage. The needle penetration at a particular velocity and diameter will cause bone damage and soft tissue deformation. The net strain of multiple layers of the iliac crest model (viz., skin tissue and bone) when bone damage and skin tissue deformation occurred during the biopsy has been shown in Figure 4.8(a-e).

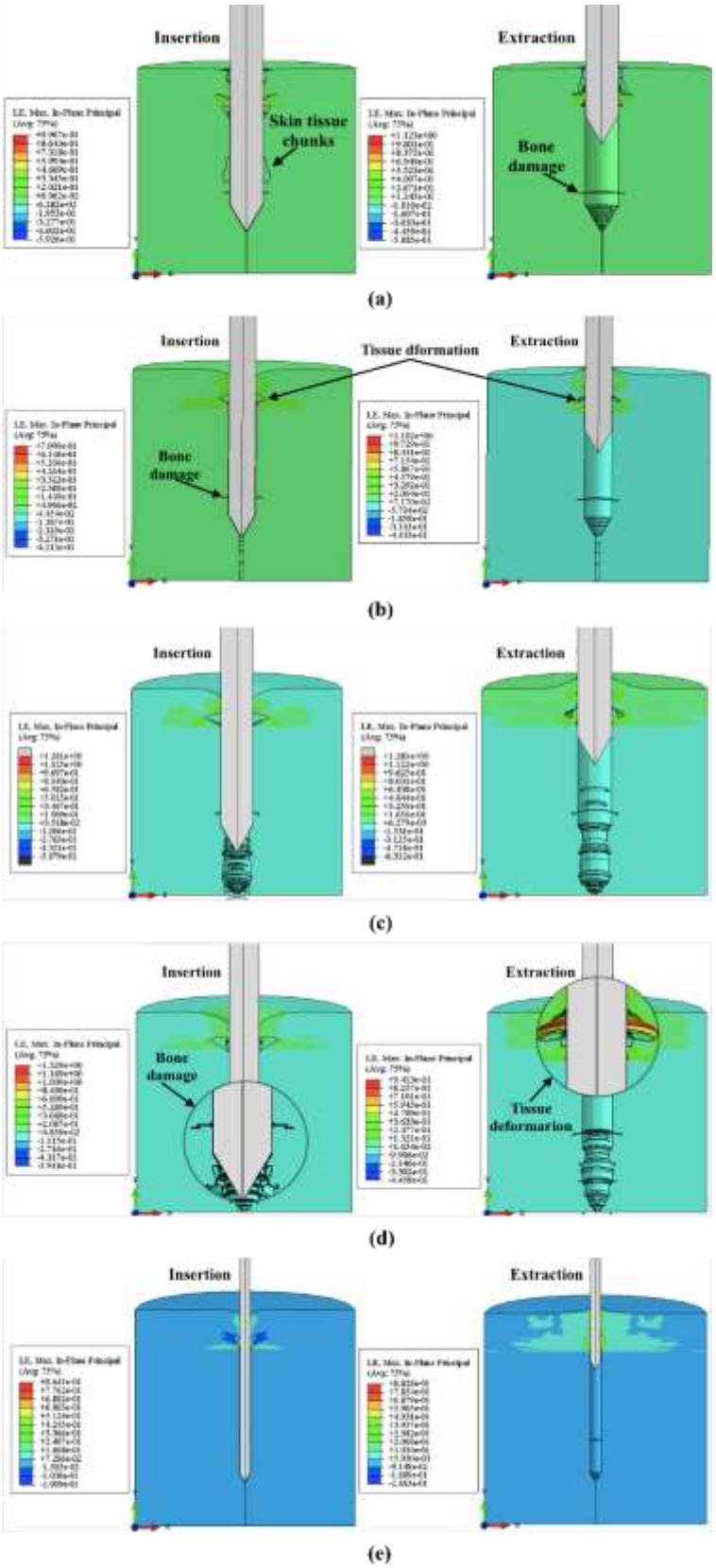

Figure 4.8: Strain contours of multi-layered iliac crest model at different velocities and needle diameters

During the insertion process, each layer of the biological skin tissue deforms in a concave pattern that follows the tip of the needle until the needle reaches the cortical bone. Once the needle reached the cortical bone, it further progressed inside it to acquire the bone marrow. The needle penetration with different diameters and speeds into the bone causes damage in the form of a crack on the cortical bone around the needle, as shown in Figure 4.8(d). The needle tip introduced a crack that extended into a circumferential hole by tearing and elongating both the skin and the bone, allowing the needle to be inserted into the skin and bone. During the insertion and extraction processes of the needle, the deformation of biological skin tissue and bone damage formed in the puncture procedure using the small diameter and less velocity needle (viz., 1 - 5 mm/sec and 0.92 - 2.40 mm) has been considerably less than that of the puncture procedure having a high diameter and velocity of needle (viz., 7 - 10 mm/sec and 2.70 -3.0 mm). Figure 4.8 shows that as the needle insertion depth rises, smaller tissue segments and irregular burrs become progressively visible on the contact surface between the multiple layers of the iliac crest model and needle. However, using less speed and small diameter needles has considerably enhanced bone damage and tissue deformation at the contact surface.

4.2.6 Biological skin tissue and bone stress

Figures 4.9(a-e) and 4.10(a-e) depict the von Misses and shear stress points of deformed skin tissue, damaged bones, and needles for different needle speeds and diameter cases. The development of deformation in different iliac crest layers increased as the penetration depth increased. It is initiated from a small portion restricted around the tip of the cutting needle with high-stress concentration (refer to Figure 4.9(a)). Continuous needle penetration increases tissue deformation, and the material before the needle-cutting tip encounters an augmented plastic deformation (refer to Figure 4.9(b)). The development of abundant shear band in front of the needle-cutting tip and around the shaft can also be detected as an outcome of the mutual influence of material anisotropy and the needle tip (refer to Figure 4.10(c)). These biological skin tissue and bone deformation processes proceeded continuously around the needle tip and along the shaft until a saturation condition was achieved, at which needle cutting force reached its highest value. After that value, the damage process and plastic deformation are progressively governed. The skin and bone layers begin to plastically deform at the free edge with extensive damage in the surrounding area (refer to Figure 4.10(c)). The softening of the material involved large plastic deformation resulting in a decrease in the stiffness and disintegration of the material (Figures 4.9 and 4.10). The stresses based on the less velocity and small diameter needle have considerably been lesser than the high velocity and large diameter needle.

Moreover, the patient experiences pain due to the insertion and extraction force on the skin tissue and bone. While there is less stress in the skin tissue and bone, the pain people experience is not evident.

However, in most cases, the location of maximum stress has been approximately similar. During the insertion procedure, maximum stress on the multi-layered iliac crest model has been transmitted to the edge of the needle tip, as shown in Figure 4.9(b). In contrast to the stress distribution of bone and skin tissue, the location of maximum needle stress has almost been in the middle portion of the needle. Furthermore, the maximum needle stress location always occurs at the needle body's center.

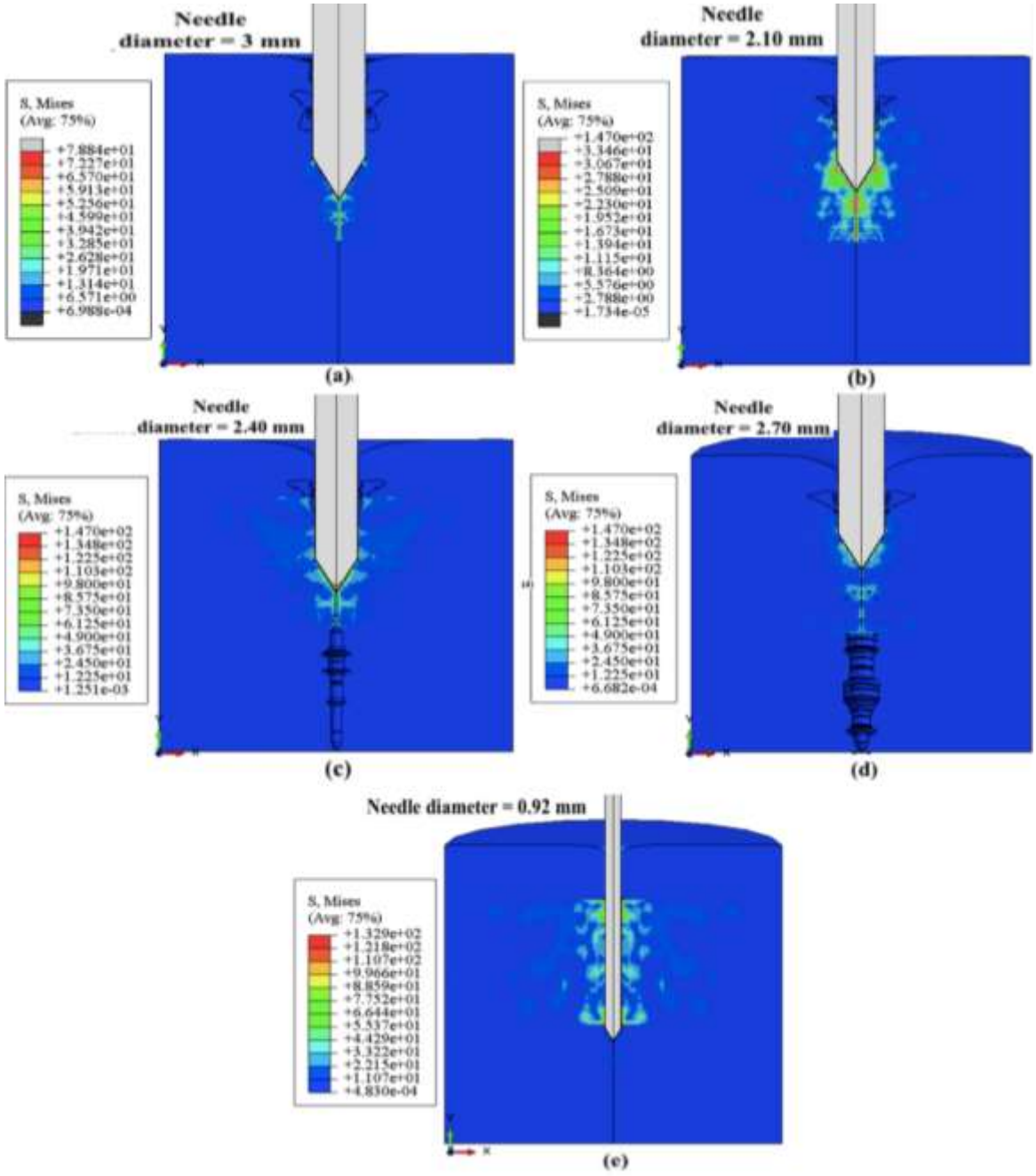

Figure 4.9: Equivalent stress (Von Mises, in MPa) element distribution at different insertion depths with various needle diameters and velocities

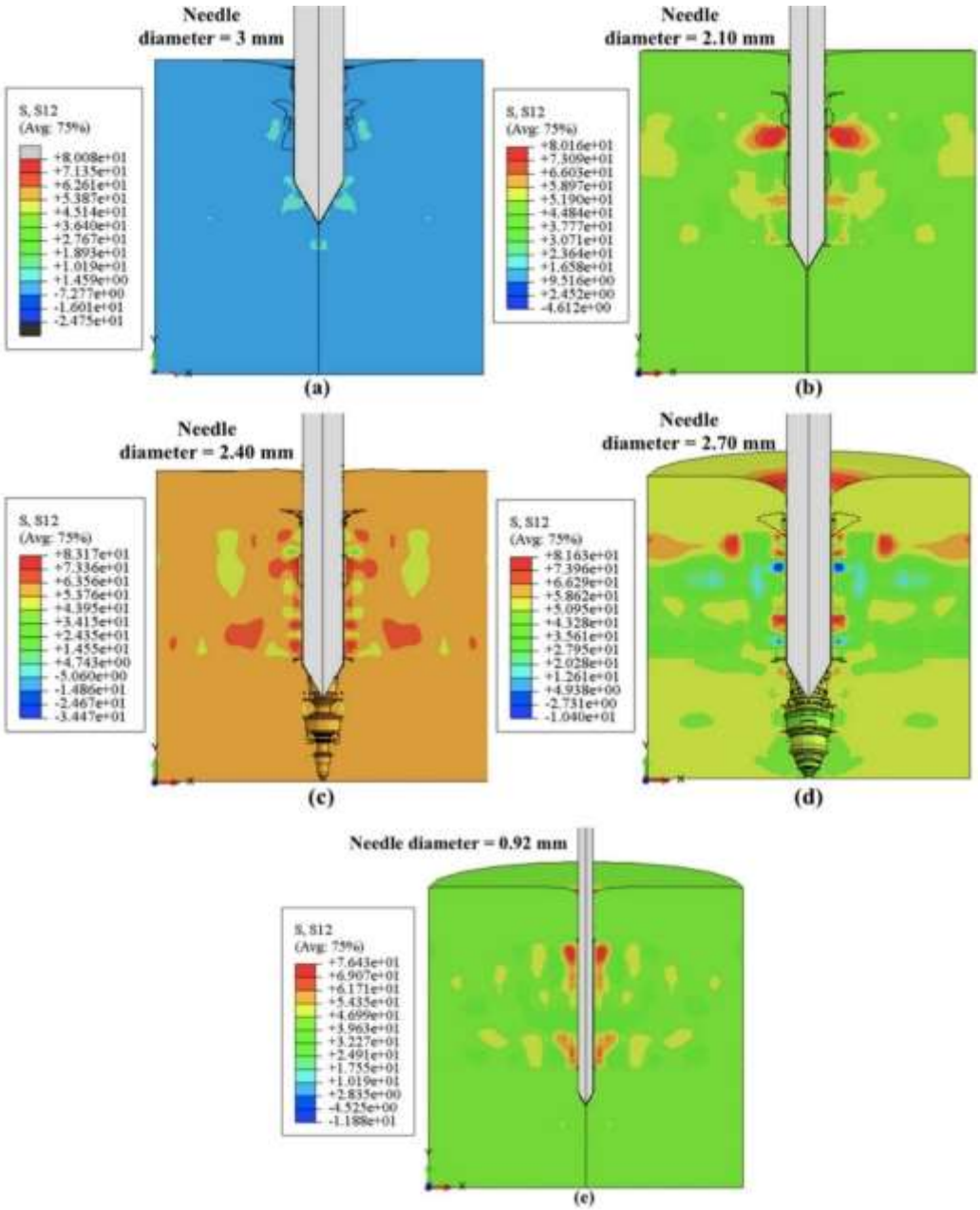

Figure 4.10: Shear stress (S12, in MPa) element distribution at different insertion depths with various needle diameters and velocities

4.2.7 Limitations and perspectives

The major drawback of our investigation is its axisymmetric design which has been chosen to avoid very long simulation times due to its explicit algorithm nature. We have tried to bridge this drawback by precisely matching the cases and controls. The second drawback is considering the needle design to be a rigid body. The current study did not consider the needle deflection caused by the axisymmetric FE model.

In addition, we have not considered the needle rotation during different sets of trials in the insertion procedure. Though the procedures adopted in the present study and described earlier in the literature are robust, a well-validated FE 3D model to estimate the needle-tissue interaction for the multi-layer iliac crest biopsy model is still required. The proposed model may be expanded to include other characteristics such as strain-rate sensitivity, torque, needle bending, and needle vibration. The findings of this study provide a foundation for the advancement of sophisticated models required for a better understanding of the intricate process of BMB needle and skin–bone tissue interaction during the biopsy procedure. These models may be used to accelerate the design and optimization of BMB instruments that are physically utilized, reducing the number of trials and pain.

4.3 FE Analysis of Conical-Shaped Conventional BMB Needle Insertion into Iliac Crest (Study 3)

In this study, two specific biopsy procedure parameters, viz., insertion velocity rate and needle diameter, have been investigated as distinguishing variables of the numerical analysis. Further, the coefficient of friction for skin and bone has been kept constant throughout the simulation process. Eleven needle insertion experiments have been performed to estimate the established multi-layer iliac crest model for bone marrow biopsy. Experimentations involved six values of insertion velocities ranging from 1 mm/s to 10 mm/s and five values of different biopsy needle diameters in the range of 0.92 mm to 3 mm, respectively. The needle rotation has not been considered because an axisymmetric model has been used to study the needle insertion process. Different needle insertion forces and stress results have been documented during the penetration procedure. The biopsy needle penetration depth in skin-bone tissue has been kept at 15.35 mm throughout the experiments.

4.3.1 Effect of needle insertion velocity

Figures 4.11(a) and (b) depict the insertion force behavior on the biopsy needle during insertion into the skin and bone layers at various velocity rates from 1 mm/sec to 10 mm/sec. Four insertion peaks have been detected after a constant increase in force, followed by a rapid drop because of the puncture of various skin and bone tissue layers. The first step occurred between 0 to 4 mm of cutting depth, during which the needle cannula gradually damaged the tissue until a first cutting occurred, which has been detected by a rapid reduction in response force. The second step began shortly after the first (from 4 to 15.35 mm of the cutting depth). As the cutting depth increased, the response force steadily increased. The primary essential part of this process in the second step has been the cutting force created when the needle tip constantly penetrated the tissue and the friction force produced at the contact between both the needle walls and the tissue. The observed forces show that altering frictional force increases insertion force.

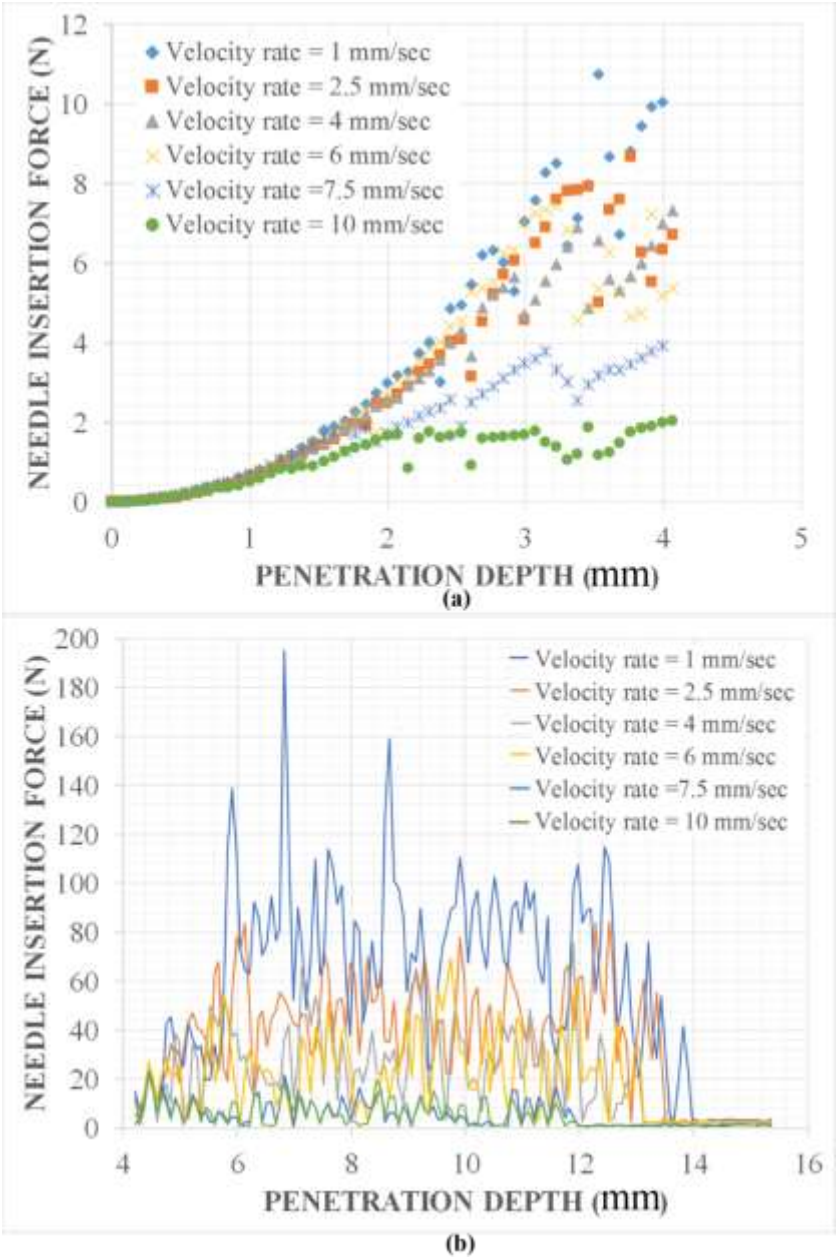

Figure 4.11: Needle insertion force vs. penetration depth plot for different velocity rates at (a) skin tissue and (b) bone tissue layers

The maximum insertion force utilized by a needle in this experimentation has been approximately 10 N when the needle penetrated the skin layers (refer to Figure 4.11(a)) and somewhat higher than 180 N when penetrating bone layers (refer to Figure 4.11(b)). This takes place during a needle insertion depth of 15.35 mm at a penetration velocity rate of 1 mm/sec, 2 mm/sec, 4 mm/sec, 6 mm/sec, 7.5 mm/sec and 10 mm/sec. A perfect linear insertion force vs. penetration depth relationship has been observed from 1 to 4 mm for six needle penetration rates, as shown in Figure 4.11(a). At the needle insertion depth of 5-10 mm, approximately 190 N of force is required for the biopsy needle to progress through the bone tissue,

irrespective of penetration speed (refer to Figure 4.11(b)). The linear insertion force vs. penetration depth curves then diverges once the needle tip crosses the 4 mm depth and reaches the bone. Once the needle tip comes into contact with the surrounding membrane of the soft tissue, the penetration process will start. The needle tip has been unable to penetrate the soft tissue prior to that point due to biological tissue's stiffness. The biological tissue's outer layer is pierced by the needle as the puncture depth increases. Following this, the needle cuts the outer membrane of the soft tissue, and the reaction force suddenly drops. At this point, the needle tip will induce soft tissue damage, making the procedure more painful. The tension on the region beyond the needle tip is smaller than that of the stress on the needle tip because it rubs beside the soft tissue. The combined cutting and friction forces applied to the needle's exterior wall and soft tissue are referred to as the reaction force. Both the frictional force and the reaction force increase with the depth of the penetration.

Further after this point, maximum average needle insertion forces have been experienced via those biopsy needles, which have been pushed forward at 1 mm/sec. In contrast, the minimum average insertion forces have been needed for those biopsy needles that progressed at 10 mm/sec. A decrease in average needle insertion force among 10 and 14 mm is evident for 2.5, 4, and 6 mm/sec insertion velocity rates, by the decrease conditions, being very substantial for the latter. At 15.35 mm penetration depth, the maximum insertion force for 1 mm/sec insertion velocity has been relatively above 190 N, which has been approximately 6.7 times higher than for the case of 10 mm/sec insertion velocity experiment.

4.3.2 Effect of needle diameter

The biopsy needles of different diameters penetrated several layers of skin and bone up to a depth of 15.35 mm and then extracted back. The experiment has been performed with five combinations of needle diameter, and the coefficient of friction values have been kept constant for both skin and bone tissue layers. Figures 4.12(a) and (b) show the needle insertion force vs. penetration depth plot for different needle diameters during the insertion procedure. The plot depicts that as the biopsy needle penetrates different skin and bone tissue layers, the force increases with the movement of the needle. When a puncture takes place, the insertion force drops quickly and as the biopsy needle further penetrates the skin and bone tissue, the insertion force begins to increase again. The maximum average needle insertion force has been reported to be 10 N for skin tissue and over 120 N for bone tissue with a needle diameter of 3 mm. It is evident from the needle penetration force plot that the insertion force increases because of the increase in tangential force with a depth of penetration and therefore causes augmentation in the insertion force requirement.

If the needle tip stiffness could be ensured, the needle tip angle should be sharpened to reduce the penetration and extraction force. It has been caused by an increase in sliding friction between the skin-bone and the needle. To overcome the sliding friction, needle loading energy has been employed to rupture skin-

bone tissue. When the needle makes contact with the artificial skin, the resistance force raised linearly from zero. During the insertion procedure, the artificial skin becomes concave and distorted beneath the progressing needle tip. By straining and tearing the artificial skin, the needle tip created a crack that developed into a circumferential hole, allowing needle penetration into the skin. The results acquired from numerical modeling for bone insertion force plots fluctuations have been normalized along the peaks using MS Excel data analysis software.

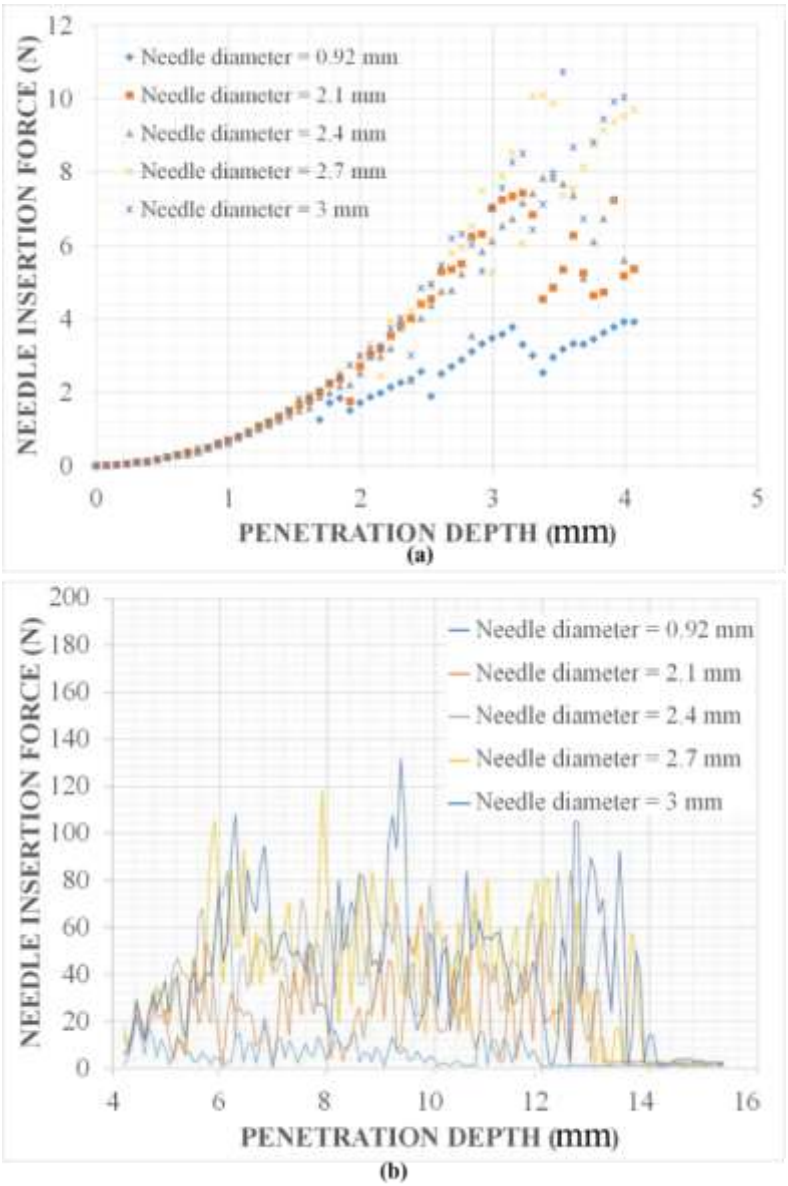

Figure 4.12: Needle insertion force vs. penetration depth plot for different needle diameters at (a) skin tissue and (b) bone tissue layers

4.3.3 Needle extraction process

Figures 4.13(a) and (b) show the plots for needle extraction force at different insertion velocity rates, 1 mm/sec to 10 mm/sec and various diameters of biopsy needles. The resistance force dropped rapidly when the biopsy needle has been removed from the skin and bone tissue layers during the simulation process. Once the resistance force starts to reduce and arrives at zero, the compression zone of skin and bone layers on the biopsy needle turns into a tensile zone. If the stiffness of the biopsy needle might be static, the angle of the needle tip should be sharp-edged to decrease the force of needle extraction. It has been clear from Figure 4.13(a) and (b) that the extraction forces of the needle gradually decrease during the needle removal process. As mentioned above, the average extraction force at different insertion velocity rates and needle diameters has been 0.69 N and 1.12 N, respectively, when the depth of extraction has been 15.35 mm.

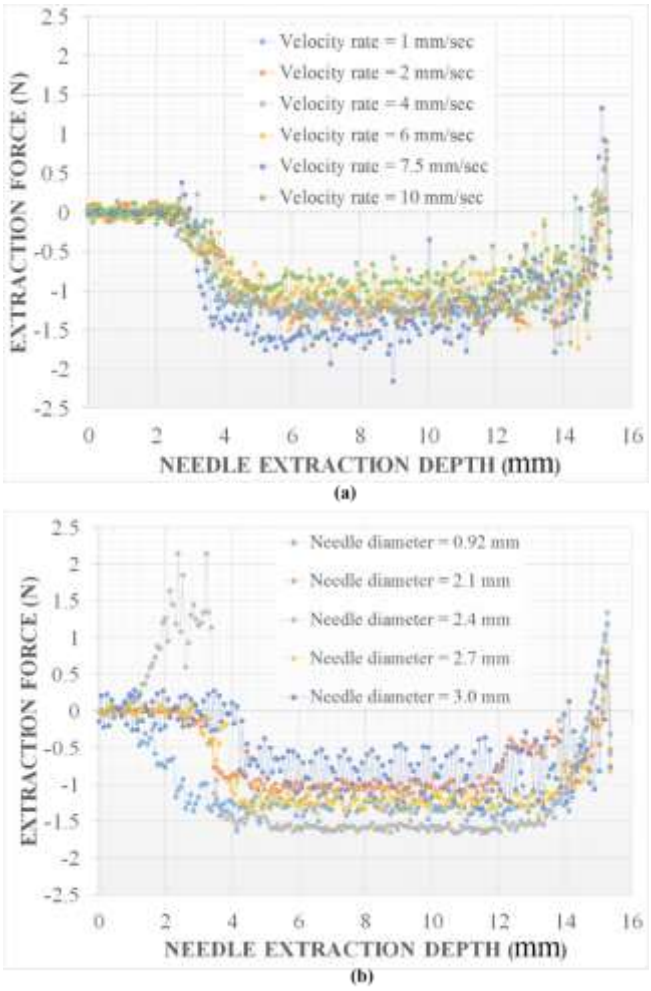

Figure 4.13: Needle extraction force vs. extraction depth plot for (a) different velocity rates and (b) needle diameter at 15.35 mm depth

4.3.4 Stress in skin and bone tissue

A stress path is a curvature whose tangents concur along with the principal stress directions on each point. It has also been recognized that the deformations in tissue and bone cracks would develop from the already existing defects in the area where stresses approach the highest tensile value. Using different needle diameters and insertion velocity rates cracks will generate at the interaction edge with an increase in stress criterion. Due to the axisymmetric nature, the stress state will propagate towards the penetration direction. Figure 4.14 depicts the initiation of stress and maximum stress contours achieved during the numerical analysis. It has initiated from a pretty small portion restricted around the tip of the cutting needle with a high-stress concentration (refer Figure 4.14(a)). The stresses during the biopsy needle and skin-bone tissue interaction drop quickly when it moves away from the interaction (refer to Figure 4.14(b)).

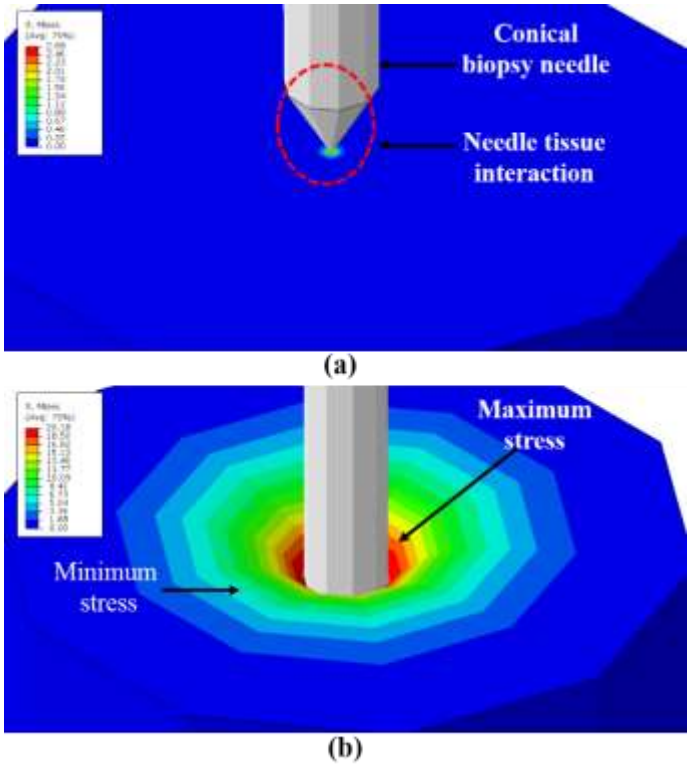

Figure 4.14: FEM results of equivalent stresses distribution around the needle tip

The stresses arising from the interaction zone are independent of the needle profile and are based only on applied parameters. These stresses during the needle penetration into the skin and bone tissue can be estimated by the input parameters used on the needle tip. At a substantial strain value, the needle tip caused a fracture, which widened a circumferential hole by pushing and tearing the artificial skin, permitting the needle tip penetration into the skin. The crack faces have been wedged open in the same way as needles were inserted into skin. The artificial skin puncture has been a planar mode I fracture. During the insertion

process, the needle penetration energy has been absorbed by the artificial skin, causing skin straining and rupture. Resistance increased when the energy has been transmitted through the interaction between the needle and the artificial skin. As demonstrated in Figure 4.14(a), the largest penetration stress and strain occurred at the needle tip. As a result of the combined interaction of material anisotropy and the needle tip, an extensive shear band develops at the front of the needle cutting tip and across the shaft. Each layer of the biological skin tissue deforms in a concave manner as the needle is inserted, following the point of the needle until it enters the cortical bone. The needle continued to advance within the cortical bone after it made contact with it in order to collect the bone marrow. It has been found from the figure that stresses have been maximum near the needle tip and then quickly reduced to minimum values as measured away from it. The maximum stress takes place at a point along the needle shaft away from the needle tip (refer to Figure 4.14(b)).

4.4 FE Analysis of Bio-Inspired BMB Needle Insertion into Iliac Crest (Study 4)

The conventional BMB needles discussed in the previous section are extensively utilized in medical procedures to extract biological tissue for the purpose of identifying specific lesions or abnormalities found during a medical examination or radiological scan. The forces applied by the needle during the cutting operation significantly impact the sample quality. Excessive needle insertion force and possible deflection might cause tissue damage, compromising the integrity of the biopsy specimen. This study aims at proposing a revolutionary bioinspired needle design that will be utilized during the BMB procedure. This work has established several design factors: barb shapes and geometry, viz., barb height, barbed back angle, barbed front angle and barbed proportion length. The impact of these parameters on the insertion and extraction forces during the multi-layered tissue piercing process has been studied. A 3D finite element multi-layer iliac crest model has been developed to investigate the barbed needle tip (bevel) effect, insertion velocity, and barb shapes. Further, the needle deflection, shear stress and von Misses distribution around the barbed needle have also been studied. The present study intends to enhance accuracy, minimize patient discomfort, avoid deflection and clogging, and increase the efficiency of BMB procedures by developing a needle based on the stinger of a honeybee.

4.4.1 Validation of the model

The results obtained from the present numerical study have been validated with the results from the experimental and numerical studies by Jushiddi et al. [140]. Jushiddi et al. [140] experimented on biological porcine liver tissue to simulate hollow needle insertion. The authors reported that the computational multi-layer model produced more accurate and realistic simulation results for needle insertion into the biological porcine liver tissue than simpler models that do not consider the tissue's multi-

layer structure. Referring to the insertion experiment on biological porcine liver tissue [140], a general 3D multilayered liver model using the Lagrangian-based FE modeling technique has been created in our study to simulate the needle-tissue interactions during hollow needle insertion, as shown in Figure 4.15. The simulation has been carried out with the same boundary conditions and material properties as used by Jushiddi et al. [140], with a hollow bevel needle having inner and outer diameters of 0.57 mm and 0.71 mm, respectively. The hollow needle penetrated the tissue vertically at a constant speed of 2.5 mm/s during the simulation to replicate the needle insertion experiment. The study used ABAQUS 2018 software to predict the insertion force during a 12-second- and 30-mm insertion depth simulation with a steady time increment of 1e-4. The simulation produced satisfactory results that agreed well with the experimental findings reported by Jushiddi et al. [140] (refer to Figure 4.15).

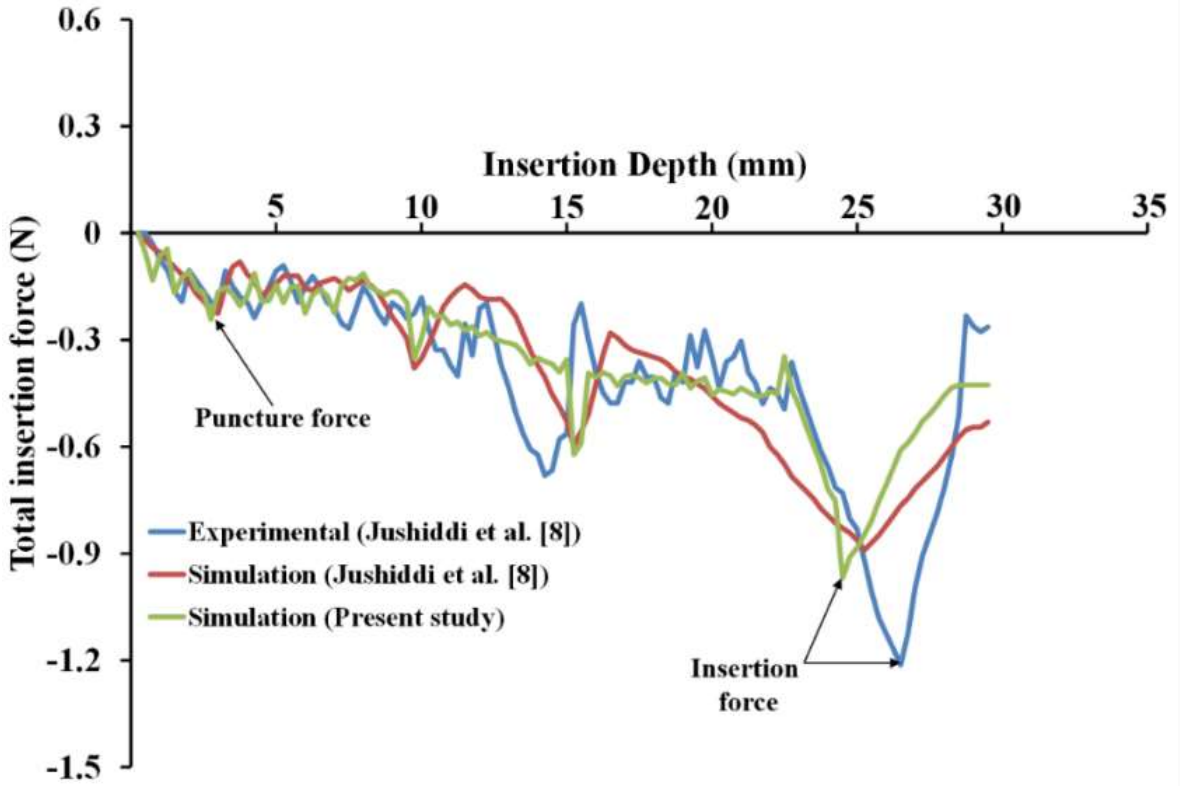

Figure 4.15: Comparison of insertion force between present results and the results by Jushiddi et al. [140]

4.4.2 Effect of barbed front angle on the insertion force

Various barbed biopsy needles have been introduced into the iliac crest (five simulated skin-bone tissue domains) specimens up to a depth of 53 mm with velocities in 3-20 mm/sec range, as shown in Figures 4.16 and 4.17. The insertion force for various needles has been studied using three phases of a complete penetration simulation process (refer to Figure 4.16). The three phases have been: 1) the skin tissue and barbed biopsy needle come into contact with each other, 2) the needle tip enters the skin tissue

and 3) the penetration needle punctures the skin tissue up to a depth of 10 mm (refer to Figure 4.16). The needle has been anchored in the cortical bone after 10 mm and penetrated further to puncture the cancellous and cortical bone up to a depth of 53 mm (refer to Figure 4.17). The penetration forces of the bioinspired barbed biopsy needle have been tested at various values of α_1 and have been shown in Figures 4.16 and 4.17. It can be seen from Figures 4.16 and 4.17 that, during the insertion of the needle deep into the skin-bone tissue layer, the insertion force increases with the needle penetration. The needle punctures the outermost layer of the skin tissue as the insertion depth increases. The reaction force then quickly reduces as the penetration needle breaks through the outer layer of the skin tissue. As soon as the puncture occurs, force immediately decreases and increases again when the needle advances into the skin and eventually into the bone. The space between two barbs on the needle shaft is very small when α_1 is 147°. As a result, a significant drop in the frictional area is not evident. The space between the barbs begins to broaden when α_1 changes from $157^{\circ}$to 170° indicating a reduction in the frictional area and insertion force. For the insertion depth range of 0-10 mm (skin tissue layers), the insertion force got reduced by 26.66% on average when employing a barbed biopsy needle with $\alpha_1 = 170^{\circ}$ compared to 147°. When compared to a conventional bevel needle, the insertion force got reduced by an average of 49.39% at an insertion depth of 10 mm when using a barbed needle with $\alpha_1 = 147^{\circ}$(see Figure A1; Appendix). This drop occurs regardless of the values of other parameters; therefore, this could not be the ultimate minimal. The pattern found in this series of investigations could be observed for any other combination of parameters. ($\alpha_1, \mathrm{h}, \mathrm{t}_b$ and L_b). The appropriate statistical tool (MS Excel) has been used to normalize the datasets generated from the numerical simulations for fluctuations in the bone insertion force, as shown in Figure 4.17. The needle is subjected to an extreme force of about 80 N during the study. For all values of α_1, a slight drop in the force can be seen when the insertion depth varies from 25 mm to 40 mm. A reduction in the insertion force of 8.6% on average is evident while using a barbed biopsy needle with $\alpha_1 = 170^{\circ}$as compared to 147° in the insertion depth range of 10-53 mm (bone tissue layers, refer to Figure 4.17). However, during the needle insertion into the bone with the insertion depth ranging from 10 to 53 mm, the insertion force got reduced by an average of 28.32% when using a barbed needle with $\alpha_1 = 147^{\circ}$ compared to a conventional bevel needle (see Figure A2; Appendix).

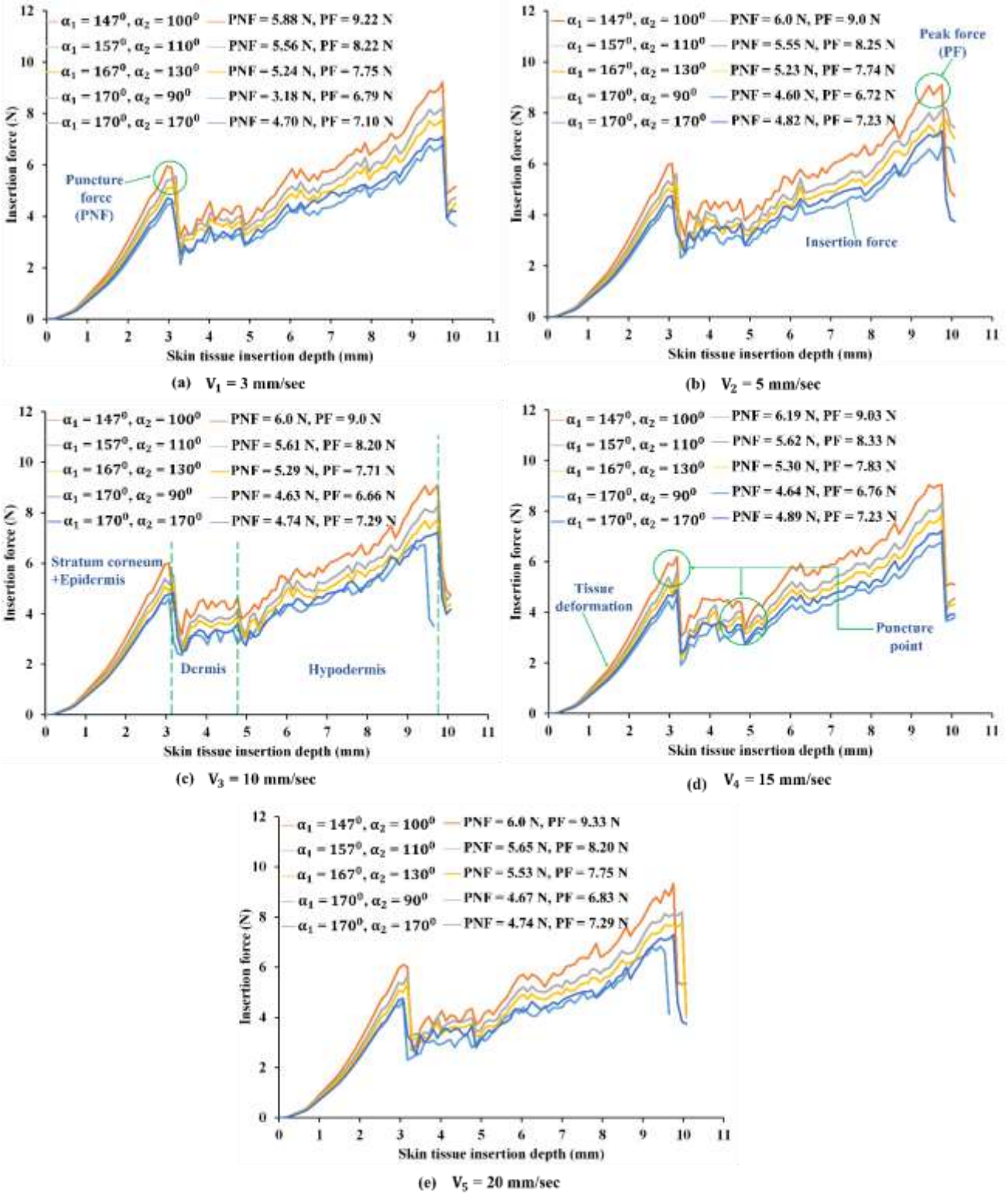

Figure 4.16: The relationship between the needle (barbed biopsy needle) insertion force and the insertion depth in skin tissue layers with various values of α_1 and insertion velocities

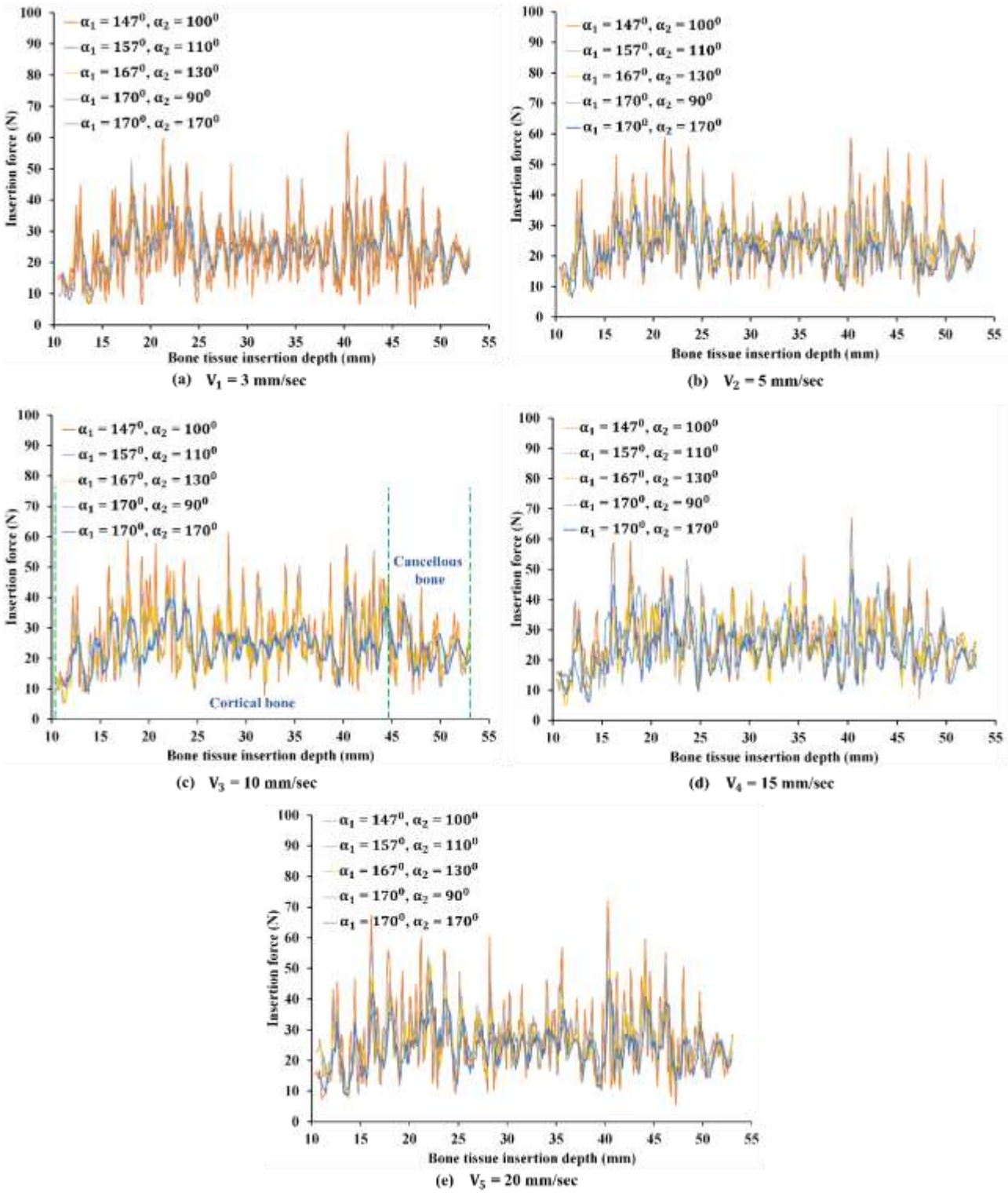

Figure 4.17: The relationship between the needle (barbed biopsy needle) insertion force and the insertion depth in bone tissue layers with various values of α_1 and insertion velocities

4.4.3 Effect of barbed back angle on the extraction force

A large value of α_2, for instance, is expected to increase the frictional area as well as the insertion force of the needle.

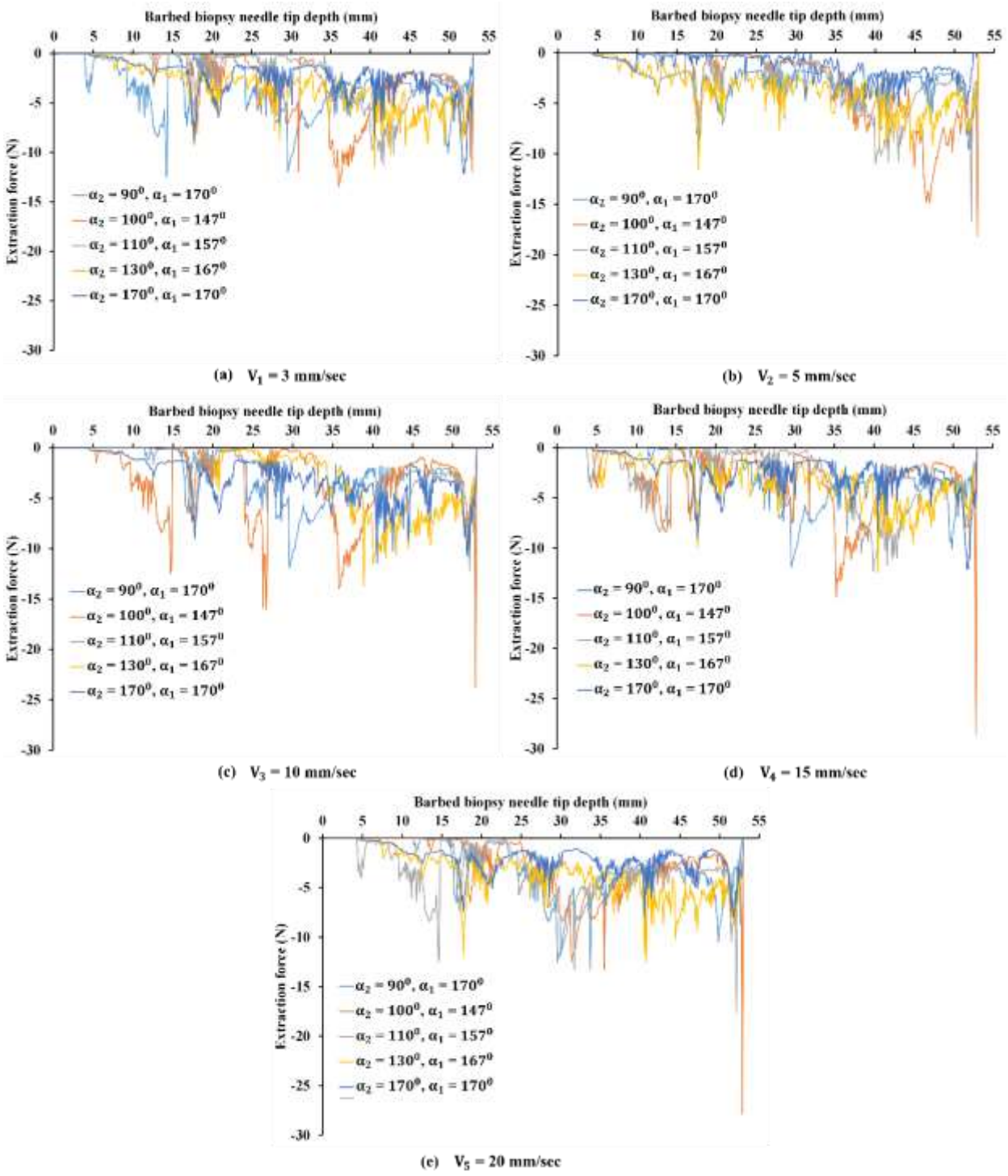

Figure 4.18: The relationship between the needle extraction force and the needle depth with various values of α_2 and extraction velocities

Since the real issue with employing barbs in the needle designs is the higher extraction force, the effect of α_2 on the extraction force of the biopsy needle is also essential. The effect of α_2, on the frictional force generated during needle insertion has been presented in this section. The extraction process begins after the completion of insertion (i.e., at an insertion depth of 53 mm). The extraction forces of biopsy needles having distinct values of α_2 are not much different, as can be seen in Figure 4.18. In other terms, the fluctuations in the extraction force with α_2 is minimal. Even though α_2 seems to be not influencing the penetration force, α_2 value of 170° warrants a lower insertion force. At a penetration depth of 53 mm, the extraction force has been reduced by 57.54% on average when employing a barbed biopsy needle with $\alpha_2 = 170^{\circ}$ as compared to $\alpha_2 = 100^{\circ}$. Compared to a conventional bevel needle, the extraction force got reduced by a maximum average value of 64.18% at an insertion depth of 53 mm when using a barbed biopsy needle (see Figure A3; Appendix). The extraction force values acquired for barbed biopsy needles with various values of α_2 have been very close. This indicates that the change in the extraction force with α_2 has been found to be moderate. In the present series of studies, using a barbed biopsy needle with $\alpha_2 = 170^{\circ}$ results in most significant decrease in the insertion force. Hence, depending on the insertion and extraction forces measured for biopsy needles with different values of α_2, it can be interpreted that $\alpha_2 = 170^{\circ}$ is significant.

4.4.4 Stress analysis on skin-bone domain during insertion and extraction procedures

The barbed biopsy needle continuously penetrates and punctures several layers of the iliac crest during a needle biopsy procedure. As the stress concentration on the needle tip is greater than the yield stress of the tissue, the tissue may get cut or deformed. Patient pain is significantly correlated to bone fracture and soft tissue deformation. Patient experiences less pain during the procedure when there is less stress on the skin and bone. The FEM stress distribution analysis procedure has been separated into two phases: insertion and extraction. Figures 4.19 and 4.20 depict the stress distribution on the iliac crest around the barbed biopsy needle throughout the insertion and extraction procedures. During the penetration procedure, every layer of skin-bone tissue domain deforms in a concave shape that accompanies the tip of the biopsy needle until it penetrates the cortical bone. When the barbed biopsy needle tip interacts with the top layer of the skin, the tissue deforms initially beneath the progressing tip unless significant stress causes skin penetration.

The maximum stress occurred at the barbed biopsy needle tip area with the highest value of 16.3 MPa, as can be seen from Figure 4.19(a). As the tip progresses, the stress at the uppermost layer of the skin rises, making the needle tip more straightforward to cut away. Several nodes got split due to the elimination of "dead" skin mesh elements once the effective stress on the skin in an element close to the needle tip met its defined failure criteria, as can be seen from Figures 4.19(a) to (c). Significant stress accumulation close to the barbs expands the skin and becomes distorted, as shown in Figure 4.19(c). Once the needle enters the

skin layers and gets anchored into the cortical bone, it progresses further to acquire the bone marrow sample (see Figure 4.19(d)).

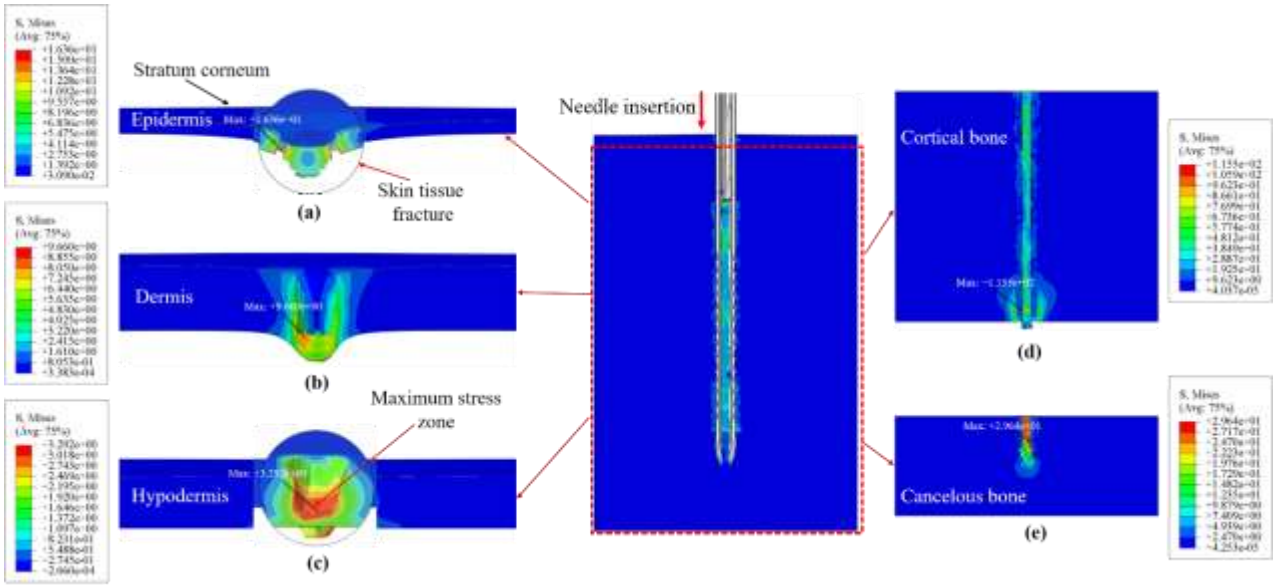

Figure 4.19: Stress distribution on the iliac crest (skin-bone domain) around the barbed biopsy needle during insertion

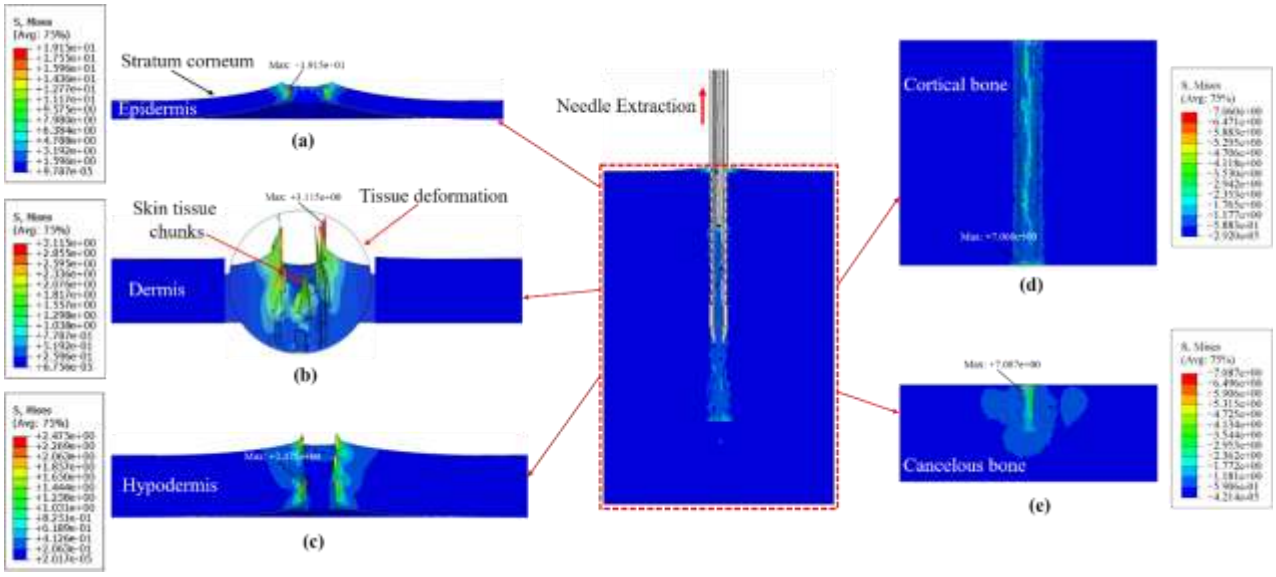

Figure 4.20: Stress distribution on the iliac crest (skin-bone domain) around the barbed biopsy needle during extraction

The maximum stress at the barbed biopsy needle tip location has been 115.5 MPa during needle insertion into the bone (see Figure 4.19(d)). Figures 4.20(a) to (e) depict the stress distribution during the extraction procedure. The skin's compression condition immediately changed into a tensile condition when the needle was extracted. The barbs on the needle shaft got jammed into the skin-bone tissue, and the stress

has been distributed around the barbs, as seen in Figure 4.20. The skin around the barbed shaft eventually exhibited a noticeable convex shape as the needle was extracted upwards. Tissue stickiness has been caused by the jammed barbs, leading to tissue deformation during the extraction process, as shown in Figure 4.20(b). Since this needle shaft and its barbs have been considered a rigid body, the needle and barbs are preserved unbroken and unbent.

4.4.5 Tissue deformation

Figures 4.21 to 4.23 depict the tissue deformation and bone damage during different insertion velocities (3 mm/sec to 20 mm/sec) using various barbed biopsy needle specifications. Before the needle penetration procedure, the needle tip has been assembled on to the top of the skin tissue in the FE model. The hollow barbed biopsy needle has been introduced into the simulated skin-bone tissue up to a depth of 53 mm, then bone damage and tissue deformation have been measured. As demonstrated in Figures 4.21 to 4.23, an increase in needle velocity enhances tissue deformation. The work done during tissue deformation and needle displacement has been transformed into elastic strain energy retained in the deformed tissue and bent needle. The lesser the overall strain, the smaller the tissue deformation and bone damage, as can be seen in Figure 4.21. As the insertion velocity increases, the strain value closer to the skin-bone tissue increases, which causes more skin-bone tissue rupture (see Figure 4.22).

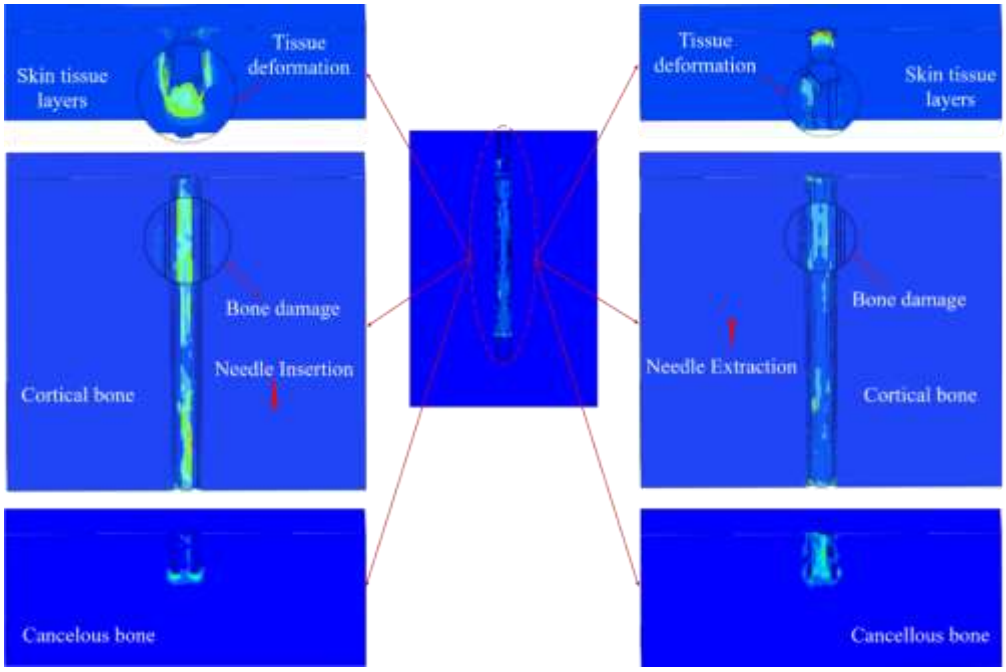

Figure 4.21: Tissue deformation and bone damage for both needle insertion and extraction at minimum insertion velocity (3mm/sec)

The damage and deformation of skin-bone tissue developed during the insertion and extraction procedures of the needle have been significantly less when using a small insertion velocity (viz., 3-10 mm/sec) compared to the high insertion velocity of the needle (viz., 10-20 mm/sec). The deformation increases whenever the needle penetration rate is enhanced during non-rotational needle insertion, as can be seen from Figure 4.23.

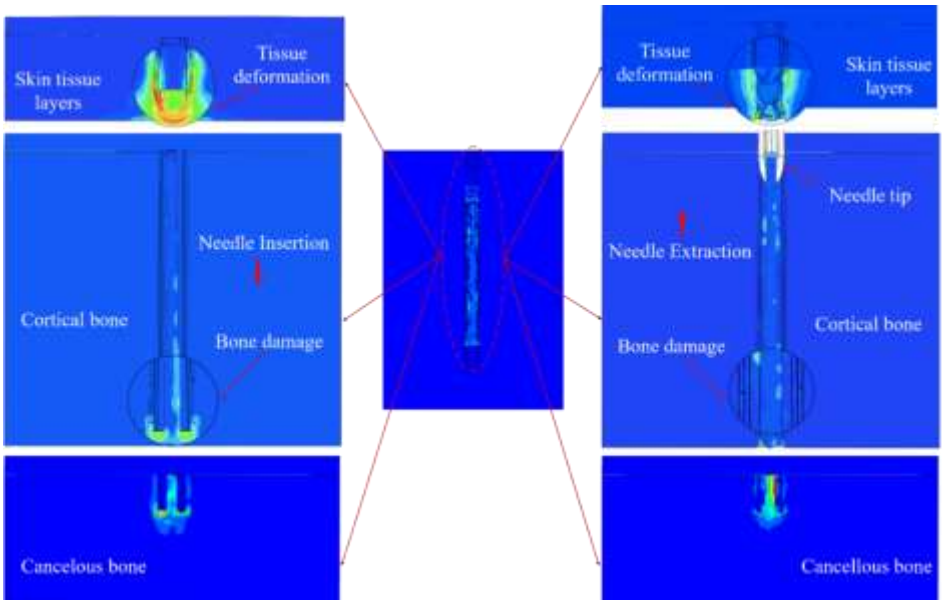

Figure 4.22: Tissue deformation and bone damage for both needle insertion and extraction at moderate insertion velocity (10mm/sec)

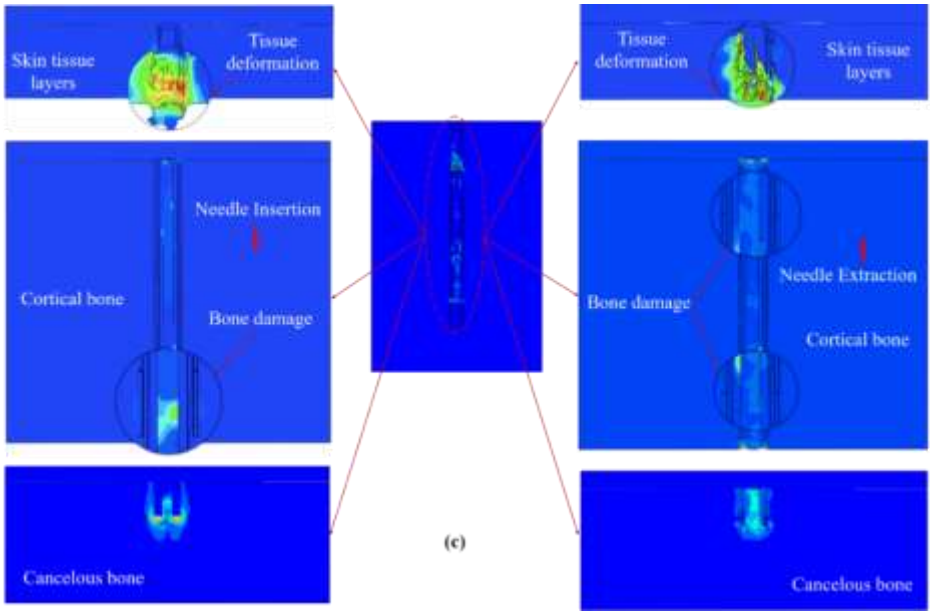

Figure 4.23: Tissue deformation and bone damage for both needle insertion and extraction at maximum insertion velocity (20mm/sec)

Figures 4.24 and 4.25 provide a simulation-based comparison of needle contact stress in the y-z plane's cross-sectional surface for various insertion and extraction procedures using different conventional and barbed biopsy needles. The maximum contact stress appeared to move along the shaft from the needle tip during insertion following a puncture with conventional and barbed biopsy needles. The maximum contact stresses observed by conventional and barbed biopsy needles during insertion along the entire skin-bone domain have been 131 MPa and 127 MPa, respectively, as illustrated in Figure 4.24. Similarly, according to Fig. 4.25, the maximum contact stress values encountered during the entire extraction of conventional and barbed biopsy needles in the skin-bone domain have been 103.33 MPa and 100.43 MPa, respectively. The variation in shear stress distribution across each model affects the geometry and tip shape of the needle. The maximum shear stress has consistently been found in close proximity to the tip of the needle across all time scales and conditions.

4.4.6 Needle deflection during insertion

The amount of needle deflection is directly associated with the needle tip's bevel angle, the needle shaft's composition, the iliac crest, and the friction forces between the surface of the needle and the surrounding tissue. Variation of the needle deflection with the distance along the needle for different insertion velocities has been shown in Figure 4.26 for different combinations of α_1 and α_2. It has been observed that by modifying the barb designs, the deflection of the bioinspired barbed biopsy needles might be altered (refer to Figure 4.26) and possibly adjusted easily. Adding barbs on the needle surface reduces the deflection of the needle. According to the findings of FE modeling using various insertion velocities and barb shapes, the average deflection of the bioinspired barbed biopsy needles has been 4.33 mm. The results of the FE analysis have demonstrated that adopting a biopsy needle with barbs drastically reduces the deflection by 40.6% on average while using a barbed biopsy needle with $\alpha_1 = 170^{\circ}$ compared to 157° for an insertion depth of 53 mm. However, the maximum deflection of the bioinspired barbed biopsy needle (6.26 mm) has been 50% less compared to the traditional bevel needle (10.44 mm) [141]. It can be construed that the deflection of the bioinspired BMB needles (refer to Figure 4.26) might be altered by altering the barb shapes. As a result, the bioinspired barbed biopsy needle may potentially follow a straightforward path (without much needle path deviation), making it easier to regulate for relatively high precision.

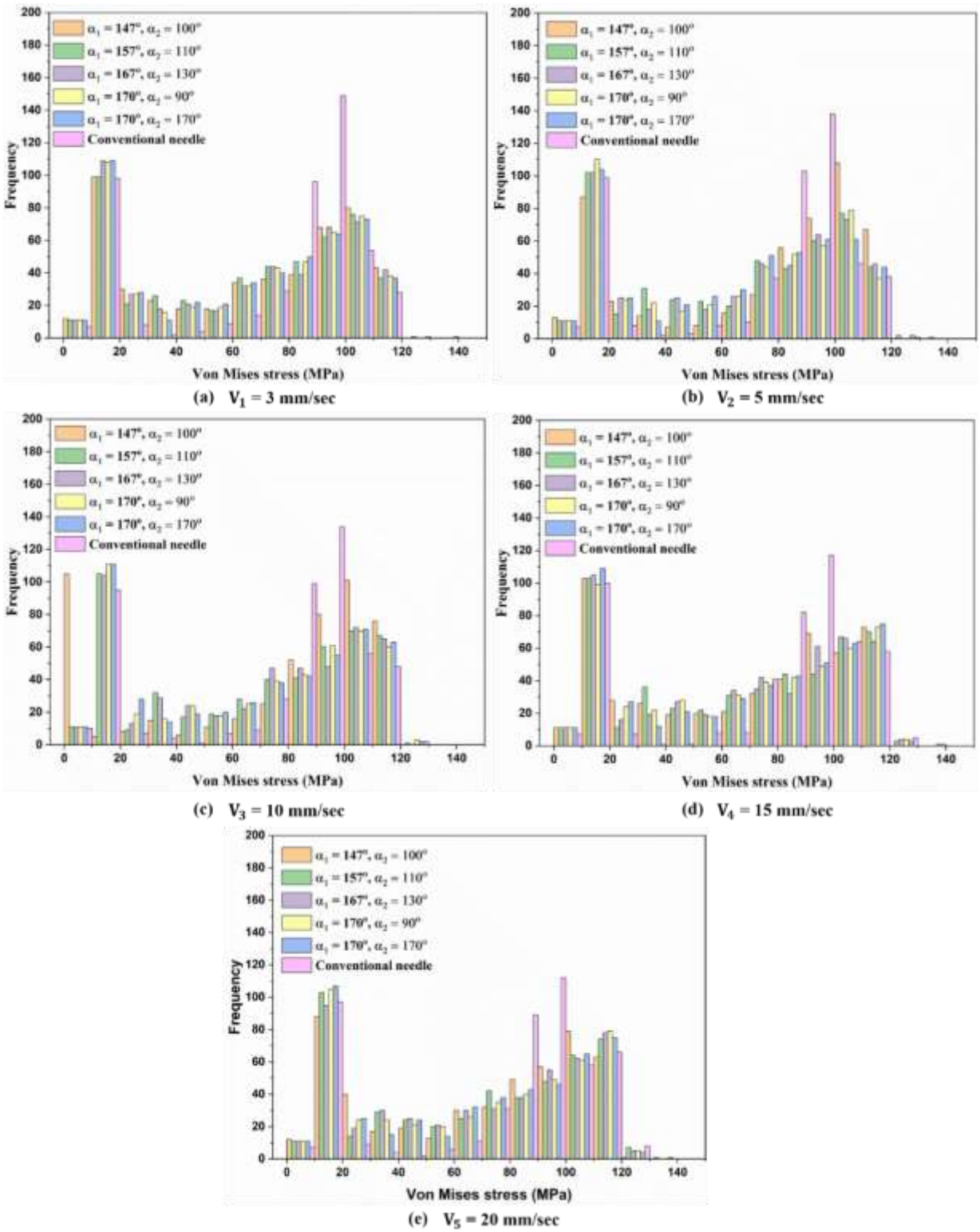

Figure 4.24: Contact stresses on the needle and skin-bone tissue layers interactions from needle insertion simulation with various values of insertion velocities.

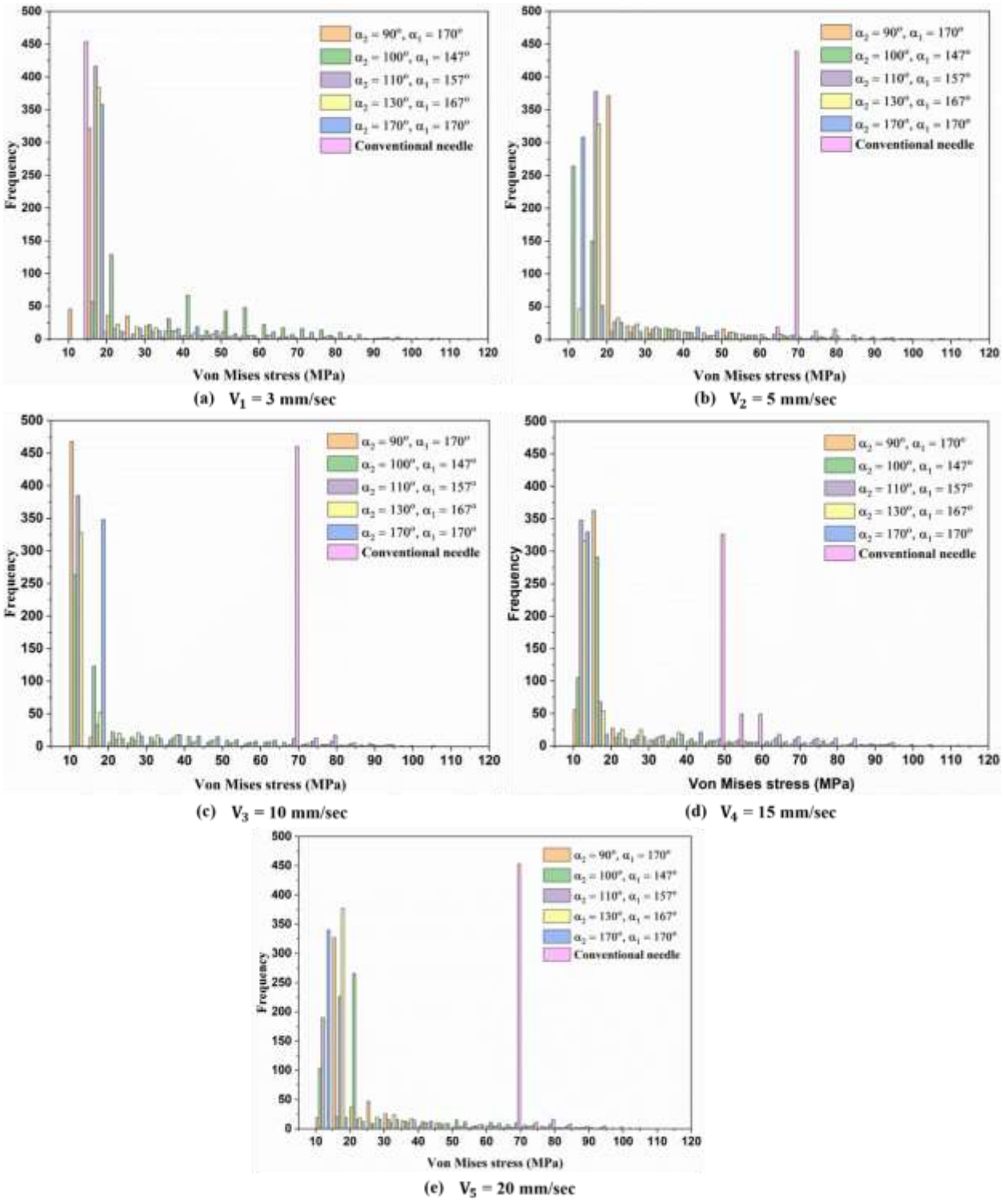

Figure 4.25: Contact stresses on the needle and skin-bone tissue layers interactions from needle extraction simulation with various values of extraction velocities.

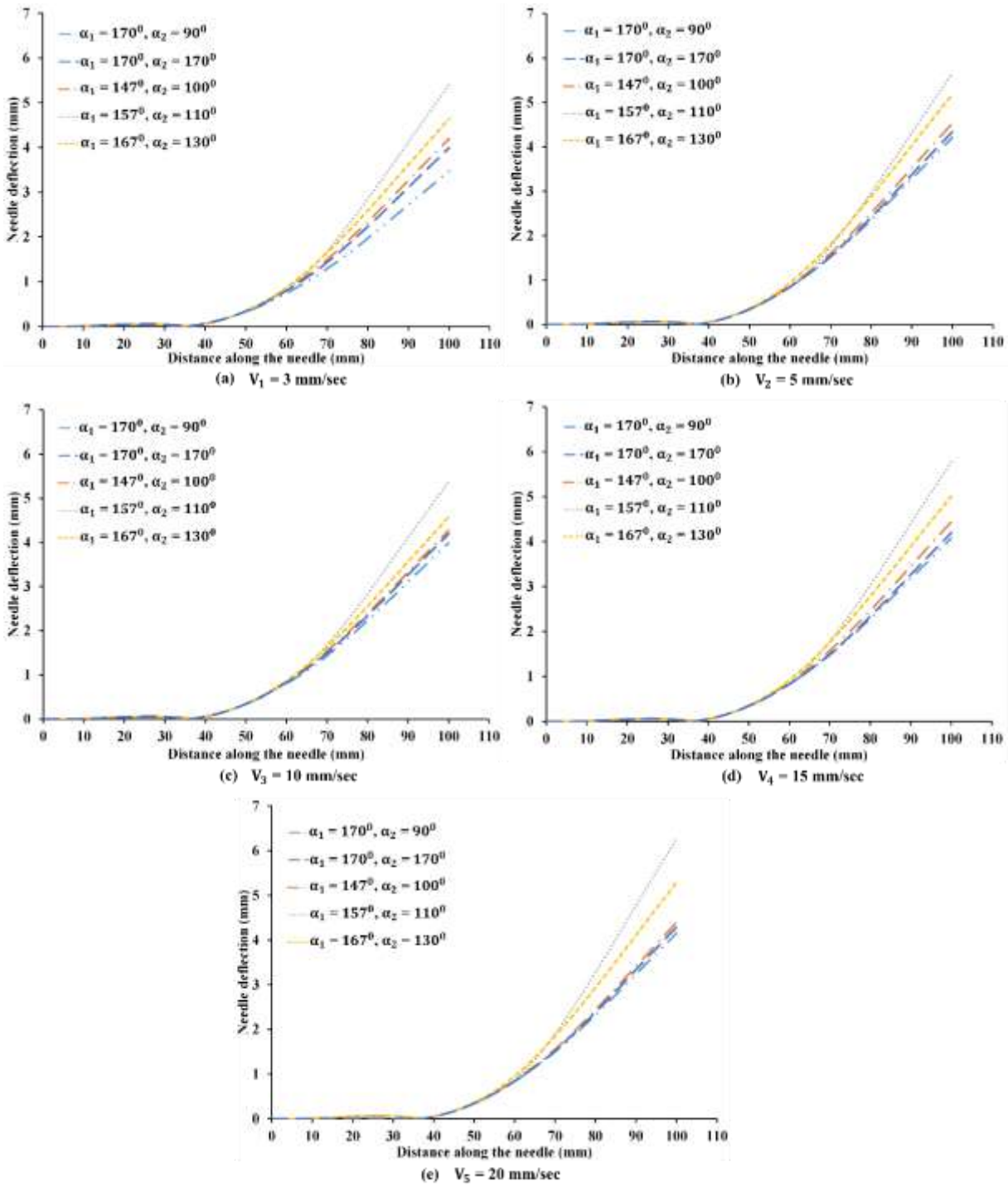

Figure 4.26: Variation of the needle deflection with the distance along the needle for different insertion velocities

4.4.7 Discussion

The study involved the creation of a 3D finite element analysis model, which used the Lagrangian surface-based method to simulate the insertion of a hollow barbed biopsy needle, based on a honeybee stinger, into a multilayered iliac crest model. This study aimed to establish a computational FE technique that might enhance understanding of the interaction between the needle and tissue. The ultimate objective is to optimize the design of hollow barbed biopsy needles to overcome the drawbacks of present hollow needle designs. The study primarily examined the forces involved in the interaction between the needle tip and shaft as they penetrate the tissue. In the present study, five-needle types have been considered, and each type has been studied for five insertions corresponding to 25 insertion/extraction tests. All FEM tests have measured the insertion and extraction forces, bone damage, needle deflection, tissue deformation, and frictional forces in the iliac crest model. It is anticipated that the friction force of the needle must be reduced to lower the insertion and extraction forces because it contributes most to the overall insertion force. This hypothesis will be examined and analyzed in this study.

Further, the extraction force of the needle is a significant consideration while incorporating barbs on the shaft. It has been assumed that the barbs will not increase the extraction force [80]. A numerical analysis has been carried out to confirm this assumption. With less or no typical forces occurring on the body, the needle trajectory within the tissue can be modulated more efficiently. The study demonstrated that the proposed honeybee-inspired needles efficiently lower the insertion and extraction forces. This reduction is attributed to the decreased surface area of the needle, which reduces friction. The study includes determining the design parameters of the barbs and studying their effect on the needle insertion and extraction procedures. The study examined the effect of α_1 on the insertion force and determined that the needle with $\alpha_1 = 170^{\circ}$ had the lowest insertion force. A needle with a modified barb design resulted in 49.39% reduction in the insertion force compared to a conventional bevel tip needle at 10 mm insertion depth in skin tissue layers. In bone tissue layers, use of barbed needle resulted in an average decrease of 28.32% in the insertion force once anchored into the bone and penetrated further compared to a conventional bevel tip needle. A higher α_1 means higher material removal from the biopsy needle and hence lower insertion forces. A biopsy needle with a large insertion force causes more skin-bone tissue destruction. Reduced deformation improves the capacity of the biopsy needle to obtain biopsy samples of higher quality and quantity [142]. The patient may experience lesser discomfort throughout the procedure if the cutting force is lowered. After analyzing both the insertion and extraction forces, α_2 values have been varied, and it can be seen from Figures 4.16-4.18 that, $\alpha_2 = 170^{\circ}$ resulted in the lowest insertion and extraction force values. When the biopsy needle is removed, the resistance force gradually decreases. Further, it is evident that multiple layers of the iliac crest experiencing the compressive state during insertion experience the tensile state during extraction. Since skin-bone tissue layers and the needle

simultaneously moved backward when the needle has been withdrawn, the friction force reported within that section has been the static friction force. The extraction force got reduced to zero when the needle has been extracted from the tissue in the final phase of the FE simulation. This is due to the fact that the coefficient of kinetic friction remained constant when the needle length within various iliac crest layers is reduced. Barbs have been generated on the outer periphery of the needle in the present model, which reduces the needle extraction force due to a reduction in the frictional area between the skin-bone tissue and the needle.

The maximum stress occurred at the barbed biopsy needle tip area with the highest value of 20 MPa during needle insertion into the skin; as the tip progresses, the stress at the bone has been reported to be 133.5 MPa. Inserting a needle into the bone with varying barbed geometries and insertion velocities occasionally results in damage in the form of a fracture of the cortical bone around the needle. However, no or minor bone damage has been documented while employing the current design of barbed biopsy needles with any insertion velocity or shape. Stress distribution at the barbs is expected to decrease distortion of the iliac crest tissue completely around the needle shaft, resulting in a lower insertion force. The barbs separate the contact area between the needle shaft and the layers of the iliac crest, reducing the friction and the insertion force. As a result, the barbs on the biopsy needle shaft are expected to reduce the penetration force in the skin-bone domain. Figures 4.21-4.23 depict the tissue deformation and bone damage during different insertion velocities (3 mm/sec to 20 mm/sec) using various barbed biopsy needle specifications. As the layers of skin-bone tissue rupture, the strain reveals the severity of the tissue deformation. Since the maximal stress of the needle tip has been more significant than the yield stress of skin-bone tissue, the tissue might get cut. The skin-bone tissue deforms when a barbed biopsy needle enters at a specific velocity. The lesser the overall strain, the smaller the tissue deformation and the bone damage, as shown in Figures 4.21-4.23. As the insertion velocity increases, the strain value closer to the skin-bone tissue increases, which causes more skin-bone tissue rupture. The study suggests that contact stress, which refers to the contact pressure caused by the stick-slip effect of friction on the needle shaft, might be a critical parameter for analyzing the interaction of needles with diverse biological tissues and examining different barbed parameters of needles. The simulation outcomes can potentially be utilized as an in silico pre-operative surgical planning tool for procedures requiring precise needle targeting, such as BMB and brachytherapy, to anticipate needle deflection, insertion force, and contact stress distribution during needle insertion.

4.4.8 Limitations and perspectives

Numerous problems in the design of barbed biopsy needles still need to be addressed in future studies. Firstly, the barbed biopsy needles have been considered rigid structures because their stiffness

values are several orders higher than the substrate stiffness values. Actual validation of the modeling approach is complex since it needs the availability of fresh human skin. Furthermore, the author has not considered needle rotation in this study. The suggested model can be modified to incorporate additional properties such as needle vibration, torque and strain-rate sensitivity. Including these factors is not a part of this study due to space restrictions. Exceptionally rigid barbed biopsy needles, with sharp needle tips, significant aspect ratio, and various barb parameters, like the one represented here, come close to a 'perfect scenario' situation regarding decreasing biopsy needle penetration force and optimizing penetration performance. The outcomes of this research establish the foundation for the design of complex bioinspired biopsy needle designs, which are essential for a better comprehension of the complex process of skin-bone tissue and biopsy needle interaction during the biopsy operation. These simulations could accelerate the design and development of actual BMB equipment, minimizing the number of tests and pain.

4.5 FE Analysis of Bio-inspired BMB Needle Using Honeybee Stinger-Inspired Hollow Needle: A Parametric Study (Study 5)

Minimally invasive biopsy needles are frequently inserted into the desired body regions during the BMB procedure. Various authors have conducted studies on soft tissue using solid/non-hollow bio-inspired needles to investigate aspects such as insertion/extraction, tissue deflection, and damage. However, these studies may have limited informativeness since a hollow needle is typically required for performing biopsies. The key problem with needle insertion in tissues is that the insertion force damages the tissue and deviates the needle path, leading the needle to miss the desired target and reducing biopsy sample integrity. To address these shortcomings, this study developed a unique bioinspired barbed biopsy needle design that reduces insertion/extraction forces and needle deflection. The insertion/extraction studies have been carried out with a hollow barbed biopsy needle into a multilayer skin-bone tissue domain. Reducing the friction force of the needle is expected to lower the insertion and extraction forces, as it is the main contributor to the overall insertion force. An analysis using several bioinspired parameters (such as α_1, α_2, h, L_b) has been performed to determine the suitable design for the BMB procedure and the bioinspired needle's maximum insertion and extraction forces.

4.5.1 Results and Discussion

The needle insertion procedure is categorized as follows: pre-puncture, insertion, post-puncture, and extraction. Figure 4.27 depicts the force-time data collected during 5 mm/s computational needle insertion, puncture, and extraction into the iliac crest model. The needle endures small and large punctures as it penetrates deeper into the skin-bone tissue and passes through internal tissues throughout the needle insertion process. As a result, during needle insertion, the force of the needle will increase and decrease,

respectively. The needle force rises linearly throughout the insertion after the puncture occurs due to increased friction between skin-bone tissue and the needle shaft (refer to Figure 4.27). The needle tip experiences cutting force during the insertion phase. In contrast, the needle shaft encounters changing frictional force as it advances, owing to increased contact area with tissue. In order to increase biopsy efficacy, the authors have concentrated on measuring the insertion/extraction force and deflection during needle insertion/extraction into the skin-bone tissue, with varying barb characteristics provided on the periphery of the needle.

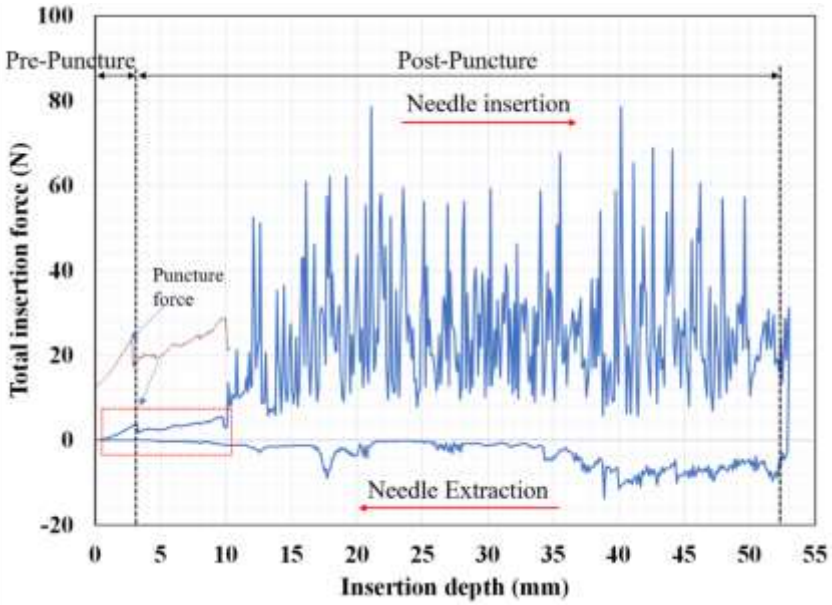

Figure 4.27: Typical needle-tissue force curve for insertion/extraction force with a depth of 53 mm and velocity of 5 mm/sec

4.5.2 Barbed front angle influence on insertion force

The insertion forces of a bioinspired needle have been measured by varying α_1 while keeping α_2 constant at 90°. Figure 4.28 depicts the average insertion forces acquired from five evaluations of bioinspired barbed biopsy needles with h = 0.5 mm, L_b = 45 mm for different values of α_1. As α_1 of a bioinspired biopsy needle is increased, the maximum insertion force decreases. The study on the variation of α_1 demonstrated that the needle with $\alpha_1 = 170^{\circ}$ angle had significantly lower maximum force than needles with 137°, 147°, 157°, and 167° angles. Moreover, increasing the barb angle reduced the maximum insertion forces, demonstrating that removing excess material from the needle reduces frictional and insertion forces. The frictional surface of the needle is reduced as the front angle increases, and this drop is not dependent on the values of other parameters; therefore, it could not be the overall minimum. Any combination of additional parameters (α_1, h, L_b) might show the trend found in this series of studies. When

a barbed needle with α_1 = 170° has been employed, insertion forces have been lowered by 44.4% on average at a depth of 53 mm.

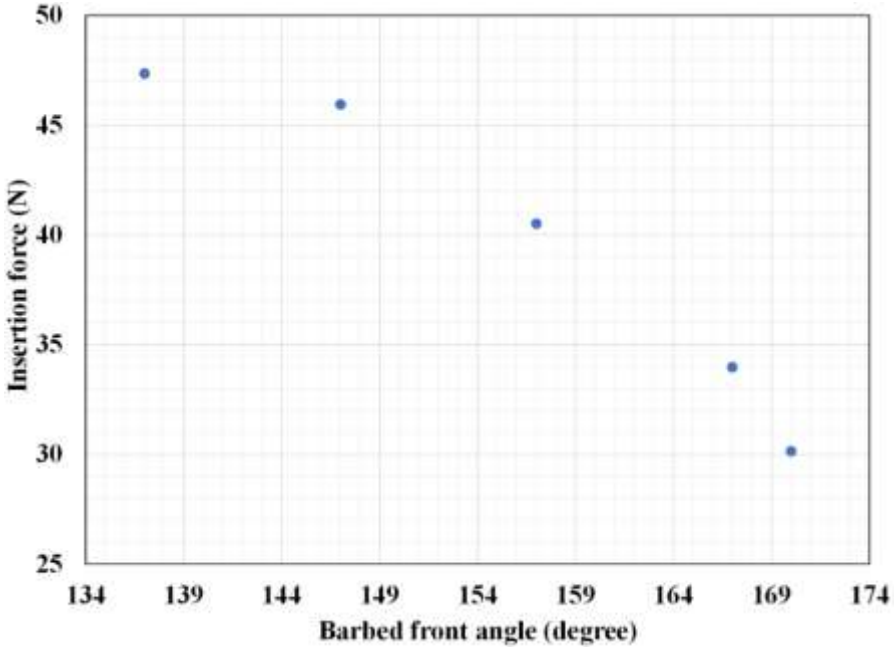

Figure 4.28: Influence of different α_1 on insertion force of bioinspired barbed biopsy needle with α_2 = 90°, h = 0.5 mm, and L_b = 45 mm

4.5.3 Barbed back angle influence on extraction force

The extraction force of a barbed needle is influenced by the α_2, which is a critical factor due to concerns about high extraction force. The extraction begins immediately following the insertion at a depth of 53 mm. The extraction forces for the bioinspired needle have been evaluated with various α_2 and a fixed α_1 of 170°. Figure 4.29 depicts the average insertion forces acquired from five evaluations of bioinspired barbed biopsy needles with α_1 = 170°, h = 0.5 mm, L_b = 45 mm for different α_2. When a barbed needle with α_2 = 90° has been employed, insertion forces decreased by 53.5% on average at a depth of 53 mm with the beveled needle tip. When a barbed needle with α_2 = 90° has been inserted into the skin-bone region, the tissue around it travels across adjacent barbs without filling the gap between them. As a result, the contact area between the needle and the tissue reduces considerably, along with the friction force. The present design incorporates the barbs on the periphery of the needle, reducing the frictional region between the needle and the skin-bone tissue domain and lowering the needle's extraction force. The extraction force values acquired for barbed biopsy needles with various α_2 are close to one another, indicating that the change in the extraction force with α_2 is minimal.

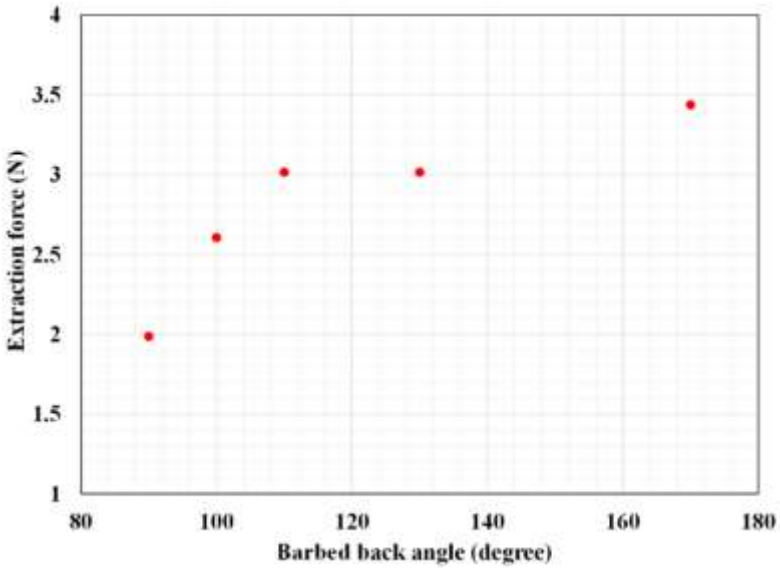

Figure 4.29: Influence of different values of α_2 on extraction force of bioinspired barbed biopsy needle with α_1 = 170°, h = 0.5 mm, and L_b = 45 mm

4.5.4 Barbed height influence on insertion force

To examine the effect of the h parameter, insertion simulations have been carried out using a multilayered skin-bone domain. Reducing frictional force by removing the excess material due to larger barb height reduces insertion forces. The average insertion force for barbed biopsy needles with various values of h has been shown in Figure 4.30, where α_1 = 170°, α_2 = 90° and L_b = 45 mm.

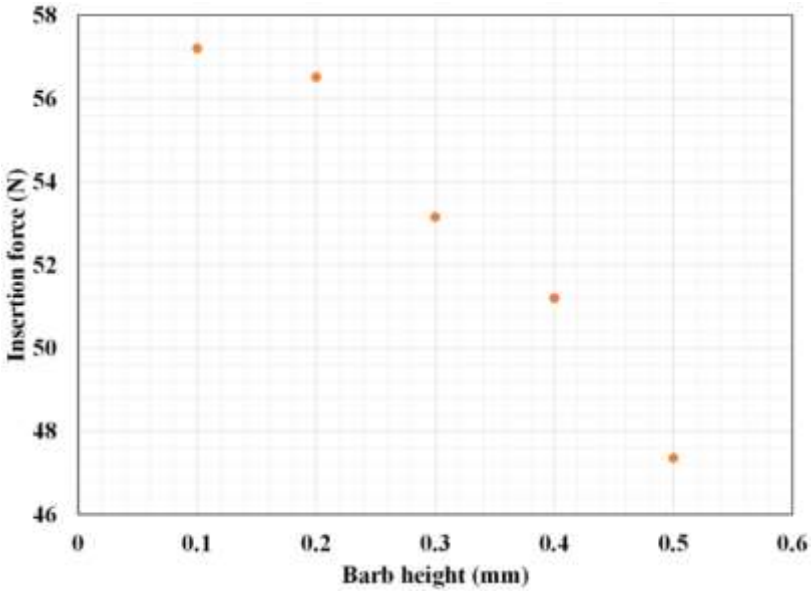

Figure 4.30: Influence of different values of h on insertion force of bioinspired barbed biopsy needle with α_1 = 170°, α_2 = 90°, and L_b = 45 mm

The statistical analysis has revealed a substantial variance in the insertion forces for different h values, with 0.5 mm step size having the lowest average insertion force of 47.35 N compared to the other h values. On average, the insertion force has been lowered by 18.8% when using a barbed biopsy needle with an h of 0.5 mm. Selecting a suitable h can enable attaining sufficient needle insertion force and bending stiffness concurrently by analyzing the influence of h on needle insertion force and identifying the trade-off with bending stiffness.

4.5.5 Barbed proportional length influence on insertion force

In this section, the effect of L_b on needle insertion force has been presented. Based on the needle shape evaluation, a new parameter for L_b has been created to minimize the insertion force slightly. Figure 4.31 demonstrates the influence of L_b on insertion force for barbed biopsy needles with $\alpha_1 = 170^\circ$, $\alpha_2 = 90^\circ$ and h = 0.5 mm. The maximum insertion force for the barbed biopsy needle with L_b = 25 mm has been reported as about 42.15 N for the insertion depth of 53 mm. Further, it can be seen that the insertion force for the needle with L_b = 30 mm got reduced by 5.0% and by 16.4% for the biopsy needles with L_b = 35 mm. Similarly, the insertion force got reduced by 33.4% when L_b is 40 mm and 38.3% when L_b is 45 mm.

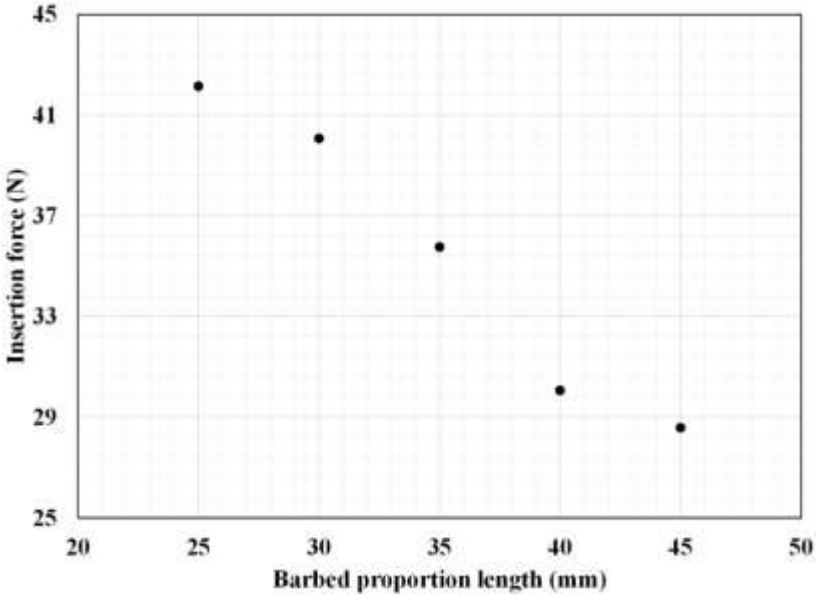

Figure 4.31: Influence of different values of L_b on insertion force of bioinspired barbed biopsy needle with $\alpha_1 = 170^\circ$, $\alpha_2 = 90^\circ$, and h = 0.5 mm.

4.5.6 Stress in skin and bone tissues

A stress path is a curved line that follows the principal stress direction at each point along its length. It has also been noted that the defects already present in the region where stresses approach the maximum

tensile value would lead to tissue and bone cracks deformations. The tissue may become damaged or distorted because the stress concentration on the barbed biopsy needle tip is larger than the yield stress of the tissue. Soft tissue deformation and bone fracture are substantially associated with patient discomfort. Since there is less tension on the skin and bone, the patient has less discomfort throughout the procedure. After the biopsy needle is removed from the skin-bone tissue interface, the tension during that interaction immediately decreases. The input parameters of the barbed biopsy needle may be applied to evaluate these forces when the needle penetrates the skin and bone tissue. The tissue first deforms under the advancing tip when the barbed biopsy needle tip contacts the top layer of the skin until substantial stress results in penetration into the skin. Penetration got initiated with a high-stress concentration in a comparatively small area constrained around the cutting needle (refer to Figure 4.32(a)). The presence of jammed barbs in the extraction process depicted in Figure 4.32(b) has caused tissue stickiness, resulting in tissue deformation. According to Figure 4.32, stresses around the needle tip have been maximum and rapidly decreased as evaluated away from it.

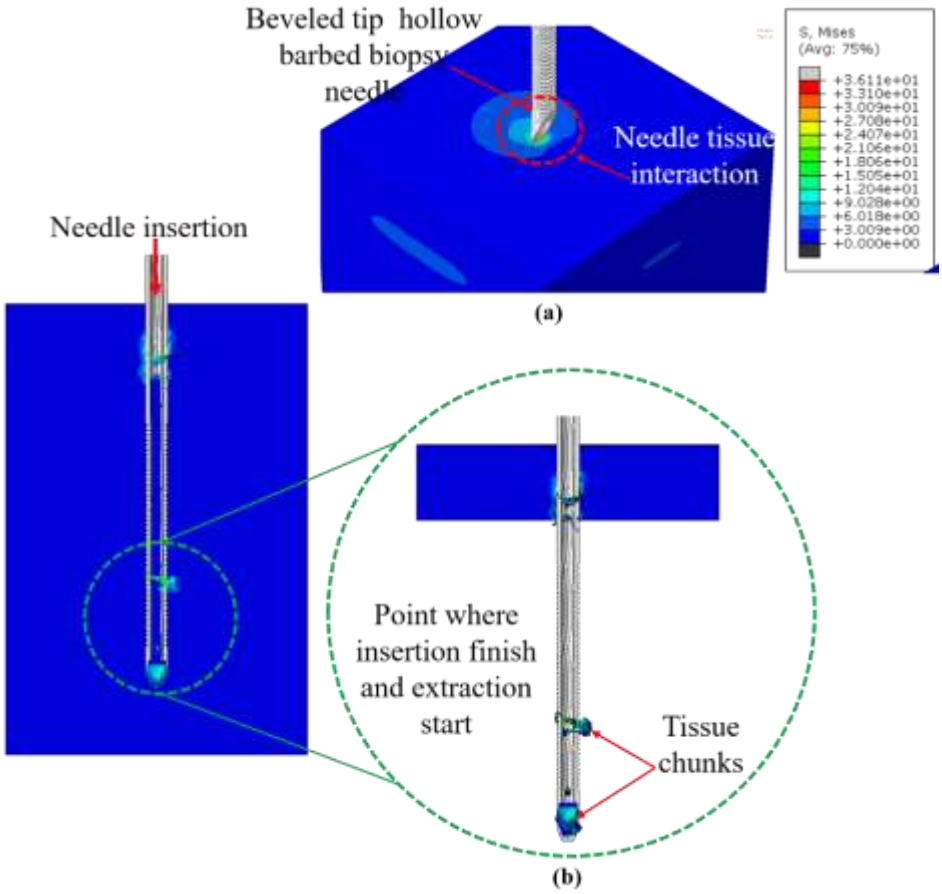

Figure 4.32: Simulation results of (a) stress distribution at the needle tissue interaction zone and (b) close-up view of the needle insertion/extraction process

Figure 4.33 demonstrates the contours of the maximum stress obtained during the numerical study of needle insertion into the skin-bone domain. The tissue may get cut because the maximum stress on the needle tip is greater than the yield stress of skin-bone tissue. The skin-bone tissue deforms when a barbed biopsy needle penetrates at a given velocity. Each layer of the tissue deforms into a concave shape as the biopsy needle advances through the skin-bone tissue domain, following the tip of the needle until it approaches the cortical bone. It has been anticipated that the stress distribution at the barbs would decrease the necessity for significant deformation of the iliac crest tissue surrounding the needle shaft. This, in turn, would lead to a reduction in the required insertion force. Barbs reduce friction and insertion force by separating the contact region between the multiple layers of the iliac crest and the needle shaft. The barbs on the biopsy needle decrease the force required to penetrate the skin and bone area. The stress concentration during the extraction process is shown in Figure 4.34. Once the needle has been extracted, the compression state of the skin quickly shifts to a tensile state.

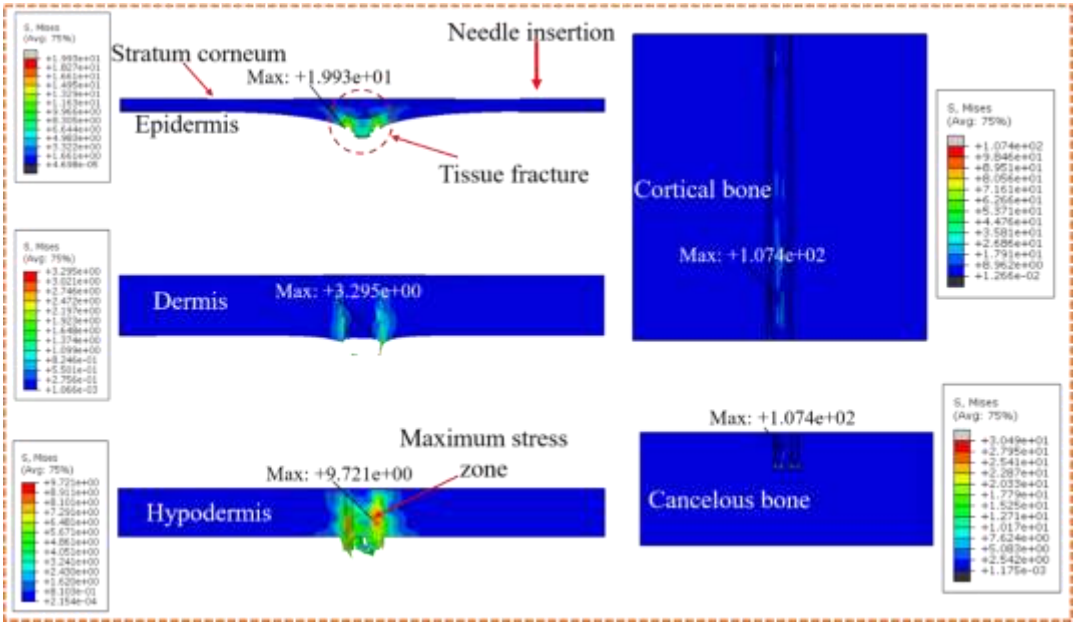

Figure 4.33: Stress distribution on the skin-bone domain during the needle insertion

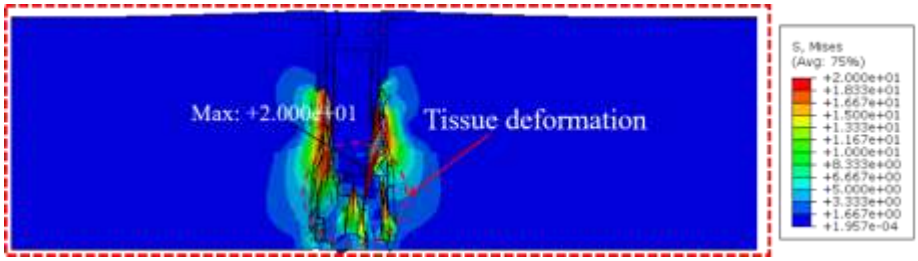

Figure 4.34: Stress distribution on the skin-bone domain during the needle extraction

4.5.7 Needle deflection

A 3D computer model based on Lagrangian surface-based non-linear FE technique has been utilized to simulate the insertion forces and deflection of a bevel-tipped hollow barbed biopsy needle into the skin-bone tissue. Figure 4.35 depicts the relationship between the needle deflection and the distance along the needle as a function of α_1 and α_2, at a velocity of 5 mm/sec. The study reported that by modifying the barb designs, the deflection of bioinspired barbed biopsy needles might be readily altered and adjusted, as shown in Figure 4.35. According to FE modeling results, the average maximum deflection of bioinspired barbed biopsy needles is 4.62 mm when various barb geometry parameters have been considered. The results from FE analysis indicate that using a barbed biopsy needle reduces deflection by an average of 28.28%, and a needle with α_1= 170° compared to 167° at an insertion depth of 53 mm has been more effective in reducing deflection. The barbs on the biopsy needle produce frictional forces with the surrounding tissue that assists in needle stabilization and reduces deflection during insertion, leading to decreased deflection with a barbed biopsy needle.

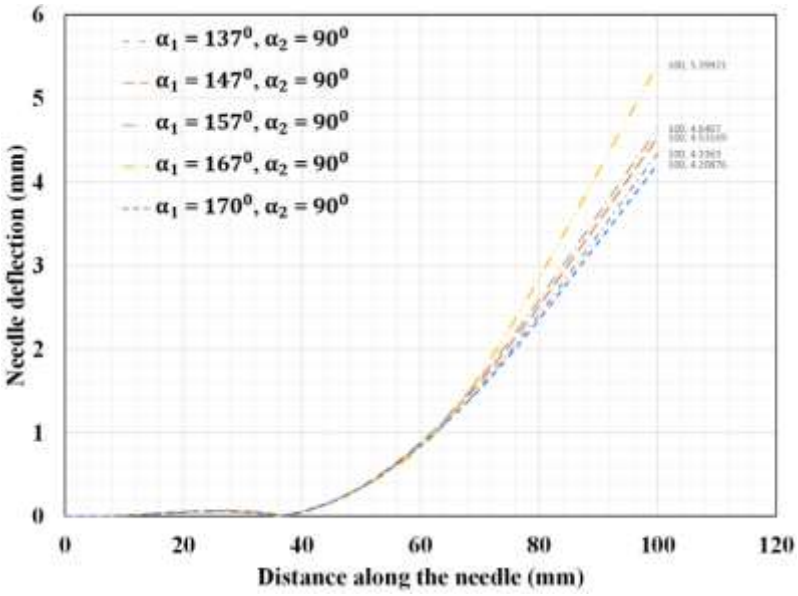

Figure 4.35: Representation of needle deflection vs. distance along the needle for different α_1

4.6 In-silico Analysis of Optimal Configurations for Rotational Bio-inspired BMB needle designs: An ANN Approach (Study 6)

Medical needle innovations have utilized rotating motion to enhance tissue-cutting capabilities, reducing cutting force and improving clinical outcomes. However, no studies have been performed to investigate the cutting motion used during BMB procedures, in which a hollow needle is inserted at a depth ranging from 10 to 60 mm while being rotated. In case of moderate penetration or rotation speed, the current

understanding of the cutting process with a rotating needle is limited. It would be essential to determine if the benefit of minimum cutting force can continue to be sustained, particularly when a more prominent core needle is used, such as in vacuum-assisted biopsy. Numerical simulation is a low-cost method for studying the cutting force in different needle velocity combinations with varying rotational orientations. These computer simulations can be used by authors to thoroughly study the number of variables and determine the best-barbed design of a bioinspired BMB needle. This study analyzes the effects of six essential factors on insertion and extraction forces during BMB procedures. The study uses Taguchi's L32 orthogonal array and numerically simulates the BMB process using the Lagrangian surface-based method on a three-dimensional (3-D) heterogeneous Finite Element (FE) model of the human iliac crest. The study evaluates cutting forces in needle insertion and extraction using unidirectional (360° rotation) and bidirectional (180°clock and anti-clock rotation) bioinspired BMB needles. This work aims at creating an AI tool that assists researchers and clinicians in selecting the most suitable and safe design parameters for a bio-inspired barbed biopsy needle. An efficient Graphical User Interface (GUI) has been developed for easy use and seamless interaction with the AI tool.

4.6.1 Results

The studies comprise insertion/extraction of a hollow barbed biopsy needle into a tissue domain comprising multiple layers of skin and bone. The needle penetration process has been divided into distinct phases: pre-puncture, insertion, post-puncture, and extraction. Figures 4.36(a) and (b) illustrate the collected force data patterns during computational needle insertion, puncture, and extraction into the iliac crest (skin-bone tissue) model for both bidirectional and unidirectional rotations. The needle undergoes small and large punctures throughout the insertion process as it progressively penetrates deeper into the skin-bone tissue and travers's internal tissues. Consequently, the force exerted by the needle during insertion will exhibit fluctuations characterized by rises and falls. The increased friction between the skin-bone tissue and the needle shaft causes an increase in the needle force s linearly after the puncture and continue to increase throughout the insertion procedure (refer to Figures 4.36(a) and (b)). During the insertion phase, the needle tip encounters a cutting force, while the needle shaft experiences varying frictional forces due to increased contact area with the tissue.

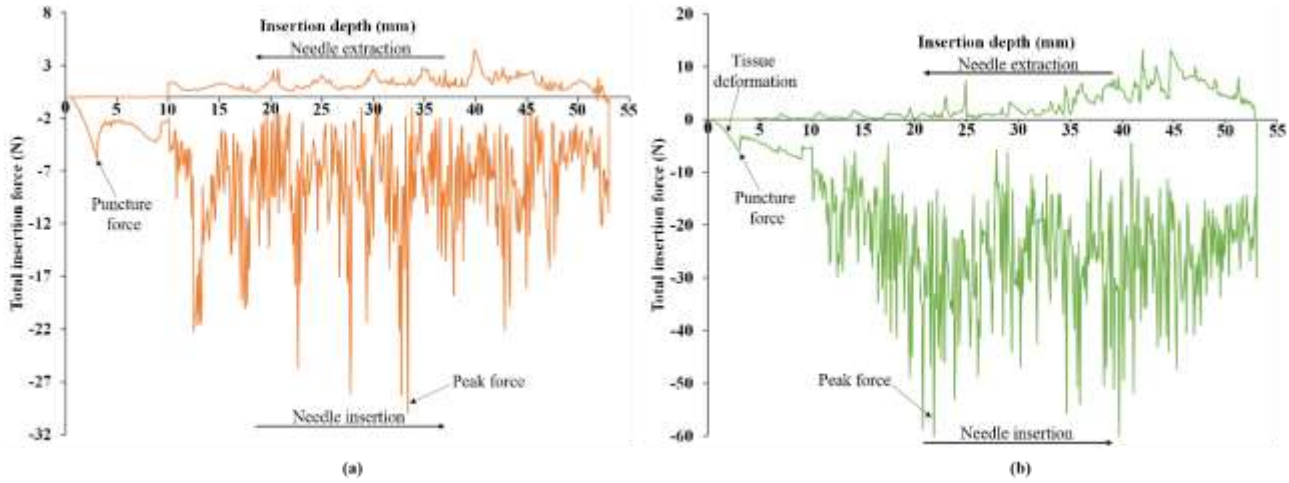

Figure 4.36: A characteristic force curve depicting the interaction between the needle and tissue during insertion/extraction at a depth of 53 mm with (a) bidirectional or (b) unidirectional rotation

4.6.1.1 Needle insertion force measurement

The measurement of insertion forces has been conducted by employing a bioinspired needle with varying values of α_1, and the forces have been recorded for both unidirectional and bidirectional rotations. Figure 4.37 illustrates the average insertion forces obtained from Taguchi's L32 orthogonal array trials (16 with unidirectional rotation and 16 with bidirectional rotation), which examined the effects of different input parameters on bioinspired needles with varying values of α_1. The observed data for skin-bone tissue layers shown in Figures 4.37 (a and b) demonstrates a substantial decrease in the insertion force when using different barbed needles. As the barb front angle increases, there is a corresponding decrease in the maximum insertion force. While comparing the different barb front angles, it has been observed that the needle rotating in a bidirectional direction with α_1 = 170°, h_b= 0.4 and L_{bs} = 30 exhibited a significantly lower insertion force than the needles having angles 147°, 157° and 167°, respectively. Furthermore, increasing the barb angle in conjunction with the bidirectional rotating direction decreases the maximum insertion forces. This observation suggests that removing excess material from the needle decreases frictional forces, resulting in lower insertion forces. For depths ranging from 0 to 10 mm, which corresponds to the layers of skin tissue, the average insertion force at a bidirectional rotation speed of v_r = 3.33 radian/time and v_i = 5 mm/sec has been 1.55 N, whereas the insertion force for unidirectional rotation has been observed to be 1.85 N. Similar patterns have been observed in this context, with depths ranging from 10 to 53 mm corresponding to bone tissue layers. The average insertion force at a bidirectional rotation speed of v_r = 3.33 radian/time and v_i = 5 mm/sec has been 10.58 N, whereas the insertion force for unidirectional rotation has been observed to be 22.67 N. These findings indicate a reduction of 17.64% (skin tissue layers) and 72.72% (bone tissue layers) in the average insertion forces for bidirectional rotation as compared to unidirectional rotation.

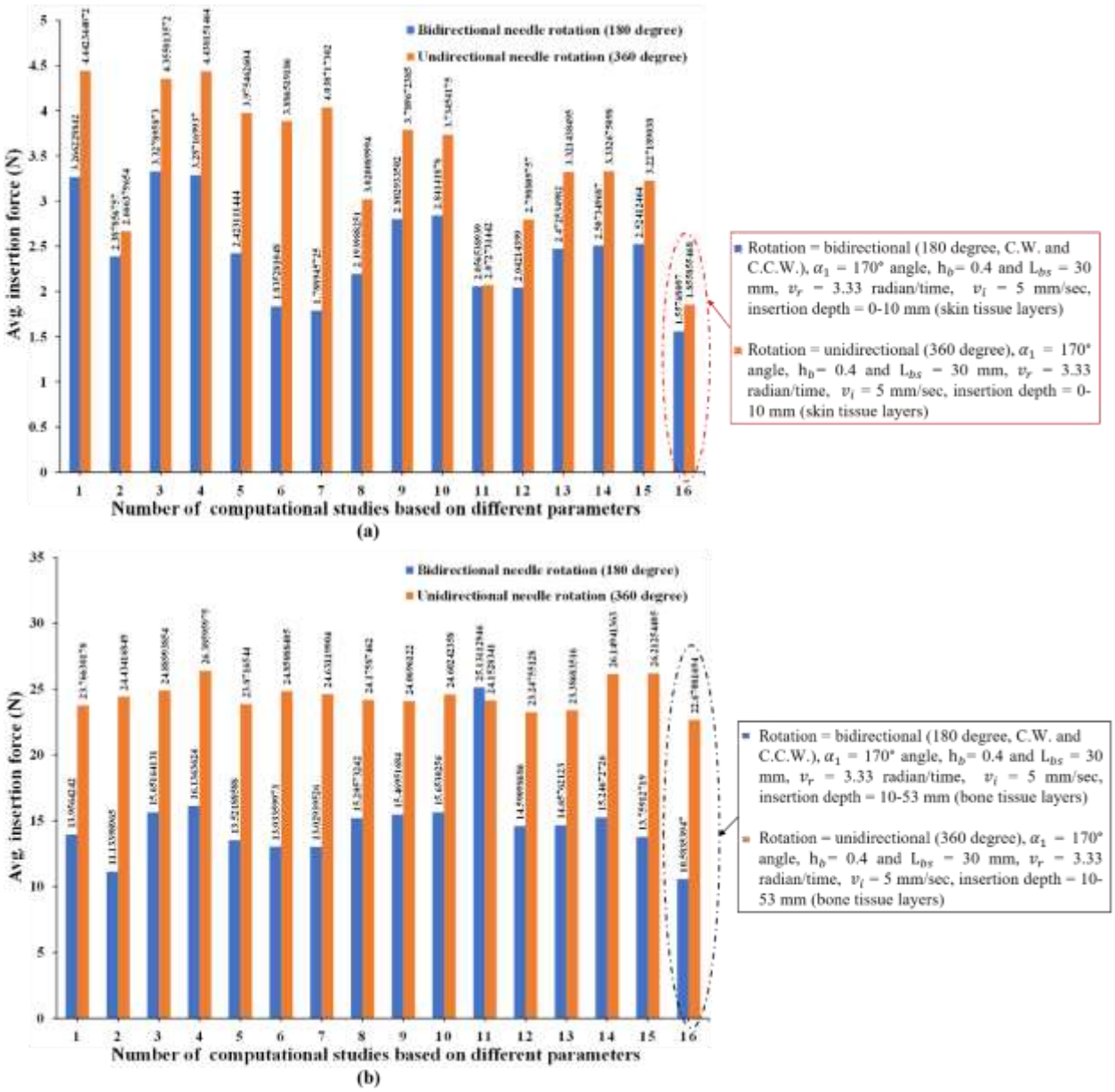

Figure 4.37: Barbed biopsy needle insertion force data for (a) skin tissue layers and (b) bone tissue layers at different Taguchi-based input parameter settings with unidirectional and bidirectional rotations

4.6.1.2 Needle extraction force measurement

Extraction forces have been measured using a bioinspired needle with different values of α_2, and the forces have been documented for both unidirectional and bidirectional rotations. The mean extraction forces acquired from Taguchi's L32 orthogonal array experiments have been shown in Figure 4.38. These trials encompassed 16 instances of unidirectional rotations and 16 instances of bidirectional rotations, allowing for an assessment of the impact of different input parameters on bioinspired needles with varying α_2 values. Considering the high extraction force associated with the utilization of barbs in the needle design,

it is crucial to recognize the significance of the impact of α_2 on the extraction force of the needle. The utilization of a bidirectional rotation barbed needle resulted in a substantial reduction in the extraction force compared to the use of a unidirectional rotation barbed needle (refer to Figure 4.38). While comparing different α_2 values, it has been observed that the needle rotating in a bidirectional direction with α_2 = 90°, h_b= 0.2 and L_{bs} = 35 exhibited a significantly lower extraction force than needles with angles of 110°, 130°, and 170°, respectively. For extraction depths ranging from 53 to 0 mm, which corresponds to the bone-skin tissue layers, the average extraction force at a bidirectional rotation speed of v_r = 3.33 radian/time and v_i = 5 mm/sec has been 0.606 N, whereas the extraction force for unidirectional rotation has been observed to be 1.215 N. The results suggest a significant decrease in the average extraction force to the extent of 66.88% (skin-bone tissue layers) for bidirectional rotation compared to unidirectional rotation, specifically for the skin-bone tissue layers.

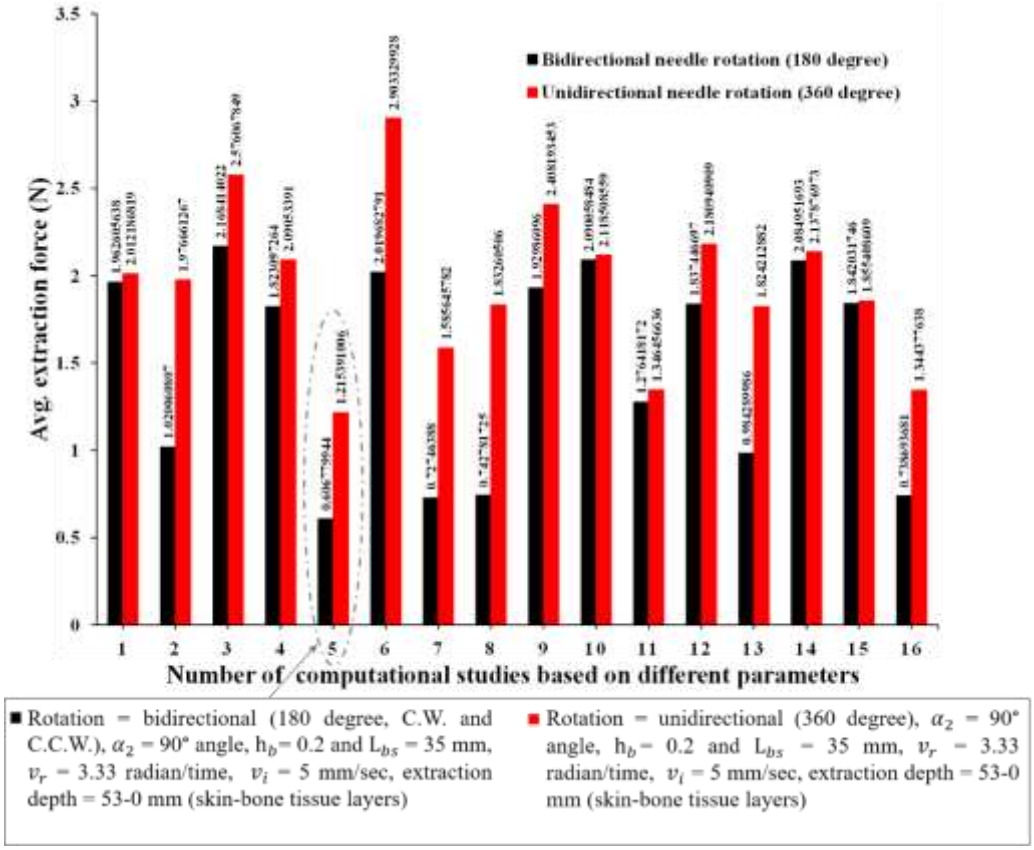

Figure 4.38: Barbed biopsy needle extraction force data for skin-bone tissue layers at different Taguchi-based input parameter settings with unidirectional and bidirectional rotations

4.6.1.3 Tissue damage for rotated insertions/extractions

Figures 4.39 and 4.40 present a comparative analysis of the tissue damage occurred during insertion/extraction procedure by a barbed biopsy needle rotating at both unidirectional and bidirectional

speeds. The tissue is susceptible to being cut if the highest stresses applied to the needle tip exceeds the yield stress range of biological skin-bone tissue. The entrance of the biopsy needle at a particular velocity and rotation induces biological skin-bone tissue deformation. Fracture behavior in skin-bone tissue has been observed once the stress value exceeds the fracture stress threshold of the tissue. The range of stress exhibited during the initial phase of fracture behavior in the tissue can be used to estimate the severity of damage to biological skin-bone tissue. The contour plots of the highest primary stress in biological skin-bone tissue under two distinct rotating directions can be seen in Figures. 4.39 and 4.40. There is a direct relationship between the amount of stress and the level of tissue damage, wherein lower stress values indicate less tissue damage. Following the puncture, it has been observed that the maximum contact stress progressively moved along the shaft of the needle from the tip throughout the insertion process, regardless of the direction of rotation and type of biopsy needle. During the needle penetration procedure, the initial peak of contact stresses at the puncture is 9.483 MPa for bidirectional rotation and 9.962 MPa for unidirectional rotation.

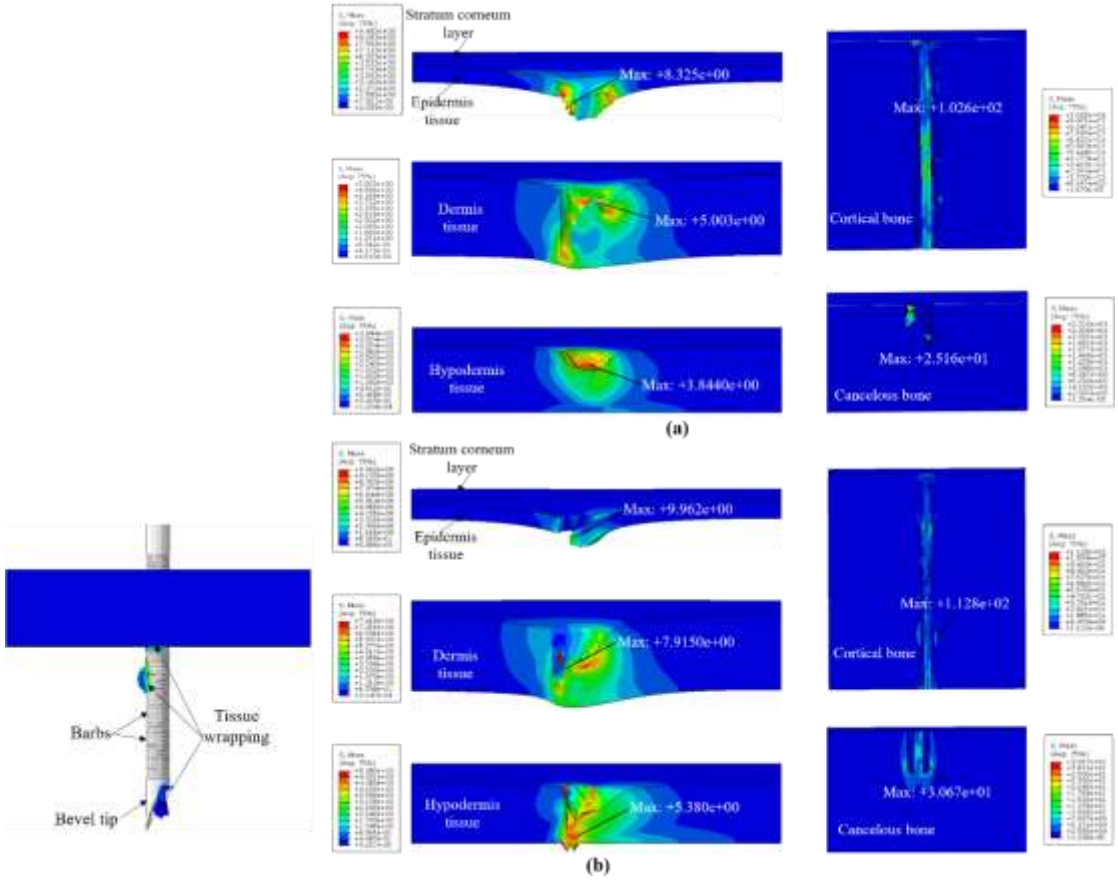

Figure 4.39: Stress distribution on the iliac crest (skin-bone domain) around the barbed biopsy needle during insertion at both unidirectional and bidirectional rotations

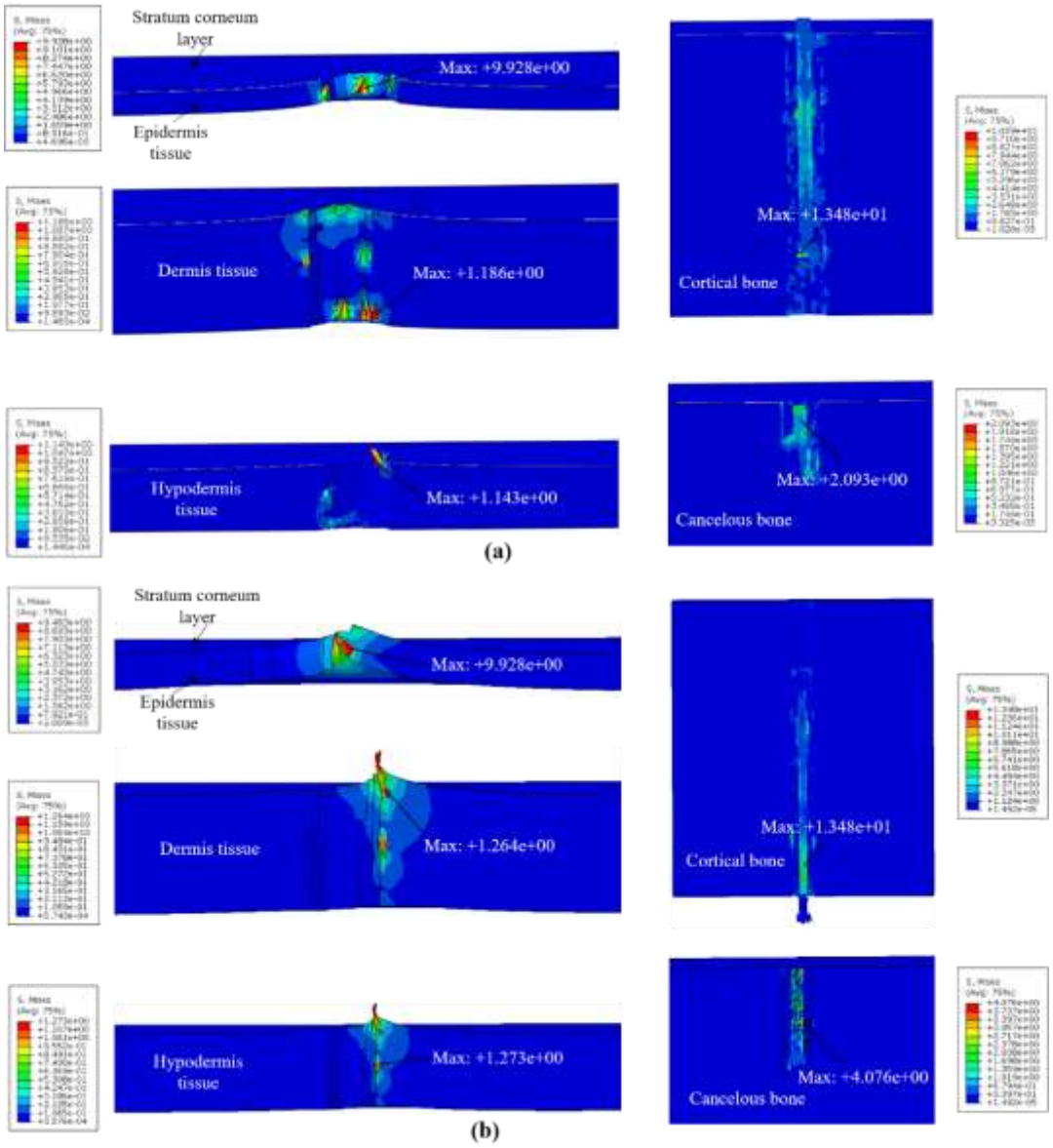

Figure 4.40: Stress distribution on the iliac crest (skin-bone domain) around the barbed biopsy needle during extraction at both unidirectional and bidirectional rotations

4.6.1.4 Needle deflection

The measurement of needle deflection has been conducted using a bioinspired biopsy needle, wherein various sets of input parameters (viz., α_1, α_2, h_b, L_{bs}, velocity) have been employed. The needle deflections have been recorded separately for both unidirectional and bidirectional rotation scenarios. The needle deflection plots obtained from Taguchi's L32 orthogonal array experiments have been shown in Figures 4.41(a) and (b), showcasing the measured deflection of the needle under different parameter combinations.

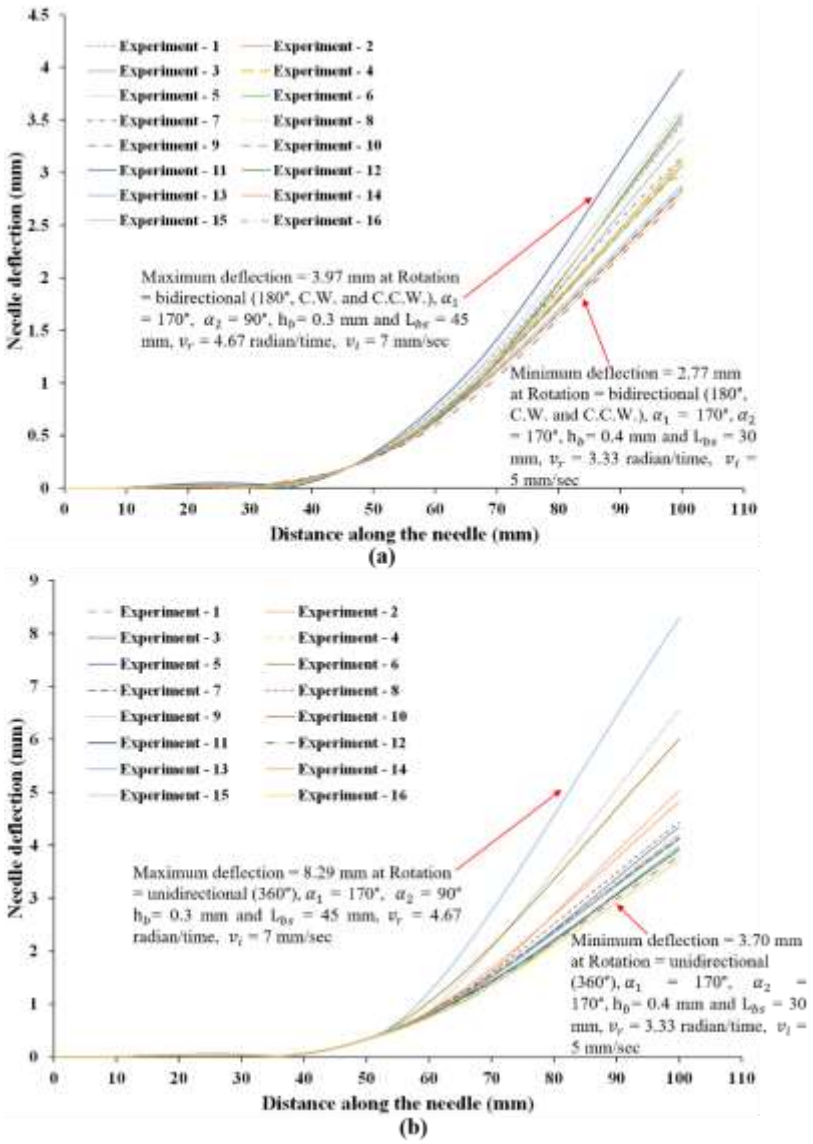

Figure 4.41: Evaluation of needle deflection between the result of unidirectional and bidirectional rotation at different Taguchi-based input parameter settings

The experimental trials include 16 instances each of unidirectional and bidirectional rotations, enabling an evaluation of how different input parameters impact bioinspired needle performance. Tissue wrapping plays a critical role in needle deflection during bioinspired biopsy needle insertion, regardless of whether the rotation is bidirectional or unidirectional. During the rotation of the needle, the adjacent tissue wraps around the needle shaft, resulting in the generation of frictional forces that impact the trajectory of the needle. At depths spanning from 0 to 53 mm, representing the layers of skin and bone (iliac crest) tissue, the maximum deflection observed during bioinspired BMB needle insertion has been 3.97 mm when using bidirectional rotation at a speed of v_r = 4.67 radian/time and v_i = 7 mm/sec. In contrast, the maximum

deflection reached 8.29 mm in case of unidirectional rotation. Similarly, for depths ranging from 0 to 53 mm, the minimum deflection during bioinspired biopsy needle insertion has been 2.77 mm when using bidirectional rotation at a speed of v_r = 3.33 radian/time and v_i = 5 mm/sec. In comparison, the minimum deflection reached 3.70 mm with unidirectional rotation. The results demonstrate a substantial reduction in maximum deflection to the extent of 70.47% and in minimum deflection to the extent of 28.74% during bioinspired biopsy needle deflection within the skin-bone tissue layers when utilizing bidirectional rotation, as compared to unidirectional rotation.

4.6.1.5 Analysis of ANN results

Ideally, the Root Mean Square Error (RMSE) should be minimized and kept below 10 for optimal performance [28, 29]. The analysis demonstrates remarkably low RMSE values for the measured parameters: 0.482 for insertion force, 0.064 for extraction force, 0.209 for deflection, and an outstandingly low 0.003 for torque. These values are significantly below the targeted threshold of 10. This information has been graphically presented in Figure 4.42, displaying the performance plot of the ANN model. Based on the data presented in Figure 4.42, it is evident that the model has achieved convergence at different epochs for each parameter: insertion force at epoch 287, extraction force at epoch 849, deflection at epoch 961, and torque at epoch 784. In this study, an epoch represents the number of iterations necessary for the model to reach convergence.

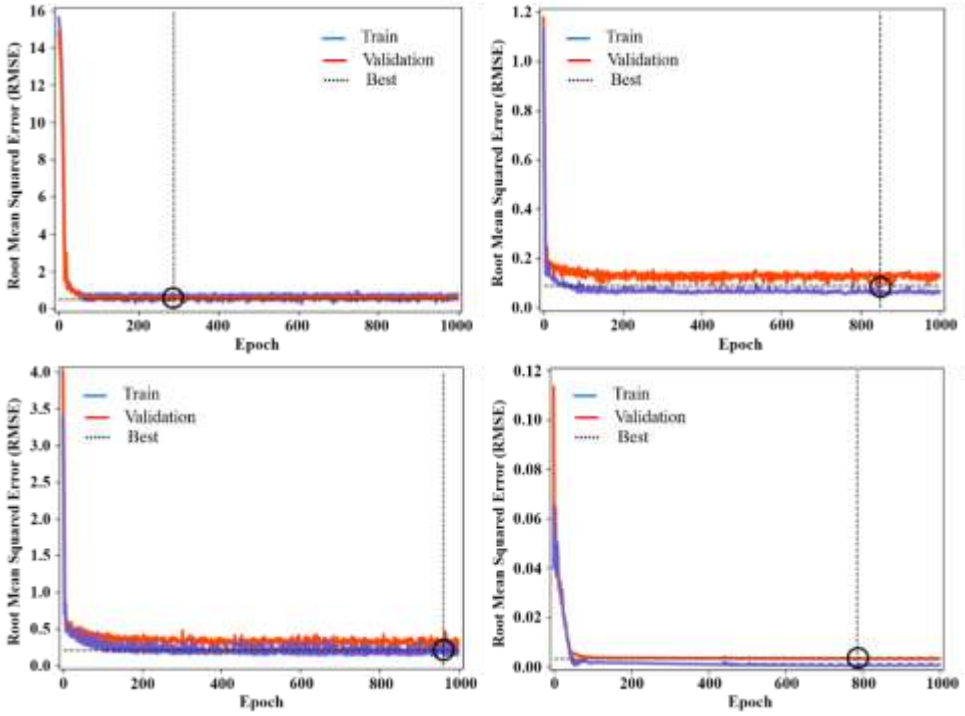

Figure 4.42: Performance plot of the proposed ANN model using six inputs showing RMSE trend during the learning phase

A linear regression analysis has been performed to validate the accuracy of the trained model. This analysis helps assess how well the model's predictions align with the actual data. Through the linear regression analysis, the study reveals the correlation between the predicted outputs of the model and the original outputs initially used for training the model. This analysis helps to evaluate the accuracy and effectiveness of the trained model's predictions. Figure 4.43(a-d) illustrates the training, validation, testing, and linear regression analysis of the trained network model. In Figure 4.43(a-d), the regression plot displays the predicted outputs along the vertical axis and aligns the target values (actual outputs) along the horizontal axis. The regression 'R' coefficient indicates the correlation between the expected and target values (i.e., actual output). The results demonstrate an optimum agreement between the expected results and the target values, with an overall R of 0.98 indicating a strong correlation between them. The ANN has been trained in an iterative method to minimize the MSE efficiency. The results demonstrate that employing fewer neurons in the hidden layer for ANN modeling accurately estimates all cases' insertion/extraction force, deflection, and torque. When comparing the test data to the expected insertion/extraction force, deflection, and torque data obtained from ANN, it is evident that the ANN's estimations exhibit a significant improvement.

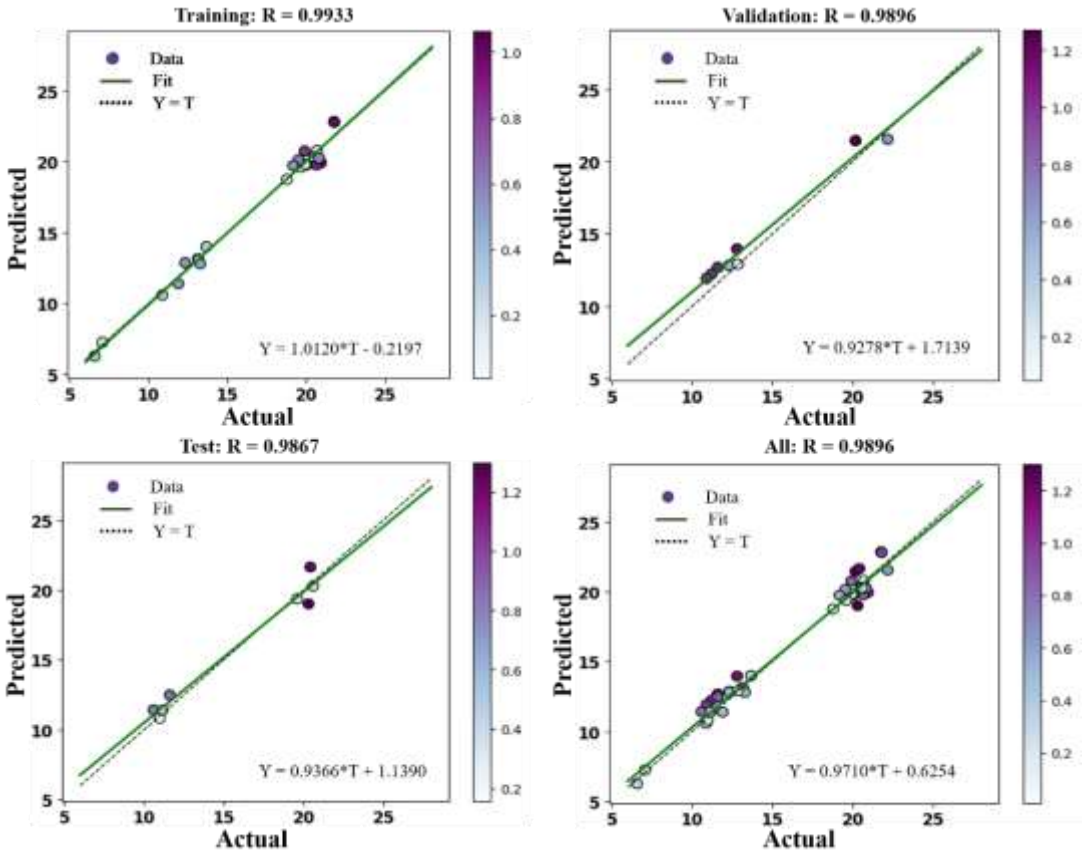

Figure 4.43(a). Neural network training regression analysis (optimal performance at 17 neurons in the hidden layer for insertion force).

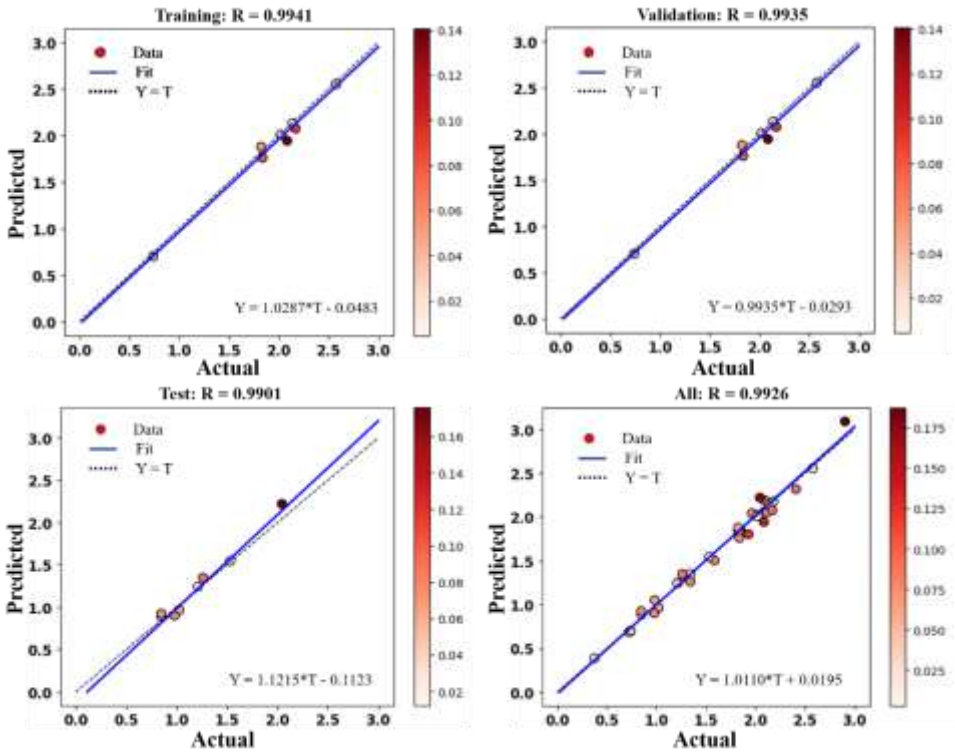

Figure 4.43(b): Neural network training regression analysis (Optimal performance at 17 neurons in the hidden layer for extraction force).

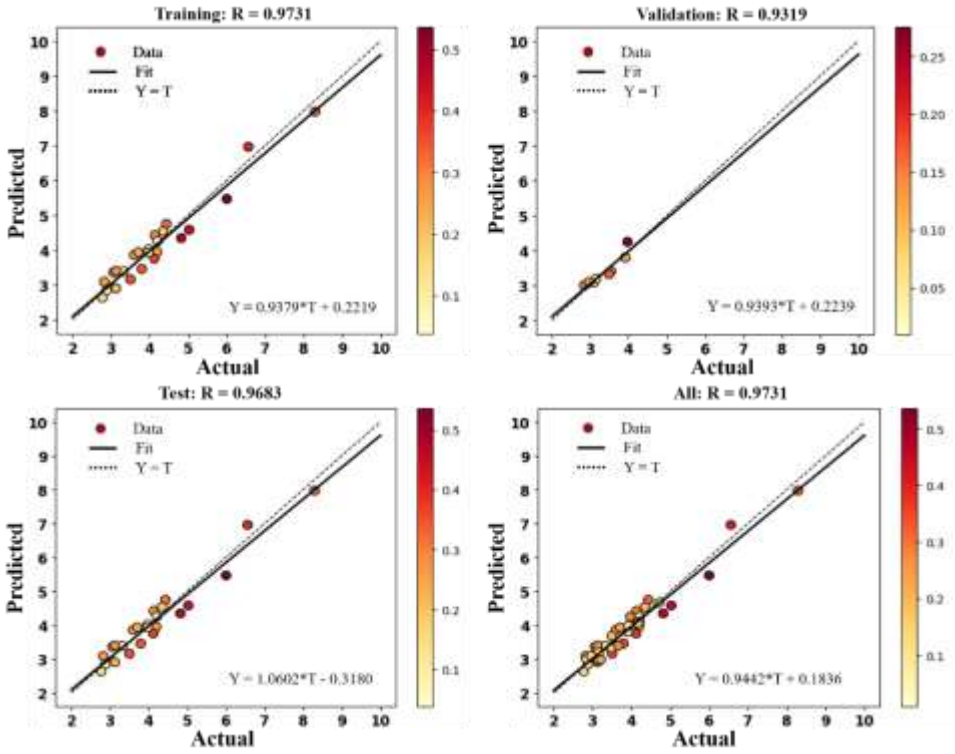

Figure 4.43(c): Neural network training regression analysis (Optimal performance at 17 neurons in the hidden layer for deflection).

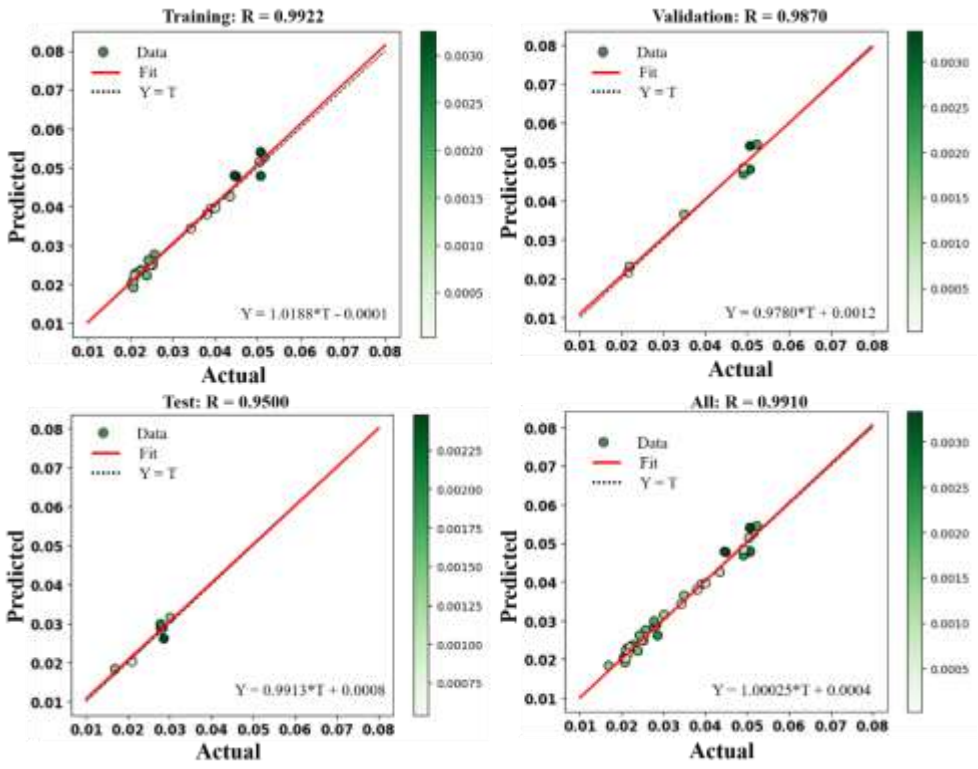

Figure 4.43(d): Neural network training regression analysis (Optimal performance at 17 neurons in the hidden layer for torque).

The main features of the dataset obtained from the FE simulation have been analyzed and summarized. These features are then visualized in a two-dimensional format using a heatmap, as shown in Figures 4.44(a-d). The seaborn heatmap has been utilized to identify the correlation between the output and input parameters in the dataset. This visualization technique helps to highlight the relationships and patterns between these variables. The data has been divided into two sections: names and features. The independent variables have been extracted and used as input features for the algorithm, while the dependent variable has been treated as the label or output variable. The Seaborn pair graph has been used to explore if there was a positive or negative association between specific areas. Fortunately, no irregularities have been found throughout this study. As illustrated in Figure 4.44, all the measured results fell within the range of -1 and +1. This indicates that the distribution and correlation among the various examined fields have been considered satisfactory. The observations reveal that light colors represent a negative correlation, whereas dark colors indicate a positive correlation between different features in the dataset.

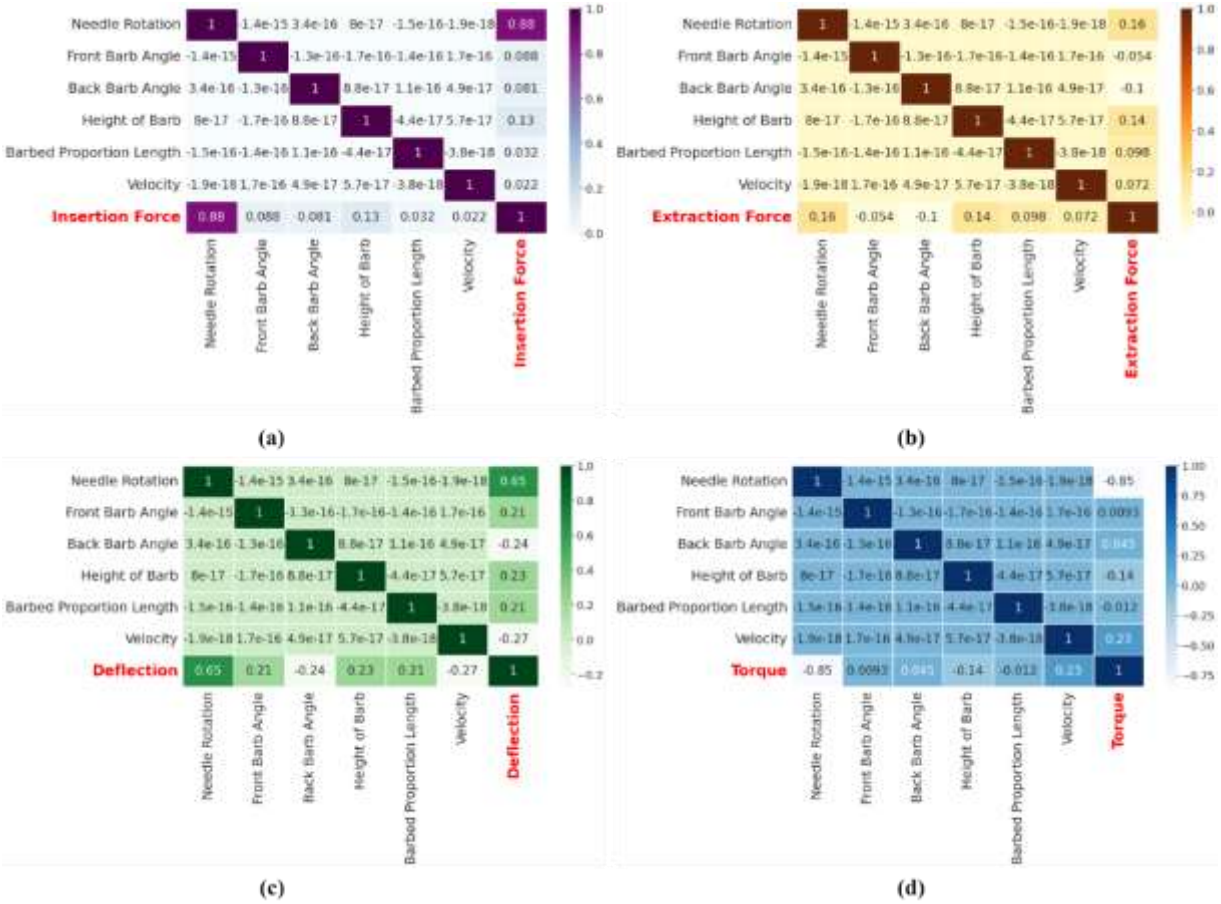

Figure 4.44: Seaborn heatmap to visualize the correlation among various input and output parameters viz. (a) insertion force, (b) extraction force, (c) deflection, and (d) torque of a barbed biopsy needle

4.6.1.6 Development of the GUI tool

The BInBioN graphical user interface (GUI) toolkit has been developed by integrating the ANN model with the "Tk Interface," i.e., the Tkinter library provided in Python 3. Tkinter contains a class called Tk which provides all the GUI components. In Python, the handles array has been passed to various callback functions. These callback functions have been primarily responsible for handling user interactions with the GUI of the tool, such as selecting a menu item or pressing a push button. The handles array allows the callback functions to access and manipulate GUI elements, facilitating seamless interaction between the end user and the graphical user interface. Figures 4.45(a) and (b) show a pictorial diagram that describes the GUI of the tool. The researchers and clinicians can utilize the GUI as an AI tool to calculate the needle's insertion/extraction force, deflection and torque effortlessly. They can achieve this by simply inputting the specific values of the barbed biopsy needle parameters into the interface.

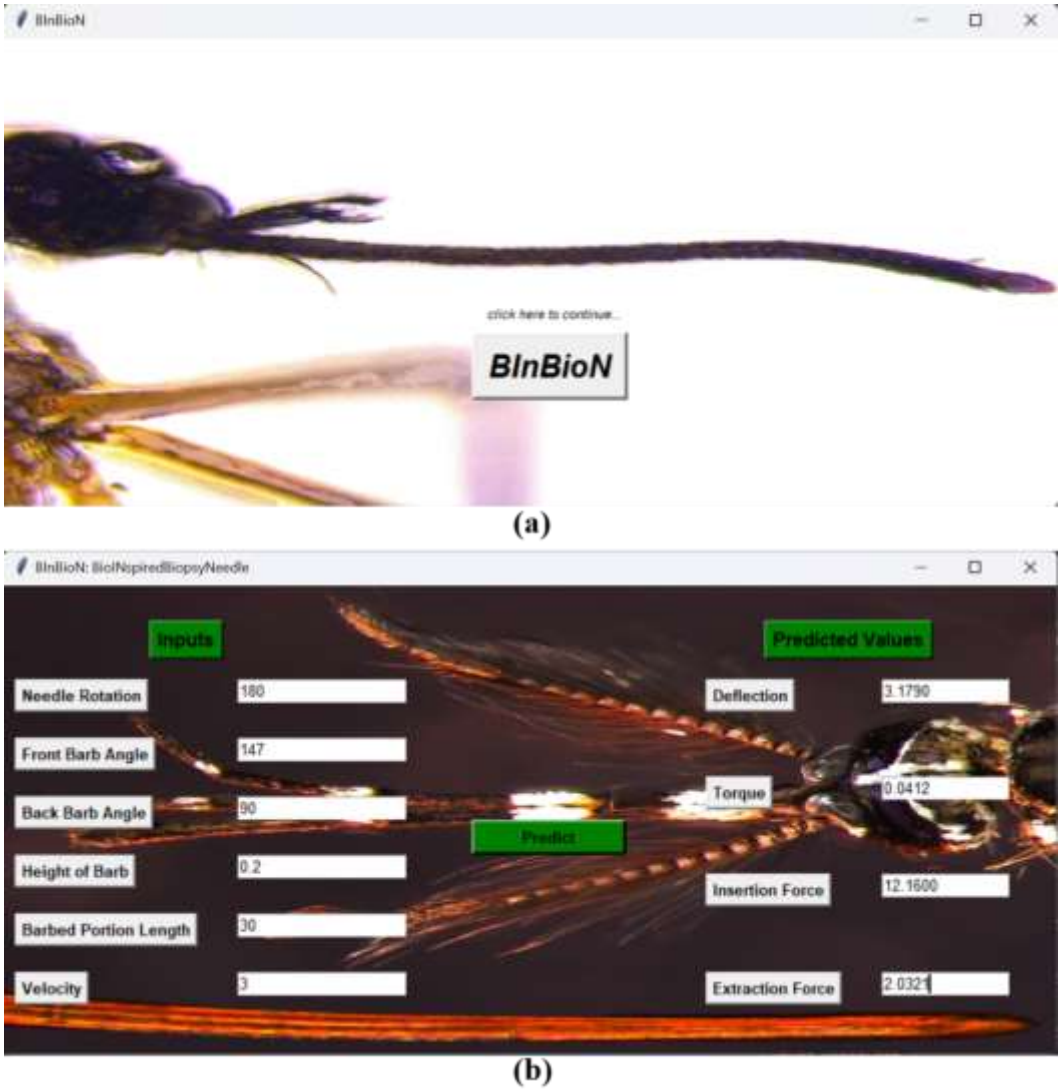

Figure 4.45: Pictorial representation of BInBioN application to determine optimal bio-inspired needle design

This user-friendly approach streamlines obtaining essential information for needle procedures, making it readily accessible and efficient for medical professionals. The step-by-step process of using the GUI tool has been depicted in Figure 4.45(a) for the front panel and Figure 4.45(b) for the back panel. These schematic representations outline the sequential approach that users can follow to interact with the GUI effectively. To achieve the desired results for biopsy needle design, designers must adhere to this sequential approach by inputting the relevant information of the biopsy needle into the corresponding box of the GUI tool. Following this step-by-step process, the GUI will provide the necessary calculations and outputs for designing an optimal biopsy needle.

4.6.1.7 Evaluation and effectiveness of the proposed tool

The suggested tool's assessment involves comparing its outcomes and those obtained from Abaqus software. The evaluation has been conducted through a dual approach, wherein the capabilities of the tool have been tested and verified in two distinct manners. Firstly, it assesses the effectiveness of the tool by examining the accuracy of the results it generates. Secondly, it compares the time efficiency of the tool with that of Abaqus software. Eight sets of input parameters at varying insertion velocities have been employed to verify the tool's effectiveness. The GUI of the tool receives each of these input data sets, which produces the relevant values for insertion/extraction force, deflection, and torque. The identical input datasets have been utilized in Abaqus, and subsequently, the obtained data for insertion/extraction force, deflection and torque values have been extracted. The percentage error between the outputs of the tool and Abaqus has been calculated, and is falling within the range of 1% to 3%. This level of error is considered satisfactory for an ANN model-based tool.

4.6.2 Discussion

The method in which the needle is inserted has been observed to impact the interaction between the needle and the tissue during the FE simulation process. In these studies, a comprehensive evaluation of the performance of bioinspired needles has been conducted by performing 16 instances of unidirectional rotation and 16 instances of bidirectional rotation. This allowed for an assessment of how different input parameters influenced the performance of the needles. By employing this approach, it became possible to analyze the impact of various combinations of parameters on the performance of the needles. Previous studies have also discovered two distinct phases during a typical needle insertion procedure [96, 66, 143]. During the initial phase, the needle deforms the tissue without cutting, and the forces exerted on the tissue increase as it deflects. In the subsequent phase, the needle consistently cuts through the tissue. In this phase, the forces acting on the needle include the cutting forces exerted at the needle tip and the friction forces generated between the needle shaft and the skin-bone tissue. The two phases mentioned above are distinguished by the occurrence of the puncture event, which is marked by a reduction in the insertion forces. Examining the force-displacement curve during needle insertion can readily identify this event. The results demonstrate a significant reduction in the average insertion force for bidirectional rotation compared to unidirectional rotation, with a decrease of 17.64% observed in skin tissue layers and a substantial decrease of 72.72% observed in bone tissue layers. There is compelling evidence indicating that rotating the needle, leading to a decrease in force, can enhance the accuracy of source placement by minimizing the tissue compression. The extraction procedure begins immediately after insertion at a depth of 53 mm. Use of bidirectional barbed biopsy needle results in a substantial decrease in the extraction force compared to the unidirectional barbed biopsy needle. The insertion forces of the needles with different α_2 values exhibit

minimal variation, indicating that the impact of α_2 on the insertion force is relatively small. This phenomenon occurs due to the creation of a larger gap space. When the barbed needle with α_2 = 90° penetrates the skin-bone tissue, the surrounding tissue shifts from one barb to the next without entering the gap between consecutive barbs. Consequently, this leads to a notable decrease in the contact surface area and the resulting friction force. The positive insertion force recorded in the data can be attributed to the resistance exerted by the deformed tissue, which pushes back against the needle throughout the insertion process (refer to Figure 4.36). As the needle is pulled back during the extraction, both the needle and the tissue move in a backward direction together. Consequently, the friction force measured during this phase corresponds to the static friction force. The extraction force steadily drops to zero in the last stage of the FE simulation as the length of the needle inside the tissue decreases due to the fixed coefficient of kinetic friction. Bidirectional rotation effectively minimizes tissue damage and achieves a satisfactory cutting effect during the operation. Simultaneously, it helps decrease cutting displacement and prevents tissue tearing. The location of maximal stress concentration within the stinger has been situated near the tip, where it reaches a peak value of 1.026e+02 MPa (refer to Figure 4.40). The forward movement of the tip results in an increase in stress on the top layer of the skin, making it susceptible to being cut away easily. After achieving the defined failure threshold of the skin's effective stress near the tip, the removal of dead skin mesh components produces node separation, allowing the stinger tip to penetrate the skin. Local stress concentrations at the barbs are believed to lower the necessity for deforming the whole circumference of skin-bone tissue surrounding the stinger, decreasing the insertion force. The compressed condition of the skin swiftly changes into a tensile state during stinger withdrawal [97]. Despite its potential benefits, enhanced needle accuracy may not yield favorable results for the patient if it leads to increased tissue damage, resulting in swelling and bleeding. The barbs remain unbent and undamaged when the stinger and its barbs have been observed as a rigid body, allowing the stinger to engage with the tissue through mechanical interlocking efficiently. The maximum forces and moments observed during needle insertion/extraction may be detected in the initial stage by running a simulation (using the extracted data from the Python script) that includes both skin-bone tissues. In this phase of the study, the needle has been selected as a rigid body, assuming no deflection takes place. In the next step, the maximum force and moment values determined earlier are employed to model the needle individually. This uses a deflection Python script that considers the needle's deformability and incorporates relevant stainless-steel properties. By incorporating the deformable nature of the needle and considering its steel properties in the modeling process, a more realistic evaluation of the needle's performance and potential impact on the surrounding tissues during insertion and extraction procedures is made possible. The results obtained for the needle deflection have been extracted and specifically presented for a length of 53 mm. This particular length has been selected as it corresponds to the penetration depth of the needle in the multi-layered skin-bone model.

The non-uniform distribution of tissue wrapping causes different frictional forces during unidirectional rotation, causing the needle to deflect along its path. The alternating clockwise and anticlockwise rotations during bidirectional rotation results in a balanced and consistent distribution of tissue wrapping around the needle. Frictional forces are created, which resist changes in motion. The uneven tissue wrapping observed during unidirectional rotation has been mitigated by employing bidirectional rotation. As a result, the precision and accuracy of the biopsy procedure are enhanced, leading to improved outcomes.

4.6.3 Limitations/perspectives and future work

Further investigations are required to tackle several issues concerning barbed biopsy needle design. The validation method for the modeling technique is difficult owing to the need for fresh human skin-bone samples. In addition, the study did not consider the inclusion of vibration-assisted rotation in barbed biopsy needle procedures. The results of this research provide a fundamental basis for designing intricate bioinspired biopsy needle configurations. Such designs enhance our understanding of the intricate interaction between skin-bone tissue and biopsy needles during biopsy procedures. A crucial aspect to consider in future studies would involve experimentally validating the honeybee stinger-based biopsy needle model. Biological studies, including the insertion and removal of the needle in multi-layered tissue specimens, might provide an in-depth understanding of its performance and effectiveness. Comparison of experimental results with computational model predictions may be helpful to assess the needle's reliability and applicability. This iterative procedure may result in further design refinement and development.

Page intentionally left blank

Chapter 5

Conclusions and Future Scopes

5.1 A prospective survey on trephine biopsy of bone and bone marrow

This study suggests patients should be well-informed and comfortable during the trephine BMB procedures to minimize pain. The posterior iliac crest has been recommended for the BMB procedure due to its larger marrow capacity. Local anesthesia with lidocaine or sedative drugs increased patient tolerance. Pain has been the major complication in both adult and pediatric patients, with 41 (14.96%) reporting no or minimal pain, 82 (29.92%) experiencing moderate pain, and 151 (55.1%) reporting intolerable pain. Premedication reduced anxiety in some patients, although complications have been observed in 5 (11.1%) of the 45 (16.4%) who received it. Bone texture affected the length of the bone marrow sample, with "fragility" and "very hard" texture resulting in shorter samples. "Very hard" bones also had more frequent needle bending and required more repetitions. Modern improvements to trephine biopsy needles with a triple-bevel needle to acquire the bone marrow sample are expected to decrease the pain during the procedure.

5.2 Modelling of conventional BMB needle insertion into the iliac crest

Optimization of the bone marrow biopsy needle diameter and its insertion velocity are essential to improve needle insertion and extraction procedures. This study has showed a numerical analysis of needle insertion and extraction forces involved in a multi-layer iliac crest model for bone marrow biopsy. The studied insertion and extraction forces have been associated with a penetration depth of 15.35 mm and insertion velocity rates of 1 mm/sec to 10 mm/sec. At the beginning of the needle insertion phase, a linear force vs. depth relationship has been recorded irrespective of the penetration depth. Despite that, as the insertion depth increased, the relationship between the force and the depth increased non-linearly. At the ending phase of the needle insertion, the force augmented rapidly, even at a small insertion velocity compared to the high insertion velocity. It has been found that the insertion and extraction forces vary according to the needle diameter and relative velocity among the needle and tissue layers. It has also been observed that the insertion and extraction forces of the conical-shaped needles in the multi-layered iliac crest model decreased by 18.92% and 37.5%, respectively, as the needle diameter reduced from 11G to 20G. At the insertion depth up to 15.35 mm, a maximum insertion force of 138 N has been observed for 10 mm/sec (i.e., high speed) experiments, approximately 1.15 times higher than 5 mm/sec (i.e., medium speed) experiments and 1.56 times higher than 1 mm/sec (i.e., low speed) experiments.

5.3 Modelling of bio-inspired BMB needle insertion into the iliac crest

In this study, bioinspired biopsy needles that mimicked honeybee stingers have been designed, modified, and evaluated. The barbed design characteristics may be designed for specific needs with varying penetration depths and tissue mechanical qualities. The simulation results demonstrate three primary phases, such as tissue deformation, insertion, or extraction forces, that occurred during the insertion of the honeybee-inspired biopsy needles. The important bioinspired biopsy needle parameters, viz., α_1 and α_2 have been analyzed to minimize the insertion force. While using barbed biopsy needles with α_1 = 170°compared to =147°, the penetration force has been decreased by 26.66% in skin tissue layers and 8.6% in bone tissue. Similarly, when using a needle with α_2 = 170°instead of a needle with α_2 = 100°, the extraction force has been lowered by an average of 57.54%. The reduction in penetration force has been shown to be caused by a smaller frictional surface among the iliac crest tissue and needle. The most extensive tissue deformation has been found to rise at the needle-punctured point, and the distortion decreased as the needle velocity increased during the post-puncture period because the more exterior effort has been transformed into energy dissipation. Using a biopsy needle with barbed features reduced deflection by up to 50% compared to a conventional bevel needle. The findings are believed to be significant for a better-bioinspired needle for BMB procedures.

5.4 Numerical Model for Simulating Honeybee Stinger-Inspired Needle Insertion: A Parametric Study

The present study involves creating, modifying, and modeling bioinspired needles designed based on honeybee stingers. Barb design parameters that are scalable can account for differences in tissue mechanical properties and insertion depth for various applications. The effect of bioinspired parameters, such as $\alpha_1, \alpha_2, \mathrm{h}, \mathrm{L_b}$, on the insertion/extraction forces have been analyzed to determine the optimal needle design that minimizes the insertion forces. The bioinspired needle significantly reduces insertion force when inserted into an iliac crest model. The bioinspired barbed biopsy needle's scale study showed a 38.3-44.4% reduction in maximum insertion force. When a barbed needle with α_2 = 90° has been employed, insertion forces were then lowered by 53.5% on average at a depth of 53 mm as compared to the other values of α_2. Modifying the needle geometry may significantly alter the needle deflection and reduces the deflection by an average of 28.28%, with α_1 = 170° compared to 167° at an insertion depth of 53 mm during insertion. The observed decrease in the needle insertion force has been related to a decrease in the frictional surface between the skin-bone tissue and the needle.

5.5 In-silico Analysis of Optimal Configurations for Rotational Bio-inspired BMB needle designs: An ANN Approach

This study presents the development of a 3D FE model for needle insertion using the Lagrangian surface-based method. This numerical model offers an alternative approach to needle design by facilitating the understanding of complex needle-tissue interactions and behavior of various bio-inspired biopsy needle designs. Our findings advance preoperative surgical planning by enabling the understanding and prediction of needle deflection, needle forces, tissue damage, and contact stress distribution during needle insertion through in-silico simulations. It can be seen from the results that bidirectional rotation reduced the average insertion force to the extent of 17.64% for skin tissue layers and 72.72% for bone tissue layers compared to unidirectional rotation. The results indicate a substantial decrease in average extraction force to the extent of 66.88% for skin-bone tissue layers and a significant reduction in maximum deflection to the extent of 70.47% when employing bidirectional rotation compared to unidirectional rotation. The findings suggest that bidirectional needle rotation is superior to unidirectional rotation, as it can reduce tissue winding damage while maintaining cutting performance during needle insertion. The proposed tool demonstrates a satisfactory accuracy of over 98% in predicting outputs such as insertion/extraction force, needle deflection, and torque values, affirming its effectiveness. The percentage error between the outputs of the tool and Abaqus has been calculated, falling within the range of 1% to 3%. This level of error is considered quite satisfactory for an ANN model-based tool. Additionally, the proposed tool demonstrated significantly improved time efficiency compared to FE simulation. Clinicians can easily utilize the proposed tool without acquiring additional skills. Unlike many existing tools, this tool does not demand specific knowledge or training, eliminating a common challenge that users face.

5.6 Future Scope

- Validating the model of the Honeybee stinger-based biopsy needle might be a viable area for future studies.
- Research advanced materials for needle construction that offer better strength, durability, and compatibility with bone marrow tissues. Biomimetic materials that mimic natural tissue properties could help reduce tissue damage.
- Investigate technologies for precise needle guidance and navigation. This might involve image-guided systems, augmented reality, or robotic assistance to ensure accurate needle placement and optimal sampling.

- Explore the integration of sensors and imaging technologies into biopsy needles. This could provide real-time feedback on tissue characteristics, depth, and position, improving accuracy and reducing the risk of complications.
- Design of application tool that can give the optimal needle design by inputting bioinspired parameters, revolutionizing the precision and efficiency of needle design for medical procedure

Effect of the conventional needle on the insertion force

A crucial aspect of a clinical procedure that can influence the discomfort, pain, and effectiveness of needle insertion is the insertion speed. The purpose of the present investigation has been to assess the influence of insertion velocity on the usage of a conventional bevel needle by comparing the outcomes for different insertion velocities ranging from 3 mm/sec to 20 mm/sec. A slower insertion may be more precise, but it may also be more difficult to perform and extend the operation duration. When utilizing a conventional needle to puncture skin tissue layers at a depth of 0-10 mm, it was found that when the insertion velocity varies from 3 mm/sec to 20 mm/sec, the insertion force decreases by an average of 30.69%. (Skin tissue layers, refer to Figure A1 in Appendix). Even though a faster insertion velocity could be simpler and quicker, it might also result in less precision when inserting the needle. It has been found that using a conventional needle with an insertion velocity of 3 mm/sec, an average reduction of 15.81% in insertion force results from an insertion velocity of 20 mm/sec (bone tissue layers, see Figure A2 in Appendix). The insertion force curve shows that as the penetration depth rises, the tangential force rises, and the insertion force increases proportionally. As a result, it can be demonstrated that the increase in tangential force is precisely appropriate to a rise in the insertion depth, resulting in an overall increase in the insertion force.

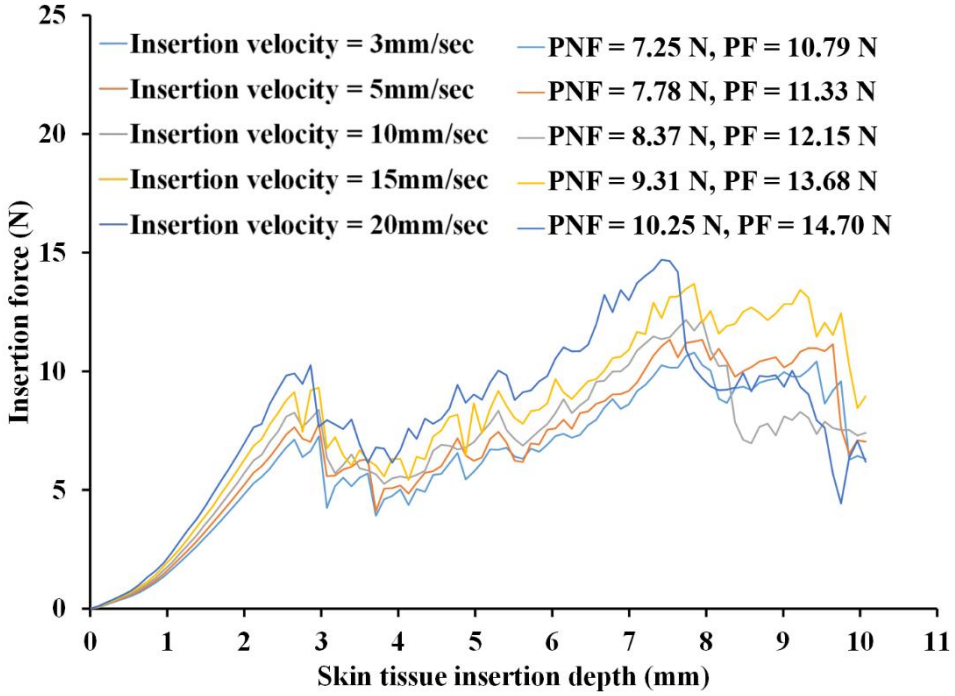

Figure A1. Relationship between the needle (conventional needle) insertion force and the insertion depth in skin tissue layers for various values of insertion velocities

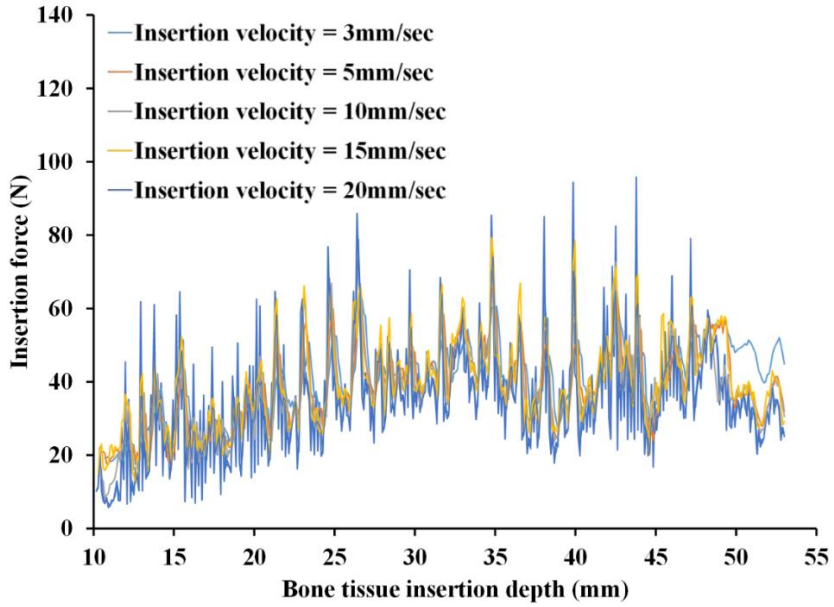

Figure A2. Relationship between the needle (conventional needle) insertion force and the insertion depth in bone tissue layers for various values of insertion velocities

Effect of the conventional needle on the extraction force

The effect of conventional bevel needles on extraction force in the skin and bone tissues at various velocity values ranging from 3 to 20 mm/sec has been shown in Figure A3. At an extraction depth of 53 mm, the average extraction force using a conventional bevel needle decreased by 88.22% when the insertion velocity was reduced from 20 mm/sec to 3 mm/sec. The resistive force has been instantly lowered when the needle was removed.

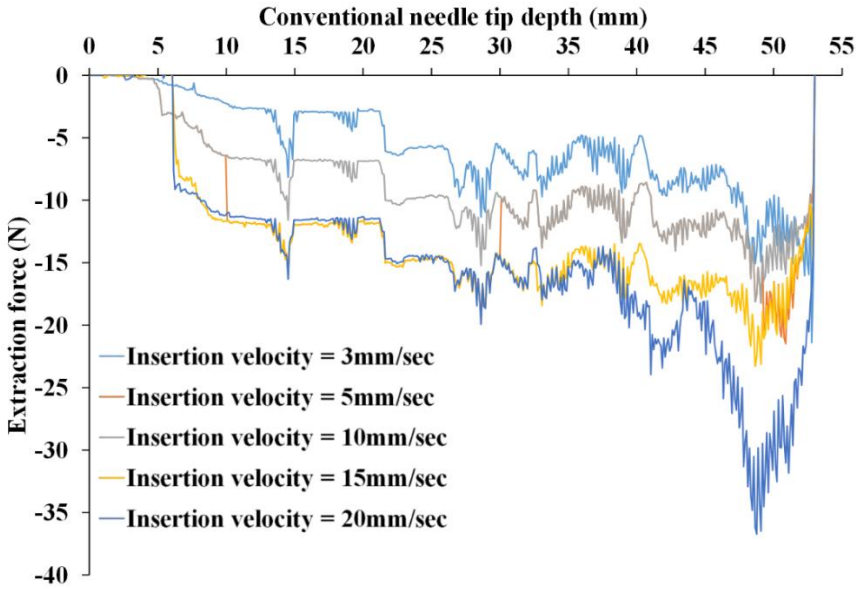

Figure A3. The relationship between the needle extraction force and the needle depth with various values of extraction velocities

FE analysis of the needle deflections

Plain bevel needles and barbed biopsy needles are used in clinical procedures such as biopsies. The primary distinction between them is that the conventional bevel needles have smooth surfaces, whereas the barbed biopsy needles have tiny barbs along the length of the needle. Regarding deflection, the needle's design can influence its flexibility and resistance to deflection. Due to the presence of barbs, which offer extra assistance to the needle, barbed biopsy needles are expected to be more resistant to deflection than conventional bevel needles. The honey bee-inspired barbed biopsy needle, in particular, has been designed to mimic the structure of a honey bee stinger. The barbs on the needle are angled in a specific way to provide maximum deflection resistance while allowing easy insertion and removal from tissue (refer to Figure A4(a)). Conventional bevel needles are more flexible and may bend more easily, especially when encountering resistance from the tissue during insertion (refer to Figure A4(b)). The conventional needle exhibits a maximum deflection of 16.6 mm when inserted at a velocity of 20 mm/sec, while a minimum deflection of 6.27 mm is observed at an insertion velocity of 3 mm/sec (refer to Figure A5). However, they may be preferred for certain procedures where flexibility is important, such as in delicate or hard-to-reach areas. The choice between a plain bevel needle and a barbed biopsy needle will depend on the specific procedure and the healthcare provider's preferences.

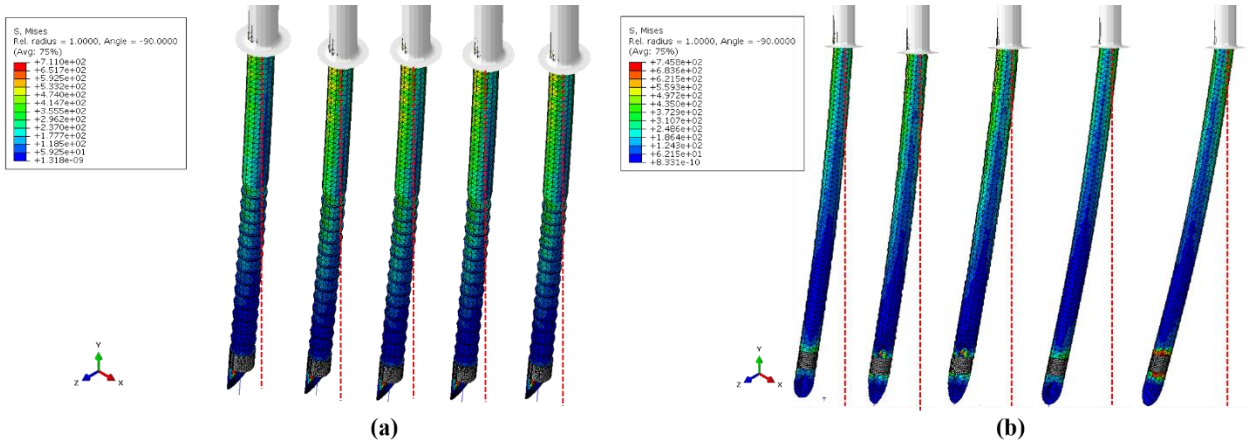

Figure A4. FE analysis of the needle deflection during (a) hollow barbed biopsy needle insertion and (b) conventional bevel needle insertion at 53 mm insertion depth

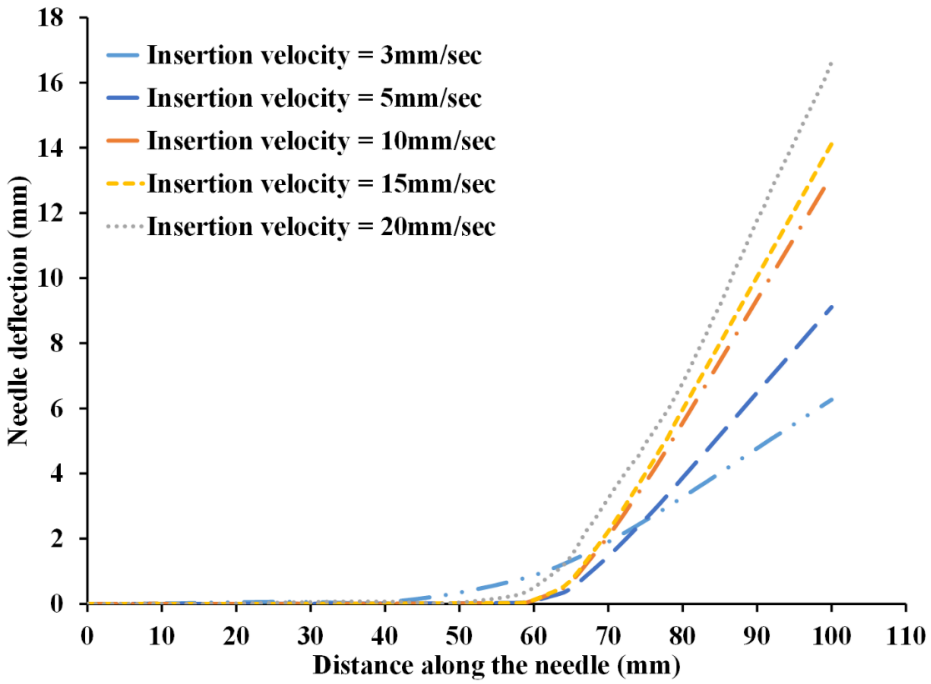

Figure A5. Variation of the needle deflection with the distance along the conventional needle for different insertion velocities

Further details on the Model Validation

To validate the present model, we have employed a computer modeling technique similar to Jushiddi et al. [130]. This approach encompasses specific details regarding the setup of the computational model. We have effectively implemented a built-in 3D dynamic explicit Lagrangian approach, typically accessible in several FE commercial software platforms such as Abaqus. The material properties of soft porcine tissue have been simulated using isotropic linear elastic parameters [130]. In addition, a distortion energy theory combined with element deletion has been employed to account for the evolution of tissue layer failures during insertion. The user subroutine 'VUSDFLD' was utilized to implement the damage evolution (set at 0.01) for various tissue layers. The contact between the needle surface and the tissue skin nodes is modeled using a friction coefficient of 0.2 for tangential behavior and the Hard contact approach for normal behavior. Table A1 shows the material properties utilized from the Jushiddi et al. [130] model.

Table A1. The FE model, incorporated isotropic linear elastic model parameters for the soft porcine tissue.

Tissue Layer	Density (ρ) (g/cm^3)	Poisson's ratio (v)	Elastic Modulus (E) (kPa)
Top	1.017	0.49	80
Middle 1	1.017	0.49	40
Middle 2	1.017	0.49	60
Bottom	1.017	0.49	100

Python script for postprocess of insertion/extraction force and torque results

```
#
table=[  'job_12' ] #11
jobname=table[0]
# -*- coding: mbcs -*-
#
# Abaqus/Viewer Release 2020 replay file
# Internal Version: 2019_09_13-19.49.31 163176
# Run by Rahul Nadda on Wed Aug 10 19:39:05 2022
#
# from driverUtils import executeOnCaeGraphicsStartup
# executeOnCaeGraphicsStartup()
#: Executing "onCaeGraphicsStartup()" in the site directory ...
from abaqus import *
from abaqusConstants import *
session.Viewport(name='Viewport: 1', origin=(0.0, 0.0), width=158.484375,
height=103.82592010498)
session.viewports['Viewport: 1'].makeCurrent()
session.viewports['Viewport: 1'].maximize()
from viewerModules import *

from driverUtils import executeOnCaeStartup
executeOnCaeStartup()
c=jobname+'.odb'
o2 = session.openOdb(name=c)
#: Model:
C:/Users/faouzi/Desktop/freelance/16_needle_insertion_in_skin_and_bone_FEA/abaqus/1_barb_170-
90/job_4.odb
#: Number of Assemblies:                1
#: Number of Assembly instances:     0
#: Number of Part instances:             2
#: Number of Meshes:                      2
#: Number of Element Sets:              12
#: Number of Node Sets:                  13
```

```
#: Number of Steps:            2
session.viewports['Viewport: 1'].setValues(displayedObject=o2)
session.viewports['Viewport: 1'].makeCurrent()
session.viewports['Viewport: 1'].view.zoom(zoomFactor=1.7, mode=ABSOLUTE)
session.viewports['Viewport: 1'].odbDisplay.commonOptions.setValues(visibleEdges=EXTERIOR)
session.viewports['Viewport: 1'].enableMultipleColors()
session.viewports['Viewport: 1'].setColor(initialColor='#BDBDBD')
cmap=session.viewports['Viewport: 1'].colorMappings['Material']
session.viewports['Viewport: 1'].setColor(colorMapping=cmap)
session.viewports['Viewport: 1'].disableMultipleColors()
session.printToFile(fileName='1_undeformed_shape', format=PNG, canvasObjects=(
session.viewports['Viewport: 1'], ))
session.viewports['Viewport: 1'].odbDisplay.display.setValues(plotState=(DEFORMED,))
session.viewports['Viewport: 1'].odbDisplay.commonOptions.setValues(visibleEdges=FEATURE)
session.printToFile(fileName='2_deformed_shape', format=PNG, canvasObjects=(
session.viewports['Viewport: 1'], ))
session.viewports['Viewport: 1'].odbDisplay.setValues(viewCutNames=('Z-Plane',), viewCut=ON)
session.viewports['Viewport: 1'].odbDisplay.viewCuts['Z-Plane'].setValues(position=0)
session.printToFile(fileName='3_deformed_shape', format=PNG, canvasObjects=(
session.viewports['Viewport: 1'], ))
c=jobname+'.odb'
odb = session.odbs[c]
session.xyDataListFromField(odb=odb, outputPosition=NODAL, variable=(('RF',
   NODAL, ((COMPONENT, 'RF2'), )), ('U', NODAL, ((COMPONENT, 'U2'), )), ),
   nodeSets=("NEEDLE.REF", ))
xy1 = session.xyDataObjects['U:U2 PI: NEEDLE N: 1000001']
xy2 = session.xyDataObjects['RF:RF2 PI: NEEDLE N: 1000001']
xy3 = combine(-xy1, -xy2)
xyp = session.XYPlot('XYPlot-1')
chartName = xyp.charts.keys()[0]
chart = xyp.charts[chartName]
c1 = session.Curve(xyData=xy3)
chart.setValues(curvesToPlot=(c1, ), )
session.charts[chartName].autoColor(lines=True, symbols=True)
```

```
session.viewports['Viewport: 1'].setValues(displayedObject=xyp)
session.charts['Chart-1'].majorAxis1GridStyle.setValues(show=True)
session.charts['Chart-1'].majorAxis2GridStyle.setValues(show=True)
session.charts['Chart-1'].minorAxis1GridStyle.setValues(show=True)
session.charts['Chart-1'].minorAxis2GridStyle.setValues(show=True)
session.charts['Chart-1'].majorAxis1GridStyle.setValues(style=DASHED)
session.charts['Chart-1'].majorAxis2GridStyle.setValues(style=DASHED)
session.charts['Chart-1'].gridArea.style.setValues(fill=False)
session.curves['_temp_3'].lineStyle.setValues(thickness=0.5)
session.charts['Chart-1'].legend.setValues(show=False)
session.charts['Chart-1'].axes1[0].axisData.setValues(useSystemTitle=False, title='Displacement (mm)')
session.charts['Chart-1'].axes2[0].axisData.setValues(useSystemTitle=False, title='Force (N)')
session.printToFile(fileName='4_load_vs_disp', format=PNG, canvasObjects=(
session.viewports['Viewport: 1'], ))
x0 = session.xyDataObjects['_temp_3']
session.writeXYReport(fileName='4_load_vs_disp.txt', xyData=(x0, ))
#
session.xyDataListFromField(odb=odb, outputPosition=NODAL, variable=(('RM',
   NODAL, ((COMPONENT, 'RM2'), )), ), nodeSets=("NEEDLE.REF", ))
xy1 = session.xyDataObjects['U:U2 PI: NEEDLE N: 1000001']
xy2 = session.xyDataObjects['RM:RM2 PI: NEEDLE N: 1000001']
xy3 = combine(-xy1, -xy2/1000.)
xyp = session.xyPlots['XYPlot-1']
chartName = xyp.charts.keys()[0]
chart = xyp.charts[chartName]
c1 = session.Curve(xyData=xy3)
chart.setValues(curvesToPlot=(c1, ), )
session.charts[chartName].autoColor(lines=True, symbols=True)
session.charts['Chart-1'].axes2[0].axisData.setValues(useSystemTitle=False, title='Torque (N.m)')
session.curves['_temp_7'].lineStyle.setValues(color='#0000FF')
session.curves['_temp_7'].lineStyle.setValues(thickness=0.5)
session.printToFile(fileName='5_torq_vs_disp', format=PNG, canvasObjects=(
session.viewports['Viewport: 1'], ))
x0 = session.xyDataObjects['_temp_7']
```

```
session.writeXYReport(fileName='5_torq_vs_disp.txt', xyData=(x0, ))
```

Python script of moment data for needle deflection results

```
job='job_12'
nref='1000001'
# -*- coding: mbcs -*-
#
# Abaqus/Viewer Release 2020 replay file
# Internal Version: 2019_09_13-19.49.31 163176
# Run by Rahul Nadda on Tue Dec 27 09:26:50 2022
#
# from driverUtils import executeOnCaeGraphicsStartup
# executeOnCaeGraphicsStartup()
#: Executing "onCaeGraphicsStartup()" in the site directory ...
from abaqus import *
from abaqusConstants import *
session.Viewport(name='Viewport: 1', origin=(0.0, 0.0), width=159.5625, height=103.82592010498)
session.viewports['Viewport: 1'].makeCurrent()
session.viewports['Viewport: 1'].maximize()
from viewerModules import *
from driverUtils import executeOnCaeStartup
executeOnCaeStartup()
o2 = session.openOdb(name=job+'.odb')
#: Model: C:/Users/faouzi/Desktop/Nouveau dossier/job4/job_4.odb
#: Number of Assemblies:         1
#: Number of Assembly instances:  0
#: Number of Part instances:      2
#: Number of Meshes:              2
#: Number of Element Sets:        11
#: Number of Node Sets:           12
#: Number of Steps:               2
session.viewports['Viewport: 1'].setValues(displayedObject=o2)
session.viewports['Viewport: 1'].makeCurrent()
```

```
odb = session.odbs[job+'.odb']
session.xyDataListFromField(odb=odb, outputPosition=NODAL, variable=(('RF',
    NODAL, ((COMPONENT, 'RF2'), )), ('RM', NODAL, ((COMPONENT, 'RM1'), (
    COMPONENT, 'RM3'), )), ('U', NODAL, ((COMPONENT, 'U2'), )), ('UR', NODAL, (
    (COMPONENT, 'UR2'), )), ), nodeSets=("NEEDLE.REF", ))
x0 = session.xyDataObjects['RF:RF2 PI: NEEDLE N: '+nref]
x1 = session.xyDataObjects['U:U2 PI: NEEDLE N: '+nref]
x2 = session.xyDataObjects['UR:UR2 PI: NEEDLE N: '+nref]
x3 = session.xyDataObjects['RM:RM1 PI: NEEDLE N: '+nref]
x4 = session.xyDataObjects['RM:RM3 PI: NEEDLE N: '+nref]
session.writeXYReport(fileName=job+'.txt', appendMode=OFF, xyData=(x0, x1, x2, x3, x4))
```

Python script for needle deflection results

```
# -*- coding: mbcs -*-
#
# Abaqus/Viewer Release 2020 replay file
# Internal Version: 2019_09_13-19.49.31 163176
# Run by Rahul Nadda on Thu Jan 5 09:12:43 2023
#
# from driverUtils import executeOnCaeGraphicsStartup
# executeOnCaeGraphicsStartup()
#: Executing "onCaeGraphicsStartup()" in the site directory ...
from abaqus import *
from abaqusConstants import *
session.Viewport(name='Viewport: 1', origin=(0.0, 0.0), width=159.5625, height=103.82592010498)
session.viewports['Viewport: 1'].makeCurrent()
session.viewports['Viewport: 1'].maximize()
from viewerModules import *
from driverUtils import executeOnCaeStartup
executeOnCaeStartup()
o2 = session.openOdb(name='bending.odb')
#: Model: C:/Users/faouzi/Desktop/Nouveau dossier/job4/bending1/bending.odb
#: Number of Assemblies:         1
#: Number of Assembly instances:  0
#: Number of Part instances:      3
#: Number of Meshes:              3
#: Number of Element Sets:        6
#: Number of Node Sets:          11
#: Number of Steps:               1
session.viewports['Viewport: 1'].setValues(displayedObject=o2)
```

```
session.viewports['Viewport: 1'].makeCurrent()
odb = session.odbs['bending.odb']
session.xyDataListFromField(odb=odb, outputPosition=NODAL, variable=(('U', NODAL),),
nodeSets=("PART1-1.REF", ))
x0 = session.xyDataObjects['U:Magnitude PI: PART1-1 N: 1000002']
x1 = session.xyDataObjects['U:U1 PI: PART1-1 N: 1000002']
x2 = session.xyDataObjects['U:U2 PI: PART1-1 N: 1000002']
x3 = session.xyDataObjects['U:U3 PI: PART1-1 N: 1000002']
# session.writeXYReport(fileName='0_bending.txt', appendMode=OFF, xyData=(x0, x1, x2, x3))
xyp = session.XYPlot('XYPlot-1')
chartName = xyp.charts.keys()[0]
chart = xyp.charts[chartName]
xy1 = session.xyDataObjects['U:Magnitude PI: PART1-1 N: 1000002']
c1 = session.Curve(xyData=xy1)
xy2 = session.xyDataObjects['U:U1 PI: PART1-1 N: 1000002']
c2 = session.Curve(xyData=xy2)
xy3 = session.xyDataObjects['U:U2 PI: PART1-1 N: 1000002']
c3 = session.Curve(xyData=xy3)
xy4 = session.xyDataObjects['U:U3 PI: PART1-1 N: 1000002']
c4 = session.Curve(xyData=xy4)
chart.setValues(curvesToPlot=(c1, c2, c3, c4, ), )
session.charts[chartName].autoColor(lines=True, symbols=True)
session.viewports['Viewport: 1'].setValues(displayedObject=xyp)
session.charts['Chart-1'].legend.area.setValues(inset=True)
session.charts['Chart-1'].legend.area.setValues(positionMethod=AUTOMATIC,alignment=TOP_RIGHT)
session.charts['Chart-1'].majorAxis1GridStyle.setValues(show=True)
session.charts['Chart-1'].majorAxis1GridStyle.setValues(style=DASHED)
session.charts['Chart-1'].majorAxis2GridStyle.setValues(show=True)
session.charts['Chart-1'].majorAxis2GridStyle.setValues(style=DASHED)
session.charts['Chart-1'].minorAxis2GridStyle.setValues(show=True)
session.charts['Chart-1'].minorAxis1GridStyle.setValues(show=True)
session.charts['Chart-1'].gridArea.style.setValues(fill=False)
session.curves['U:Magnitude PI: PART1-1 N: 1000002'].setValues( useDefault=False,
legendLabel='U:Magnitude')
session.curves['U:Magnitude PI: PART1-1 N: 1000002'].lineStyle.setValues(thickness=0.5)
session.curves['U:Magnitude PI: PART1-1 N: 1000002'].setValues(useDefault=False,
legendLabel='U:Magnitude')
session.curves['U:U1 PI: PART1-1 N: 1000002'].setValues(useDefault=False,
legendLabel='U:U1')
session.curves['U:U2 PI: PART1-1 N: 1000002'].setValues(useDefault=False,
legendLabel='U:U2')
session.curves['U:U3 PI: PART1-1 N: 1000002'].setValues(useDefault=False,
legendLabel='U:U3')
session.curves['U:U3 PI: PART1-1 N: 1000002'].lineStyle.setValues(color='#B2FF00')
```

```
#session.pngOptions.setValues(imageSize=(4096, 2134))
#session.printToFile(fileName='0_bending', format=PNG, canvasObjects=(
# session.viewports['Viewport: 1'], ))
#
session.viewports['Viewport: 1'].setValues(displayedObject=odb)
session.viewports['Viewport: 1'].enableMultipleColors()
session.viewports['Viewport: 1'].setColor(initialColor='#BDBDBD')
cmap = session.viewports['Viewport: 1'].colorMappings['Part instance']
cmap.updateOverrides(overrides={'NEEDLE':(True, '#00CCFF', 'Default','#00CCFF')})
session.viewports['Viewport: 1'].setColor(colorMapping=cmap)
session.viewports['Viewport: 1'].disableMultipleColors()
#
leaf = dgo.LeafFromPartInstance(partInstanceName=("NEEDLE", ))
session.viewports['Viewport: 1'].odbDisplay.displayGroup.replace(leaf=leaf)
session.viewports['Viewport: 1'].view.setValues(session.views['Back'])
session.viewports['Viewport: 1'].view.setProjection(projection=PARALLEL)
session.viewports['Viewport: 1'].odbDisplay.display.setValues(plotState=(UNDEFORMED, ))
session.viewports['Viewport: 1'].view.fitView()
session.pngOptions.setValues(imageSize=(4096, 2134))
session.printToFile(fileName='3_undeformed_shape_xy-view', format=PNG,
   canvasObjects=(session.viewports['Viewport: 1'], ))
#
session.viewports['Viewport: 1'].odbDisplay.display.setValues(plotState=(DEFORMED, ))
session.viewports[session.currentViewportName].odbDisplay.setFrame(step='Step-1', frame=1)
session.printToFile(fileName='4_deformed_shape_xy-view_load_applied', format=PNG,
   canvasObjects=(session.viewports['Viewport: 1'], ))
#
session.viewports[session.currentViewportName].odbDisplay.setFrame(step='Step-1', frame=-1)
session.printToFile(fileName='5_deformed_shape_xy-view_load_released', format=PNG,
   canvasObjects=(session.viewports['Viewport: 1'], ))
#
session.viewports['Viewport: 1'].view.setValues(session.views['Right'])
session.viewports['Viewport: 1'].odbDisplay.display.setValues(plotState=(UNDEFORMED, ))
session.viewports['Viewport: 1'].view.fitView()
session.printToFile(fileName='6_undeformed_shape_zy-view', format=PNG,
   canvasObjects=(session.viewports['Viewport: 1'], ))
session.viewports['Viewport: 1'].odbDisplay.display.setValues(plotState=(DEFORMED, ))
session.viewports[session.currentViewportName].odbDisplay.setFrame(step='Step-1', frame=1)
session.printToFile(fileName='7_deformed_shape_zy-view_load_applied', format=PNG,
   canvasObjects=(session.viewports['Viewport: 1'], ))
session.viewports[session.currentViewportName].odbDisplay.setFrame(step='Step-1', frame=-1)
session.printToFile(fileName='8_deformed_shape_zy-view_load_released', format=PNG,
   canvasObjects=(session.viewports['Viewport: 1'], ))
#
```

```
leaf = dgo.LeafFromElementSets(elementSets=("PART3-1.ALL", ))
session.viewports['Viewport: 1'].odbDisplay.displayGroup.replace(leaf=leaf)
session.Path(name='Path-1', type=NODE_LIST, expression=(('PART3-1', ('1:101:1', )), ))
#
session.viewports['Viewport: 1'].odbDisplay.setFrame(step=0, frame=1)
session.viewports['Viewport: 1'].odbDisplay.setPrimaryVariable(
    variableLabel='U', outputPosition=NODAL, refinement=(INVARIANT, 'Magnitude'))
pth = session.paths['Path-1']
session.XYDataFromPath(name='XYData-1', path=pth, includeIntersections=True,
    projectOntoMesh=False, pathStyle=PATH_POINTS, numIntervals=10,
    projectionTolerance=0, shape=UNDEFORMED, labelType=TRUE_DISTANCE,
    removeDuplicateXYPairs=True, includeAllElements=True)
session.viewports['Viewport: 1'].odbDisplay.setPrimaryVariable(
    variableLabel='U', outputPosition=NODAL, refinement=(COMPONENT, 'U1'))
pth = session.paths['Path-1']
session.XYDataFromPath(name='XYData-2', path=pth, includeIntersections=True,
    projectOntoMesh=False, pathStyle=PATH_POINTS, numIntervals=10,
    projectionTolerance=0, shape=UNDEFORMED, labelType=TRUE_DISTANCE,
    removeDuplicateXYPairs=True, includeAllElements=True)
session.viewports['Viewport: 1'].odbDisplay.setPrimaryVariable(
    variableLabel='U', outputPosition=NODAL, refinement=(COMPONENT, 'U3'))
pth = session.paths['Path-1']
session.XYDataFromPath(name='XYData-3', path=pth, includeIntersections=True,
    projectOntoMesh=False, pathStyle=PATH_POINTS, numIntervals=10,
    projectionTolerance=0, shape=UNDEFORMED, labelType=TRUE_DISTANCE,
    removeDuplicateXYPairs=True, includeAllElements=True)
#
session.viewports['Viewport: 1'].odbDisplay.setFrame(step=0, frame=-1)
session.viewports['Viewport: 1'].odbDisplay.setPrimaryVariable(
    variableLabel='U', outputPosition=NODAL, refinement=(INVARIANT,
    'Magnitude'))
pth = session.paths['Path-1']
session.XYDataFromPath(name='XYData-4', path=pth, includeIntersections=True,
    projectOntoMesh=False, pathStyle=PATH_POINTS, numIntervals=10,
    projectionTolerance=0, shape=UNDEFORMED, labelType=TRUE_DISTANCE,
    removeDuplicateXYPairs=True, includeAllElements=True)
session.viewports['Viewport: 1'].odbDisplay.setPrimaryVariable(
    variableLabel='U', outputPosition=NODAL, refinement=(COMPONENT, 'U1'))
pth = session.paths['Path-1']
session.XYDataFromPath(name='XYData-5', path=pth, includeIntersections=True,
    projectOntoMesh=False, pathStyle=PATH_POINTS, numIntervals=10,
    projectionTolerance=0, shape=UNDEFORMED, labelType=TRUE_DISTANCE,
    removeDuplicateXYPairs=True, includeAllElements=True)
session.viewports['Viewport: 1'].odbDisplay.setPrimaryVariable(
```

```
    variableLabel='U', outputPosition=NODAL, refinement=(COMPONENT, 'U3'))
pth = session.paths['Path-1']
session.XYDataFromPath(name='XYData-6', path=pth, includeIntersections=True,
    projectOntoMesh=False, pathStyle=PATH_POINTS, numIntervals=10,
    projectionTolerance=0, shape=UNDEFORMED, labelType=TRUE_DISTANCE,
    removeDuplicateXYPairs=True, includeAllElements=True)
#
xyp = session.xyPlots['XYPlot-1']
chartName = xyp.charts.keys()[0]
chart = xyp.charts[chartName]
xy1 = session.xyDataObjects['XYData-1']
c1 = session.Curve(xyData=xy1)
xy2 = session.xyDataObjects['XYData-2']
c2 = session.Curve(xyData=xy2)
xy3 = session.xyDataObjects['XYData-3']
c3 = session.Curve(xyData=xy3)
chart.setValues(curvesToPlot=(c1, c2, c3, ), )
session.charts[chartName].autoColor(lines=True, symbols=True)
session.viewports['Viewport: 1'].setValues(displayedObject=xyp)
session.curves['XYData-1'].lineStyle.setValues(thickness=0.5)
session.curves['XYData-1'].setValues(useDefault=False, legendLabel='bending')
session.curves['XYData-2'].setValues(useDefault=False,
    legendLabel='bending /x')
session.curves['XYData-3'].setValues(useDefault=False,
    legendLabel='bending /z')
session.charts['Chart-1'].axes2[0].axisData.setValues(useSystemTitle=False,
    title='Deflexion (mm)')
session.charts['Chart-1'].axes1[0].axisData.setValues(useSystemTitle=False,
    title='Distance along the needle')
session.printToFile(fileName='1_bending_load_applied',
    format=PNG, canvasObjects=(session.viewports['Viewport: 1'], ))
#
x1 = session.xyDataObjects['XYData-1']
x2 = session.xyDataObjects['XYData-2']
x3 = session.xyDataObjects['XYData-3']
session.writeXYReport(fileName='1_bending_load_applied.txt', appendMode=OFF, xyData=(x1, x2,x3))
#
xyp = session.xyPlots['XYPlot-1']
chartName = xyp.charts.keys()[0]
chart = xyp.charts[chartName]
xy1 = session.xyDataObjects['XYData-4']
c1 = session.Curve(xyData=xy1)
xy2 = session.xyDataObjects['XYData-5']
c2 = session.Curve(xyData=xy2)
```

```
xy3 = session.xyDataObjects['XYData-6']
c3 = session.Curve(xyData=xy3)
chart.setValues(curvesToPlot=(c1, c2, c3, ), )
session.charts[chartName].autoColor(lines=True, symbols=True)
session.viewports['Viewport: 1'].setValues(displayedObject=xyp)
session.curves['XYData-4'].lineStyle.setValues(thickness=0.5)
session.curves['XYData-4'].setValues(useDefault=False, legendLabel='bending')
session.curves['XYData-5'].setValues(useDefault=False,
   legendLabel='bending /x')
session.curves['XYData-6'].setValues(useDefault=False,
   legendLabel='bending /z')
session.printToFile(fileName='2_bending_load_released',
   format=PNG, canvasObjects=(session.viewports['Viewport: 1'], ))
#
x1 = session.xyDataObjects['XYData-4']
x2 = session.xyDataObjects['XYData-5']
x3 = session.xyDataObjects['XYData-6']
session.writeXYReport(fileName='2_bending_load_released.txt', appendMode=OFF, xyData=(x1, x2,
x3))
```

Python script for stress results

```
"""
odbMaxMises.py
Code to determine the location and value of the maximum
von-mises stress in an output database.
Usage: abaqus python odbMaxMises.py -odb odbName
      -elset(optional) elsetName
Requirements:
1. -odb: Name of the output database.
2. -elset: Name of the assembly level element set.
          Search will be done only for element belonging
          to this set. If this parameter is not provided,
          search will be performed over the entire model.
3. -help: Print usage
"""
#~~~~~~~~~~~~~~~~~~~~~~~~~~~~~~~~~~~~~~~~~~~~~~~~~~~~~~~~~~~~~~~~~~~~~~~~~~~~~~~
from odbAccess import *
from sys import argv,exit
#~~~~~~~~~~~~~~~~~~~~~~~~~~~~~~~~~~~~~~~~~~~~~~~~~~~~~~~~~~~~~~~~~~~~~~~~~~~~~~~
def rightTrim(input,suffix):
   if (input.find(suffix) == -1):
      input = input + suffix
   return input
#~~~~~~~~~~~~~~~~~~~~~~~~~~~~~~~~~~~~~~~~~~~~~~~~~~~~~~~~~~~~~~~~~~~~~~~~~~~~~~~
```

```
def getMaxMises(odbName,elsetName):
   """ Print max mises location and value given odbName
      and elset(optional)
   """
   elset = elemset = None
   region = "over the entire model"
   """ Open the output database """
   odb = openOdb(odbName)
   assembly = odb.rootAssembly

   """ Check to see if the element set exists
      in the assembly
   """
   if elsetName:
      try:
         elemset = assembly.elementSets[elsetName]
         region = " in the element set : " + elsetName;
      except KeyError:
         print 'An assembly level elset named %s does' \
               'not exist in the output database %s' \
               % (elsetName, odbName)
         odb.close()
         exit(0)

   """ Initialize maximum values """
   maxMises = -0.1
   maxElem = 0
   maxStep = "_None_"
   maxFrame = -1
   Stress = 'S'
   isStressPresent = 0
   inc=0
   for step in odb.steps.values():
      print 'Processing Step:', step.name
      for frame in step.frames:
         maxMisesFrame = -0.1
         maxElemFrame = 0
         allFields = frame.fieldOutputs
         if (allFields.has_key(Stress)):
            isStressPresent = 1
            stressSet = allFields[Stress]
            if elemset:
               stressSet = stressSet.getSubset(
                  region=elemset)
```

```
            for stressValue in stressSet.values:
                if (stressValue.mises > maxMises):
                    maxMises = stressValue.mises
                    maxElem = stressValue.elementLabel
                    maxStep = step.name
                    maxFrame = frame.incrementNumber
                if (stressValue.mises > maxMisesFrame):
                    maxMisesFrame = stressValue.mises
        inc+=1
        print ((inc, maxMisesFrame))
        f.write(str(inc)+' '+str(maxMisesFrame)+'\n')
    if(isStressPresent):
        print 'Maximum von Mises stress %s is %f in element %d'% (
            region, maxMises, maxElem)
        print 'Location: frame # %d step:  %s '%(maxFrame,maxStep)
    else:
        print 'Stress output is not available in' \
             'the output database: %s\n' %(odb.name)

    """ Close the output database before exiting the program """
    odb.close()
#=============================================================================
# S T A R T
#
f = open ("maxMise.txt", "w")
f.write("# Frame | maxVonMises\n")
print '# Frame | maxVonMises'
if __name__ == '__main__':
    odbName = None
    elsetName = None
    argList = argv
    argc = len(argList)
    i=0
    while (i < argc):
        if (argList[i][:2] == "-o"):
            i += 1
            name = argList[i]
            odbName = rightTrim(name,".odb")
        elif (argList[i][:2] == "-e"):
            i += 1
            elsetName = argList[i]
        elif (argList[i][:2] == "-h"):
            print __doc__
            exit(0)
```

```
        i += 1
    if not (odbName):
        print ' **ERROR** output database name is not provided'
        print __doc__
        exit(1)
    getMaxMises(odbName,elsetName)

f.close()
```

Page intentionally left blank

References

[1] Riley, R.S.; Hogan, T.F.; Pavot, D.R.; Forysthe, R.; Massey, D.; Smith, E.; Wright, L.; Jr. and Ben-Ezra, J.M. A pathologist's perspective on bone marrow aspiration and biopsy: I. performing a bone marrow examination. J. Clin. Lab. Anal. 2004, 8, 70-90.

[2] Knowles, S.; Hoffbrand, A.V. Bone-marrow aspiration and trephine biopsy (2). Br Med J. 1980, 281(6235), 280–281.

[3] Beckstead, J.H. The bone marrow biopsy. A diagnostic strategy. Arch Pathol Lab Med. 1986,110, 175–179.

[4] Williams, W.J.; Nelson, D.A. Examination of the marrow. In: Williams WJ, Beutler E, Erslev AJ, Lichtman MA, editors. Hematology. New York: McGraw-Hill, Inc. 1972, 24–31.

[5] Rywlin, A.M. Histopathology of the bone marrow. Boston: Little, Brown & Co.; 1976.

[6] Kucklick, T.R.; Kucklick, T.R. (Ed.), Introduction to Needles and Cannulae, CRC Press Taylor and Francis Group, Boca Raton, FL, 200633487–2742.

[7] van Veen, Y.R.; Jahya, A.; Misra, S. Macroscopic and microscopic observations of needle insertion into gels. Proc. IME H J. Eng. Med. 2012, 226(6), 441–449.

[8] Han, P.; Che, D.; Pallav, K.; Ehmann, K. Models of the cutting edge geometry of medical needles with applications to needle design. Int. J. Mech. Sci. 2012, 65(1), 157–167.

[9] Bain, B.J. Morbidity associated with bone marrow aspiration and trephine biopsy - a review of UK data for 2004. Haematologica. 2006, 91,1293-4.

[10] Kuball, J.; Schüz, J.; Gamm, H.; Weber, M. Bone marrow punctures and pain. Acute Pain. 2004, 6, 9–14

[11] Vanhelleputte, P.; Kristel, N.; Delforge, M.; Evers, G.; Vanderschueren, S. Pain during bone marrow aspiration: prevalence and prevention. J Pain Symptom Manage. 2003, 26, 860–866.

[12] Dalrymple, J. On the microscopical character of mollities ossium. Dublin Quarterly J Med Sci. 1846, 85–95.

[13] Arinkin, M.I. Die intravitale untersuchungsmethodik des knochenmarks. Folia Haematol. 1929, 38, 233–240.

[14] Arinkin, M.I. The intravital method of examining the bone marrow. Clin Orthop. 1970, 73, 3–7.

[15] Raich, P.C. Bone marrow needle biopsy: method and indications. Wis Med J. 1974, 73, 155–160.

[16] Custer, R.P. Biopsy of the bone marrow. In: An atlas of the blood and bone marrow. Philadelphia: W.B. Saunders Co.; 1974, 537–551.

[17] Reich, C. A Clinical atlas of sternal bone marrow. Whats New. 1946, 100, 17-32.

[18] Custer, R.P. Studies on the structure and function of bone marrow: bone marrow biopsy. Am J Med Sc. 1933, 185, 617–624.

[19] McFarland, W.; Dameshek, W. Biopsy of bone marrow with the Vim-Silverman needle. J Am Med Assoc. 1958, 166(12), 1464–1466.

[20] Ellis, L.D.; Jensen, W.N.; Westerman, M.F. Needle biopsy of bone and bone marrow. An experience with 1,445 biopsies. Arch Intern Med. 1964, 114, 213–214.

[21] Jamshidi, K.; Swaim, W.R. Bone marrow biopsy with unaltered architecture: a new biopsy device. J Lab Clin Med. 1971, 77, 335–342.

[22] Jamshidi, K.; Windschitl, H.E.; Swaim, W.R. A new biopsy needle for bone marrow. Scand J Haematol. 1971, 8, 69–71.

[23] Birch, C.D.; Fischer, S.; Zibell, A.; Jensen, M.E. Diagnostic bone marrow studies extended routinely by iliac crest biopsy, using the method of Schaadt-Fischer. Acta Pathol Microbiol Immunol Scand. 1982, 90, 229–234.

[24] Goldenberg, A.S.; Rishton, M. Bone-marrow biopsy needle incorporating a snare-coil specimen-capturing device:description and preclinical studies. Biomed Instrum Technol. 1999, 33, 522–529.

[25] Goldenberg, A.S.; Tiesinga, J.J. Clinical experience with a new specimen capturing bone marrow biopsy needle. Am J Hematol. 2001, 68, 189–193.

[26] Bates, I.; Burthem, J. 7 - Bone Marrow Biopsy. Dacie and Lewis Practical Haematology (Twelfth Edition) 2017, 12-125.

[27] Thachil, J.; Bates, I. Approach to the Diagnosis and Classification of Blood Cell Disorders. Dacie and Lewis Practical Haematology. 2017, 497–510.

[28] Anwarul, Islam. A New Single-Use Bone Marrow Biopsy Needle with Core Retention Design. Biomed J. Sci & Tech Res. 2019, 19, 14293-14299

[29] Lewandowski, K.; Complak, A.; Hellmann, A. Microscopic examination of bone marrow aspirates in malignant disorders of haematopoiesis-a comparison of two slide preparation techniques. Ann Hematol. 2012, 91, 497-505.

[30] Mihailescu, S.D.; Jaselme, P.; Fontoura, M.L.; Hannachi, L.F.; Veresezan, E.L.; Drieux, F.; Vincent, C.; Florian, B.; Hervé, Tilly.; Nathalie, C.; Fabrice, J. Comparison of bone marrow trephine sample quality between a drill-powered system and a manual needle system. Ann Diagn Pathol. 2022, 59, 151952.

[31] Rywlin, A.M. Histopathology of the bone marrow. Boston: Little, Brown & Co.; 1976.

[32] Gendron, N.; Sara, Z.C.; Poenou, G.; Rivet, N.; Belleville-Rolland, T.; Lemaire, P.; IEscuret, A.; Ciaudo, M.; Curtis, E.; Gaussem, P.; Siguret, V.; Darnige, L.I 2019) Pain assessment and factors influencing pain during bone marrow aspiration: A prospective study. PLOS ONE. 14, e0221534.

[33] Jamshidi, K.; Swaim, W.R. Bone marrow biopsy with unaltered architecture: a new biopsy device. J Lab Clin Med. 1971, 77, 335– 342.

[34] Jamshidi, K.; Windschitl, H.E.; Swaim, W.R. A new biopsy needle for bone marrow. Scand J Haematol. 1971, 8, 69–71.

[35] Jacobs, P. Bone-marrow aspiration and trephine biopsy. Br Med J. 1980, 281, 944.

[36] Raich, P.C. Rogers 2nd JS. Bone marrow aspiration and biopsy. W V Med J. 1980, 76, 1–4.

[37] Garnier, H.; Reynier, J.; Dimopoulog, F. A propos des accidents dela ponction sternale. Ann Chir. 1964, 18, 308.

[38] Puschel, K.; Mattern, R.; Mittmeyer, H.J.; Schneider, V. Errors and hazards: fatalities through sternal puncture. Dtsch Med Wochenschr. 1985, 110, 1611–1613.

[39] Eastlund, D.T. Sternal-manubrial separation as a complication of marrow aspiration in a patient with protein-calorie malnutrition and osteoporosis. Acta Haemat. 1990, 83, 42–44.

[40] Yoell, J.H. Bone marrow embolism to lung following sternal puncture. Arch Pathol Lab Med. 1959, 67, 373.

[41] Fine, N.L.; Reich, E.J.; Weinsaft, P. Growth of sternal tumor mass following bone marrow aspiration. MNY State J Med. 1967, 67, 2866.

[42] Ben-Chetrit, E.; Flusser, D.; Assaf, Y. Severe bleeding complicating percutaneous bone marrow biopsy. Arch Intern Med. 984, 144, 2284.

[43] Steinke, B. Complications after bone marrow biopsy. Dtsch Med. Wochenschr. 1992, 117, 1003–1004.

[44] Gupta, S.; Meyers, M.L.; Trambert, J.; Billett, H.H. Massive intraabdominal bleeding complicating bone marrow aspiration and biopsy in multiple myeloma. Postgrad Med J. 1992, 68, 770.

[45] Kucklick, T.R.; Kucklick, T.R. (Ed.), Introduction to Needles and Cannulae, CRC Press Taylor and Francis Group, Boca Raton, FL, 200633487–2742.

[46] Veen, Y.R.; Jahya, A.; Misra, S.; Macroscopic and microscopic observations of needle insertion into gels. Proc. IME H J. Eng. Med. 2012, 226, 441–449.

[47] Han, P.; Che, D.; Pallav, K.; Ehmann, K. Models of the cutting edge geometry of medical needles with applications to needle design. Int. J. Mech. Sci. 2012, 65, 157–167.

[48] Towler, M.A.; McGregor, W.; Rodeheaver, G.T.; Cutler, P.V.; Robert F. Bond, R.F.; David Phung, D.; Morgan, R.G.; Thacker, J.G.; Richard F.; Edlich, R.F. Influence of cutting edge configuration on surgical needle penetration forces. J. Emerg. Med. 1988, 6, 475–481.

[49] Assaad, W.; Jahya, A.; Moreira, P.; Misra, S. Finite-element modeling of a bevel-tipped needle interacting with gel. J. Mech. Med. Biol. 2015, 15, 1550079.

[50] Jahya, A.; van der Heijden, F.; Misra, S. Observations of three-dimensional needle deflection during insertion into soft tissue. in Biomedical Robotics and Biomechatronics (BioRob), 2012 4th IEEE RAS & EMBS International Conference on. 2012. IEEE.

[51] DiMaio, S.P.; Salcudean, S.E. Interactive simulation of needle insertion models. IEEE Trans. Biomed. Eng. 2005, 52, 1167–1179.

[52] Chinzei, K.; Hata, N.; Jolesz, F.A.; Kikinis, R. MR compatible surgical assist robot: system integration and preliminary feasibility study, International Conference on Medical Image Computing and Computer-Assisted Intervention, Springer, 2000.

[53] Jiang, S.; Li, P.; Yu, Y.; Liu, J.; Yang, Z. Experimental study of needle–tissue interaction forces: effect of needle geometries, insertion methods and tissue characteristics. J. Biomech. 2014, 47, 3344–3353.

[54] van Gerwen, D.J.; Dankelman, J.; van den Dobbelsteen, J.J. Needle–tissue interaction forces–A survey of experimental data. Med. Eng. Phys. 2012, 34, 665–680.

[55] DiMaio, S.P.; Salcudean, S.E. Needle insertion modeling and simulation. IEEE Trans. Robot. Autom. 2003, 19, 864–875.

[56] Misra, S.; Ramesh, K; Okamura, A.M. Modeling of Tool-Tissue Interactions for Computer-Based Surgical Simulation: A Literature Rev. 2008, 17, 463.

[57] Jiang, S.; Li, P.; Yu, Y.; Liu, J.; Yang, Z. Experimental study of needle–tissue interaction forces: effect of needle geometries, insertion methods and tissue characteristics. J. Biomech. 2014, 47, 3344–3353.

[58] van Gerwen, D.J.; Dankelman, J.; van den Dobbelsteen, J.J. Needle–tissue interaction forces–A survey of experimental data. Med. Eng. Phys. 2012, 34, 665–680.

[59] Oldfield, M.; Dini, D.; Giordano, G.; Baena, F.R.Y. Detailed finite element modelling of deep needle insertions into a soft tissue phantom using a cohesive approach. Comput. Methods Biomech. Biomed. Eng. 2013, 16, 530–543.

[60] Yamaguchi, S.; Tsutsui, K.; Satake, K.; Morikawa, S., Shirai, Y.; Tanaka, H.T. Dynamic analysis of a needle insertion for soft materials: arbitrary Lagrangian–Eulerian-based three-dimensional finite element analysis, Comput. Biol. Med. 2014, 53, 42–47.

[61] Donea, J.; Giuliani, S.; Halleux, J.P. An arbitrary Lagrangian-Eulerian finite element method for transient dynamic fluid-structure interactions. Comput. Methods Appl. Mech. Eng. 1982, 33, 689–723.

[62] Liang, D.; Jiang, S.; Yang, Z.; Wang, X. Simulation and experiment of softtissue deformation in prostate brachytherapy. Proc Inst Mech Eng H J Eng Med. 2016, 230, 532-44.

[63] Kerdok, A.E.; Cotin, S.M.; Ottensmeyer, M.P.; Galea, A.M.; Howe, R.D.; Dawson, S.L. Truth cube: Establishing physical standards for soft tissue simulation. Med Image Anal. 2003, 7, 283-91.

[64] Oldfield, M.J.; Burrows, C.; Kerl, J.; Frasson, L.; Parittotokkaporn, T.; Beyrau, F.; Baena, F.R. Highly resolved strain imaging during needle insertion: results with a novel biologically inspired device. J Mech Behav Biomed Mater. 2014, 30, 50-60.

[65] Maurin, B.; Barbe, L.; Bayle, B.; Zanne, P.; Gangloff, J.; Mathelin, M.D.; Gangi, A.; Soler, L.; Forgione, A. In vivo study of forces during needle insertions, Proceedings of the Scientific Workshop on Medical Robotics, Navigation, and Visualization, 2004, 415-422.

[66] Okamura, A.M.; Simone, C.; O'Leary, M.D. Force modeling for needle insertion into soft tissue. IEEE Trans. Biomed. Eng. 2004, 51, 1707–1716.

[67] Hing, J.T.; Brooks, A.D.; Desai, J.P.; Reality-based estimation of needle and soft-tissue interaction for accurate haptic feedback in prostate brachytherapy simulation. Robot. Res. 2007, 28, 34–48.

[68] Misra, S.; Reed, K.B.; Douglas, A.S.; Ramesh, K.T.; Okamura, A.M. Needle–tissue interaction forces for bevel-tip steerable needles. in Proc. 2nd Biennial IEEE/RAS-EMBS Int. Conf. Biomed. Robot. Biomechatron. 2008, 224–231.

[69] Kobayashi, Y.; Onishi, A.; Watanabe, H.; Hoshi, T.; Kawamura, K.; Fujie, M.G. In vitro validation of viscoelastic and non-linear physical model of liver for needle insertion simulation. in Proc. 2nd Biennial IEEE/RAS-EMBS Int. Conf. Biomed. Robot. Biomechatron. 2008, 469–476.

[70] Yan, K.G.; Podder, T.; Yu, Y.; Liu, T.; Cheng, C.W.S. Flexible needle–tissue interaction modeling with depth-varying mean parameter: Preliminary study. IEEE Trans. Biomed. Eng. 2009, 56, 255–262

[71] Barbe, L.; Bayle, B.; de Mathelin, M. In vivo model estimation and haptic characterization of needle insertions. Int. J. Robot. Res., 2007, 26, 1283–1301.

[72] Yen, P.; Hibberd, R.D.; Davies, B.L. A telemanipulator system as an assistant and training tool for penetrating soft tissue. Mechatronics. 1996, 6, 423–436.

[73] Brett, P.N.; Harrison, A.J.; Thomas, T.A. Schemes for the identification of tissue types and boundaries at the tool point for surgical needles. IEEE Trans. Inform. Technol. Biomed. 2000, 4, 30–36.

[74] Scali, M.; Kreeft, D.; Breedveld, P.; Dodou, D. Design and evaluation of a wasp-inspired steerable needle Proc. 2016, 78-78.

[75] Shergold, O.; Fleck, N. Experimental investigation into the deep penetration of soft solids by sharp and blunt punches, with application to the piercing of skin. J. Biomech. Eng. 2005, 127, 838–48.

[76] Mahvash, M.; Dupont, P.E. Mechanics of dynamic needle insertion into a biological material IEEE Trans. Biomed. Eng. 2010, 57, 934–43.

[77] Chebolu, A.; Mallimoggala, A.; Nagahanumaiah. Modelling of cutting force and deflection of medical needles with different tip geometries. Proc. Mater. Sci. 2014, 5, 2023–31.

[78] Ling, J.; Jiang, L.; Chen, K.; Pan, C.; Li, Y.; Yuan, W.; Liang, L. Insertion and Pull Behavior of Worker Honeybee Stinger. J. Bionic Eng. 2016, 13, 303–11.

[79] Wu, J.; Yan, S.; Zhao, J.; Ye, Y.; Barbs facilitate the helical penetration of honeybee (Apis mellifera ligustica) stingers. PLoS One. 2014, 9, 103823.

[80] Sahlabadi, M.; Hutapea. P. Novel design of honeybee-inspired needles for percutaneous procedure. Bioinspir. Biomim. 2018, 13, 036013

[81] Ramasubramanian, M.K.; Barham, O.M.; Swaminathan, V. Mechanics of a mosquito bite with applications to microneedle design. Bioinspir. Biomim. 2008, 3, 046001

[82] Shoffstall, A.; Srinivasan, S.; Willis, M.; Stiller, A.M.; Ecker, M.; Voit, W.E.; Pancrazio, J.J.; Capadona, J.R. A Mosquito Inspired Strategy to Implant Microprobes into the Brain Sci. Rep. 2018, 8, 1–10.

[83] Gordon, R.M.; Lumsden, W.H.R. A study of the behavior of the mouth-parts of mosquitoes when taking up blood from living tissue together with some observations on the ingestion of microfilariae. Ann. trop. med. Parasitol. 1939, 33, 259–278.

[84] Anne, H. Notes on the piercing mouthparts of three species of mosquitoes viewed with the scanning electron microscope. Can. Entomol. 1970, 102, 501–509.

[85] Jones, J.C. The feeding behavior of mosquitoes. Sci. Am.1978, 238, 112–120.

[86] Kong, X.Q.; Wu, C.W. Measurement and prediction of insertion force for the mosquito fascicle penetrating into human skin. J. Bionic. Eng. 2009, 6, 143–152.

[87] Kong, X.Q.; Wu, C.W. Mosquito proboscis: an elegant biomicroelectromechanical system. Phys. Rev. E. 2010, 82, 2007–2014.

[88] Lenau, T.A.; Hesselberg, T.; Drakidis, A.; Silva, P.; Gomes, S. Mosquito inspired medical needles Bioinspiration, Biomimetics, Bioreplication 2017, 1016208.

[89] Aoyagi, S.; Izumi, H.; Fukuda, M. Biodegradable polymer needle with various tip angles and consideration on insertion mechanism of mosquito's proboscis. Sens. Actuator A Phys. 2008, 143, 20–8

[90] Yang, M.; Zahn, J.D. Microneedle Insertion Force Reduction Using Vibratory Actuation. Biomed. Microdevices. 2004, 6, 177–82

[91] Huang, Y.C.; Tsai, M.C.; Lin, C.H. A piezoelectric vibration-based syringe for reducing insertion force. IOP Conf. Ser. Mater. Sci. Eng. 2012, 42, 012020

[92] Begg, N.D.M.; Slocum, A.H. Audible frequency vibration of puncture-access medical devices. Med. Eng. Phys. 2014, 36, 371–7

[93] Bi, D.; Lin, Y. Vibrating needle insertion for trajectory optimization Proc. World Congr. Intell. Control Autom. 2008, 7444–7448

[94] Cho, W.K.; Ankrum, J.A.; Guo, D.; Chester, S.A.; Yang, S.Y.; Kashyap, A.; Campbell, G.A.; Wood, R.J.; Rijal, R.K.; Karnik, R.; Langer, R.; Kar, J.M. Microstructured barbs on the North American porcupine quill enable easy tissue penetration and difficult removal. Proc. Natl. Acad. Sci. USA. 2012, 109, 21289–21294.

[95] Ling, J.; Song, Z.; Wang, J.; Chen, K.; Li, J.; Xu, S.; Ren, L.; Chen, Z.; Jin, D.; Jiang, L. Effect of honeybee stinger and its microstructured barbs on insertion and pull force. J. Mech. Behav. Biomed. Mater. 2017, 68, 173–179.

[96] Abolhassani, N.; Patel, R.; Moallem, M. Needle insertion into soft tissue: A survey. Med Eng Phys. 2007, 29, 413-31.

[97] Nadda, R.; Repaka, R.; Mallik, N.; Sahani, A.K. A prospective survey on trephine biopsy of bone and bone marrow: an experience with 274 Indian patients' biopsies. Eur. J. Med. Res. 2023, 28, 193.

[98] Sommen, F.; Zinger, S.; Peter, H.N. Accurate biopsy-needle depth estimation in limited-angle tomography using multi-view geometry, Proc. SPIE 9786, Medical Imaging 2016: Image-Guided Procedures, Robotic Interventions, and Modeling. 2016, 9786.

[99] Li, D.R.; Yeh, J.K.; Putra, K.; Shih, A. Optical Measurement of Tissue Deformation in Needle Insertion. Proc. CIRP. 2017, 65, 175-179.

[100] Davis, S.P.; Landis, B.J.; Adams, Z.H.; Allen, M.G.; Prausnitz, M.R. Insertion of microneedles into skin: measurement and prediction of insertion force and needle fracture force. J Biomech. 2004, 37, 1155–1163.

[101] Yan, B.H.; Wang, C.C.; Liu, W.D.; Huang, F.Y. Machining characteristics of Al2O3/6061Al composite using rotary EDM with a disk like electrode. Int. J. Adv. Manufac. Technol. 2000,16, 322-333.

[102] Nadda, R.; Repaka, R. In-silico analysis of optimal configurations for rotational bioinspired bone marrow biopsy needle designs: An ANN Approach, Ann Biomed Eng. 2024, 1-19.

[103] Wildnauer, R.H.; Bothwell, J.W.; Douglass, A.B. Stratum Corneum biomechanical properties I. Influence of relative humidity on normal and extracted human stratum corneum. J. Invest. Dermatol. 1971, 56, 72–78.

[104] NíAnnaidh, A.; Cassidy, M.; Curtis, M.; Destrade, M.; Gilchrist, M.D. A combined experimental and numerical study of stab-penetration forces. Forensic Sci. Int. 2013, 233, 7–13.

[105] Geerligs, M. A literature review of the mechanical behaviour of the stratum corneum, the living epidermis and the subcutaneous fat tissue. Tech Note PR-TN 2006.

[106] Kong, X.Q.; Zhou, P.; Wu, C.W. Numerical simulation of microneedles' insertion into skin. Comput. Methods Biomech. Biomed. Eng. 2011, 14, 827–835.

[107] Hendriks, F.M.; Brokken, D.; Oomens, C.W.; Bader, D.L.; Baaijens, F.P. The relative contributions of different skin layers to the mechanical behavior of human skin in vivo using suction experiments. Med Eng Phys. 2006, 28, 259–266.

[108] Duck, F.A. Chapter 5 - mechanical properties of tissue, in: Physical Properties of Tissues. Academic Press, London, 1990, 137–165

[109] Gerling, G.J.; Thomas, G.W. The effect of fingertip microstructures on tactile edge perception. paper presented at: IEEE Virtual Reality Conference-World Haptics Symposium; Pisa, Italy. 2005

[110] Demirbas, A.E.; Ekici, R.; Karakaya, M.; Alkan, A. Bone stress and damage distributions during dental implant insertion: a novel dynamic FEM analysis. Comput. Methods Biomech. Biomed. Eng. 2022, 25, 1381-1392.

[111] Yeoh, O.H. Some Forms of the Strain Energy Function for Rubber. Rubber Chem. Techno. 1993, 66, 754–771.

[112] Vercher, A.; Giner, E.; Arango, C.; Tarancón, J.E.; Fuenmayor, F.J. Homogenized stiffness matrices for mineralized collagen fibrils and lamellar bone using unit cell finite element models. Biomech. Model Mechanobiol. 2014, 13, 437–49.

[113] O'Mahony, A.M.; Williams, J.L.; Spencer, P. Anisotropic elasticity of cortical and cancellous bone in the posterior mandible increases peri-implant stress and strain under oblique loading. Clin. Oral Implant Res. 2000, 12, 48–57.

[114] Elkhyat, A.; Courderot-Masuyer, C.; Gharbi, T.; Humbert, P. Influence of the hydrophobic and hydrophilic characteristics of sliding and slider surfaces on friction coefficient: in vivo human skin friction comparison. Skin Res. Technol. 2004, 10, 215–221.

[115] Sobolev, A.V.; Radchenko, M.V. Use of Johnson–Cook plasticity model for numerical simulations of the SNF shipping cask drop tests, Nucl. Eng. Technol. 2016, 2, 272-276.

[116] Nadda, R.; Repaka, R.; Sahani, A.K. Finite element simulation of multi-layer model to simulate fine needle insertion mechanism into iliac crest for bone marrow biopsy. Comput Methods Biomech Biomed Engin. 2022, 26, 877-892.

[117] Singh, S.; Repaka, R.; Al-Jumaily, A. Sensitivity analysis of critical parameters affecting the efficacy of microwave ablation using Taguchi method. Int J RF Microw Comput Aided Eng. 2019, 29, e21581.

[118] Degen, C.; Christen, S.; Rovo, A.; Gratwohl, A. Bone marrow examination: a prospective survey on factors associated with pain. Ann Hematol. 2010, 89, 619–624.

[119] Parapia, LA. Trepanning or trephines: a history of bone marrow biopsy. Br J Haematol. 2007, 139, 14-19.

[120] Islam, A. Bone marrow solid core biopsy needle: a critical assessment of the utility, benefits and limitations of the instruments employed in current day haematology and oncology. J Clin Pathol. 2018, 7, 475-482.

[121] Vanhelleputte, P.; Kristel, N.; Delforge, M.; Evers, G.; Vanderschueren, S. Pain during bone marrow aspiration: prevalence and prevention. J Pain Symptom Manage. 2003, 26, 860–866.

[122] Wolanskyj, A.P.; Schroeder, G.; Wilson, P.R. A randomized placebo-controlled study of outpatient premedication for bone marrow biopsy in adults with lymphoma. Clin Lymphoma. 2000, 1, 154–157.

[123] Giannoutsos, I.; Grech, H.; Maboreke, T.; Morgenstern, G. Performing bone marrow biopsies with or without sedation: a comparison. Clin Lab Haem. 2004, 26, 201–204.

[124] Park, S.H.; Bang, S.M.; Nam, E.; Cho, E.K.; Shin, D.B.; Lee, J.H.; Ahn, J.Y. A randomized double-blind placebo-controlled study of low-dose intravenous Lorazepam to reduce procedural pain during bone marrow aspiration and biopsy. Pain Med. 2008, 9, 249–252.

[125] Milligan, D.W.; Howard, M.R.; Judd, A. Premedication with Lorazepam before bone marrow biopsy. J Clin Pathol. 1987, 40, 696–698.

[126] Sandler, E.S.; Weyman, C.; Conner, K.; Reilly, K.; Dickson, N.; Luzins, J.; McGorray, S. Midazolam versus fentanyl as premedication for painful procedures in children with cancer. Pediatrics. 1992, 89, 631–634.

[127] Burkle, C.; Harrison, B.; Koenig, F.; Decker, P.; Warner, D.; Gastineau, D. Morbidity and mortality of deep sedation in outpatient bone marrow biopsy. Am J Hematol. 2004, 77, 250–256.

[128] Pellier, I.; Monrigal, J.; le Moine, P.; Rod, B.; Railland, X.; Granry, J.C. Use of intravenous ketamine-midazolam association for pain procedures in children with cancer. A prospective study. Paediatr Anaesth. 1992, 9, 61–68

[129] Chakupurakal, G.; Delgado, J.; Nikolousis, E.; Pitchapillai, S.; Allotey, D.; Holder, K.; Bratby, L.; de la Rue, J.; Milligan, D.W. Midazolam in conjunction with local anaesthesia is superior to Entonox in providing pain relief during bone marrow aspirate and trephine biopsy. J Clin Pathol. 2008, 61, 051–1054

[130] Dunlop, T.J.; Deen, C.; Lind, S.; Voyle, R.J.; Prichard, J.G. Use of combined oral narvotic and benzodiazepine for control of pain associated with bone marrow examination. South Med J. 1999, 92, 477–480.

[131] Swerdlow, S.; Campo, E.; Harris, N.L.; Jaffe, E.S.; Pileri, S.A.; Stein, H.; Thiele, J. WHO Classification of Tumours of Haematopoietic and Lymphoid Tissues. 4th ed. Lyon, France: IARC Press; 2017.

[132] Kuball, J.; Schüz, J.; Gamm, H.; Weber, M. Bone marrow punctures and pain. Acute Pain. 2004, 6, 9–14.

[133] Brestoff, J.R.; Toland, A.; Afaneh, K.; Qavi, A.J.; Press, B.; Westervelt, P.; Kreisel, F.; Hassan, A. Bone Marrow Biopsy Needle Type Affects Core Biopsy Specimen Length and Quality and Aspirate Hemodilution. Am J Clin Pathol. 2019, 151, 185–193.

[134] van de Berg, N.; de Jong, T.; van Gerwen, D.; Dankelman, J.; van den Dobbelsteen, J.J. The influence of tip shape on bending force during needle insertion. Sci Rep. 2017, 7, 40477.

[135] Webster, R.J.; Memisevic, J.; Okamura, A.M. 2005. Design Considerations for Robotic Needle Steering. Proceedings of the 2005 IEEE International Conference on Robotics and Automation. 2005, 2, 3588-3594.

[136] Mulligan, R.; Yin, L.; Lamont, A.; Peng, Z.; Forwood, M.R.; Teoh, S.H. Effect of Penetration Rate on Insertion Force in Trabecular Bone Biopsy. Mater. Sci. Forum. 2010, 654-656, 2225-2228.

[137] Li, S.; Wahab, A.A.; Demirci, E.; Silberschmidt, V.V. Penetration of cutting tool into cortical bone: Experimental and numerical investigation of anisotropic mechanical behavior. J. Biomech. 2014, 47, 1117-1126.

[138] Carra, A.; Avila-Vilchis, J.C. Needle insertion modeling through several tissue layers. 2010 2nd International Asia Conference on Informatics in Control, Automation and Robotics (CAR 2010), 2010, 237-240.

[139] Jushiddi, M.G.; Mulvihill, J.J.E.; Chovan, D.; Mani, A.; Shanahan, C.; Silien, C.; Tofail, A.M.; Tiernan, P. Simulation of biopsy bevel-tipped needle insertion into soft-gel. Comput. Biol. Med. 2019, 111, 103337.

[140] Jushiddi, M.G.; Mani, A.; Silien, C.; Tofail, S.A.M.; Tiernan, P.; Mulvihill, J.J.E. A computational multilayer model to simulate hollow needle insertion into biological porcine liver tissue. Acta Biomater. 2021, 136, 389-401.

[141] Moore, J.Z.; McLaughlin, P.W.; Shih, A.J. Novel needle cutting edge geometry for end-cut biopsy. Med. Phys. 2012, 39, 99–108.

[142] Zhao, B.; Lei, L.; Xu, L.; Li, S.; Hu, Y.; Zhang, J.; Yang, X.; Zhang, Y. Needle Deflection Modeling and Pre-operative Trajectory Planning During Insertion Into Multilayered Tissues. IEEE/ASME Trans Mechatron. 2012, 26, 943-954.

[143] Moore, J. Malukhin, K. Shih, A. Ehmann, K. Hollow Needle Tissue Insertion Force Model. CIRP Ann Manuf Technol. 2011, 60, 157–60.